Thomas Traußnig

Charge-induced property tuning of nanoscaled metals and metal oxides

DOCTORAL THESIS

For obtaining the academic degree of

Doktor der technischen Wissenschaften

Doctoral Programme of Technical Sciences
Technical Physics

Graz University of Technology

Supervisor:

Univ.-Prof. Dr. Roland Würschum

Institute of Materials Physics

Graz, March 2011

Contents

Abstract **vii**

I. Introduction and Experimental **1**

1. Introduction **3**

2. Physical Basics **7**

2.1. Charge-induced property tuning of metals 7

2.2. Formation of nanoporous structures by dealloying 9

2.3. Magnetism in metal oxides 10

3. Experimental procedures **13**

3.1. Synthesis 13

3.1.1. Chemical FePt-nanoparticle synthesis by hot-injection/polyol process 13

3.1.2. Nanoparticle formation by condensation in inertgas 14

3.1.2.1. Powder preparation for charging experiments 14

3.2. Electrochemical characterization methods 16

3.2.1. Cyclovoltammetry 16

3.2.1.1. Double layer regime 16

3.2.1.2. Chemisorption regime 17

3.2.1.3. Pseudocapacitive charging regime 17

3.2.2. Chronoamperometry 17

3.3. SQUID magnetometry 20

3.3.1. Design of an electrochemical cell for in-situ charging 22

3.4. Dealloying and resistance measurement of nanoporous Au 22

II. Results and Discussion **27**

4. Overview of measuring results - charge-induced magnetic moment variation **29**

5. Nanocrystalline Co **31**
5.1. Electrochemical pre-characterization 31
5.2. Charge-induced variation of magnetic moment 33
5.3. Influence of charging on hysteresis 37
5.4. Discussion 38

6. Nanocrystalline Pd **41**
6.1. Electrochemical pre-characterization 41
6.2. Charge-induced variation of magnetic moment 42
6.3. Discussion 44

7. Nanocrystalline FePd **47**
7.1. Electrochemical pre-characterization 47
7.2. Charge-induced variation of magnetic moment of $Fe_{20}Pd_{80}$ 48
7.3. Charge-induced variation of magnetic moment of $Fe_{50}Pd_{50}$ 55
7.4. Discussion 64

8. Maghemite/platinum nanocomposites **67**
8.1. Magnetic pre-characterization 67
8.2. Electrochemical pre-characterization 70
8.3. Charge-induced variation of magnetic moment 71
8.3.1. Pseudocapacitive charging 71
8.3.2. Charging in chemisorption regime 75
8.4. Discussion 77
8.5. Comparison with magnetic tunability of multiferroics 80

9. Nanocrystalline FePt **83**
9.1. Structural characterization by X-ray diffraction and Transmission Electron Microscopy 84
9.2. Magnetic pre-characterization 86
9.3. Ligand removal and electrochemical pre-characterization of chemically synthesized FePt 89

9.4. Charge-induced variation of magnetic moment 90
9.5. Discussion 94

10.Reference measurements of in-situ charging in SQUID 97
10.1. Diamagnetic response of electrochemical cell 97
10.2. Charge-dependent magnetic moment of reference sample 98
10.3. Discussion 99
10.3.1. Effect of charging current 99
10.3.2. Effect of cell 102
10.3.3. Comparison with magnetic measurements on nanocrystalline samples 102

11.Charge-induced resistance variation of nanoporous Au 105
11.1. Experimental Results 105
11.2. Discussion 107

12. Summary 115

13. Appendix 119
13.1. Nanocrystalline Co - supplementary data 119
13.1.1. Influence of charging on coercitivity 121
13.2. Nanocrystalline Pd - supplementary data 122
13.3. Nanocrystalline FePd - supplementary data 122
13.3.1. $Fe_{20}Pd_{80}$ 122
13.3.2. $Fe_{50}Pd_{50}$ 125
13.3.2.1. Voltage regime for 2-electrode charging 125
13.3.2.2. In-situ charging in SQUID 125
13.4. Nanocrystalline FePt - supplementary data 129
13.4.1. Basic chemical synthesis route of FePt 129
13.4.2. Ligand exchange 131
13.4.3. Ligand removal by utilisation of forming gas 132
13.4.4. Charging of chemically synthesized FePt 132
13.5. Effect of charging current - supplementary data 134

Acknowledgements 137

Bibliography 139

Abstract

Influencing magnetism and electrical resistance reversibly by applying a voltage is of great interest for new and innovative electronic devices. An alternative niche approach may emerge with the concept of charging of nanocrystalline materials with a high surface-to-volume ratio by means of electrolytes.

The present work investigates various ways to tune the magnetic moment and the electrical resistance of porous nanoscaled metals and metal oxide/metal nanocomposites immersed in an electrolyte by charging. The studied structures comprise nanocrystalline Pd, FePd and Co prepared by crystallite condensation in inertgas as well as nanoporous Au received from electrochemical dealloying. In addition nanocrystalline FePt is synthesized via chemical route for charging purposes. Electrochemical charging is performed with alkaline electrolytes. All samples are pre-characterized electrochemically for the determination of the charging regimes where a special focus was laid on charging in chemically sensitive regimes.

Extending the charging process to the regime of adsorption and desorption of oxygen yields a reversible variation of the magnetic moment in maghemite/platinum (γ-Fe_2O_3/Pt) of more than 10 % and of the electrical resistance in nanoporous Au of up to 43 %. Positive charging of γ-Fe_2O_3/Pt leads to a decrease of the magnetic moment while negative charging increases it. The variation of the magnetic moment is assigned to an electrochemically induced surface transition. This also holds for Co, however, the charge-induced variation of the magnetic moment is with 0.7 % significantly smaller compared to γ-Fe_2O_3/Pt as charging only influences the low magnetic Co-oxide surface. Chemically synthesized FePt exhibits the smallest variation of the magnetic moment but yields nevertheless the highest charge-coefficient of all investigated samples which can be assinged to the significantly smaller particle size. For Pd an increase of the magnetic moment with positive charging is observed which is in contrast to the findings for γ-Fe_2O_3/Pt and Co due to the domi-

nation of charge transfer processes on the Pd surface. FePd exhibits a maximum relative variation of the magnetic moment of 1.83 %. The variation of the magnetic moment with charge is strongly dependent on the magnetic field and changes the sign.

In nanoporous Au positive charging increases the resistance while negative charging decreases the resistance. The observed effect can be understood with additional scattering centers reversibly introduced by positive electrochemical charging which influence the electrical resistance. A comparison of the relative variations of resistance R and magnetic moment m reveals that R is more sensitive to charging than m, since electron-scattering selectively probes metal-electrolyte interfaces which are modified by charging. In contrast to that m represents a volume-averaged value where only the surface-shell part is sensitive to charging.

Die Schaltbarkeit von Magnetismus und elektrischem Widerstand durch Anlegen einer elektrischen Spannung ist für die Entwicklung von neuartigen, innovativen Applikationen im Bereich der Elektronik von großem Interesse. Die ladungsinduzierte Beeinflussung von nanokristallinen Materialien mittels Elektrolyten stellt ein vielversprechendes Konzept für mögliche Nischenanwendungen dar.

Die vorliegende Arbeit untersucht verschiedene Möglichkeiten, um das magnetische Moment sowie den elektrischen Widerstand von nanoskaligen Metallen und Metall/Metalloxid Nanokompositen durch elektrolytische Beladung zu beeinflussen. Die Untersuchungen umfassen Pd, FePd und Co, die mittels Kristallitkondensation in Inertgas hergestellt wurden, sowie nanoporöse Au-Proben, welche durch elektrochemisches Ätzen erzeugt wurden. Weiters wurden zum Zwecke der Beladung FePt-Nanopartikel mit einem chemischen Verfahren synthetisiert. Die elektrochemische Beladung wurde mit alkalinen Elektrolyten durchgeführt. Alle Proben wurden mittels elektrochemischer Verfahren vorcharakterisiert, um geeignete Spannungsbereiche für die elektrochemische Beladung zu bestimmen. Dabei wurde der Fokus auf chemisch besonders empfindliche Spannungsbereiche gelegt.

Die Erweiterung des Beladungsprozesses in Bereiche von Adsorption und Desorption von Sauerstoff führte zu einer Variation von über 10 % des magnetischen Moments in Maghemit/Platin Kompositen (γ-Fe_2O_3/Pt) und von 43 % des elektrischen Widerstands in nanoporösem Au. Positive Beladung senkt das magnetische Moment in γ-Fe_2O_3/Pt während negative Beladung das magnetische Moment erhöht. Dies wird elektrochemisch induzierten Oberflächenänderungen zugeschrieben. Die selbe Beobachtung wird bei Co gemacht, jedoch ist die ladungsinduzierte Änderung mit 0.7 % deutlich kleiner verglichen mit γ-Fe_2O_3/Pt, da durch Beladung bei Co nur die schwach magnetische, oxidierte Oberfläche beeinflusst werden kann. Durch chemische Synthese gewonnenes FePt weist die geringfügigste Änderung des magnetischen Moments auf, jedoch ist der Beladungskoeffizient höher als für alle anderen untersuchten Materialien. Dies beruht vermutlich auf der wesentlich kleineren Kristallitgröße, die durch den chemischen Syntheseprozess erzielten werden kann. Im Gegensatz zu γ-Fe_2O_3/Pt und Co steigt das magnetische Moment von Pd bei positiver Beladung an und sinkt bei negativer Beladung. Dies kann mit der Dominanz von Ladungstransferreaktionen auf der Pd-Oberfläche verstanden werden. FePd weist eine maximale, relative Variation des magnetischen Moments von 1.83 % auf. Der Vorzeichenwechsel des Beladungskoeffizienten deutet auf eine Feldabhängigkeit des beladungsinduzierten Effekts bei FePd hin.

In nanoporösem Au erhöht positive Beladung den Widerstand, während negative Beladung den Widerstand senkt. Dieser Effekt kann durch zusätzliche Streuzentren verstanden werden, die bei positiver elektrochemischer Beladung eingebracht werden. Ein Vergleich der relativen Änderungen von Widerstand R und magnetischem Moment m zeigt, dass R empfindlicher auf ladungs-induzierte Änderungen reagiert als m. Dies liegt darin begründet, dass der elektrische Widerstand durch die Streuung an den Metall-Elektrolyt Grenzflächen kontrolliert wird, während das magnetische Moment eine Volumengewichtete Größe darstellt, die durch Beladung nur entsprechend des Volumenanteils der Oberflächenschicht beeinflusst wird.

Part I.

Introduction and Experimental

CHAPTER 1

Introduction

Today's technology shows a more and more increasing demand for novel materials to achieve advances in the fields of information technology, biotechnology, data storage and many more. One key challenge is to find materials the properties of which can be tuned reversibly upon applying a voltage. Many endeavours have been performed especially in the field of magnetic data storage. With the implementation of the spin in microelectronic devices, so called spintronics, a further degree of freedom in addition to the mainly charge-driven devices could be obtained [1]. First spintronic devices can already be found in computer harddisks where the reading head works according to the principle of the 'Giant Magneto Resistance' (Nobel prize in physics, 2007). In addition to that the development in the field of sensors and actors demands for more and more novel material classes to meet today's requirements in science and industry [2, 3].

Ongoing efforts aim at an entire fusion of the semiconductor technology with ferromagnetic metals with the focus on the realization of pioneering spintronic devices [4]. As an example EuO can be given which exhibits a Curie-Temperature T_c of 67 K. In the focus of research are the improvement of the electron spin polarization as well as the fabrication of a fully functional spintronic transistor device [1].

Aiming at the further development of spintronic devices, novel material classes are seeked for the magnetic moment of which can be tuned by voltage. One promising material class are multiferroic materials. Ferroelectric properties in connection with ferromagnetic properties allow tuning the magnetization by applying an electric field and vice versa via the mechanism of magnetoelectric coupling [3, 5]. Single phase materials with these

properties are rare. As an example bismuth ferrite ($BiFeO_3$) or cromium oxide (Cr_2O_3) can be given. Due to strain coupling one can influence the crystallographic structure, as for example in $La_{0.67}Sr_{0.33}MnO_3/BaTiO_3$ structures [3]. Such structures and others comparable to that might lead to technological leaps, for example in hard disk writing heads as proposed by Kleemann [6].

Another possibility for tuning the magnetic moment in materials is the chemical modification of the surface with organic ligands [7]. Sun et al. [8] synthesized FePt-nanoparticles via a polyol process with a diameter of 4 nm and coated by oleic acid/oleylamine cappings. These cappings separate each single particle so that the FePt particles exhibit superparamagnetic properties. Thermal treatment induces a phase transition in FePt from chemically disordered fcc to a chemically ordered fct structure [8, 9]. In the work of Mikami et al. [7] reversible tuning of the magnetic moment was achieved by functionalization of maghemite nanoparticles with azobenzene-containing amphiphilic compounds. Alternating illumination with visible and UV-light leads to a reversible variation of 9 % of the relative magnetic moment due to cis-/trans photoisomerization [7].

Gleiter et al. [10] developed a novel approach for tuning the properties of materials by charging in an aqueous electrolyte. In connection with a high surface-to-volume ratio - resulting from the use of slightly compacted nanocrystalline metal powders - it becomes possible to influence the properties of metals. Several material properties have already been tuned successfully. Weissmüller et al. [2] demonstrated a reversible strain in Pt induced by charging in aqueous electrolytes with a maximum relative variation of the length l by $\Delta l/l = 0.15\,\%$. Resistance tuning was demonstrated by Sagmeister et al. [11] for nanocrystalline Pt in 1 molar potassium chloride (1-M KOH) with a maximum relative resistance variation $\Delta R/R$ of 8 %. Mishra et al. [12] achieved a relative resistance variation $\Delta R/R$ of 7 % in nanoporous Au, received from dealloying. The work of Drings et al. [13] reports reversible magnetic susceptibility tuning of nanocrystaline Pd in 1-M KOH up to 1 %. Ghosh et al. [14] observed a relative variation of the magnetic moment in CoPd of up to 1 % with an opposite sign of change compared to the results of Drings.

The present work investigates the charging effect on Pd, FePd-alloys and Co in aqueous electrolytes. The metals are synthesized by nanocrystallite condensation in inertgas. With this technique an average crystallite size of 10 nm can be achieved [15, 16]. The charging experiments, which aim at tuning the magnetic moment, are performed in 1-molar potassium hydroxide (1-M KOH). In comparison to earlier work on this topic, the charging

range is extended to regimes sensitive to adsorption and desorption of oxygen. Chemical synthesis methods enable the production of very small and highly monodisperse FePt nanocrystallites with oleic acid/oleylamine coating [8]. Due to the smaller crystallite size of chemically synthesized FePt a more pronounced charging effect compared to nanoparticles from crystallite condensation in inertgas is expected. The surface configuration of FePt is varied by ligand exchange [17, 18] and studied by SQUID magnetometry. Ligand removal of oleic acid/oleylamine [18] enables charging experiments on FePt. First measuring approaches on FePt after defined washing cycles are demonstrated. The studies are further extended for the first time to charging experiments on metal oxides, in particular maghemite (γ-Fe_2O_3). γ-Fe_2O_3 was synthesized by microwave plasma synthesis with a narrow particle size distibution and a small particle size [19, 20]. As charging of pure γ-Fe_2O_3 is unfeasible due the electrically isolating properties a γ-Fe_2O_3/Pt-composite is produced for charging purposes. In γ-Fe_2O_3/Pt mainly the regimes with electrochemical surface reactions are adressed and investigated. For the sake of comparison with the charge-induced variation of the magnetic moment in magnetic materials, the charge-induced variation of the electrical resistance in nanoscaled Au is studied as well. The nanoporous Au is synthesized by dealloying, i.e., electrochemical etching of AgAu-master alloys. The charging experiments for nanoporous Au are performed in 1-M KOH as for the magnetic materials.

CHAPTER 2

Physical Basics

The present chapter shortly summarizes the physical concepts related to this doctoral thesis. Focus will be laid on the novel concepts of charge-induced property tuning (section 2.1) and the concept of dealloying (section 2.2).

2.1. Charge-induced property tuning of metals

The concept of property tuning of nanophase metals by means of electrochemical charging was first proposed by Gleiter et al. [10]. Let us first consider the picture of a capacitor: Upon applying a voltage U between two electrodes which are separated by a dielectric interlayer with a thickness d a charge

$$Q = \epsilon_0 \epsilon \frac{U}{d}, \tag{2.1}$$

is induced where ϵ and ϵ_0 denote the relative dielectric constant and the dielectric constant of the vacuum, respectively [10, 21].

Q is located in the surface region with a thickness δ, the so-called electric screening length (see Fig. 2.1).

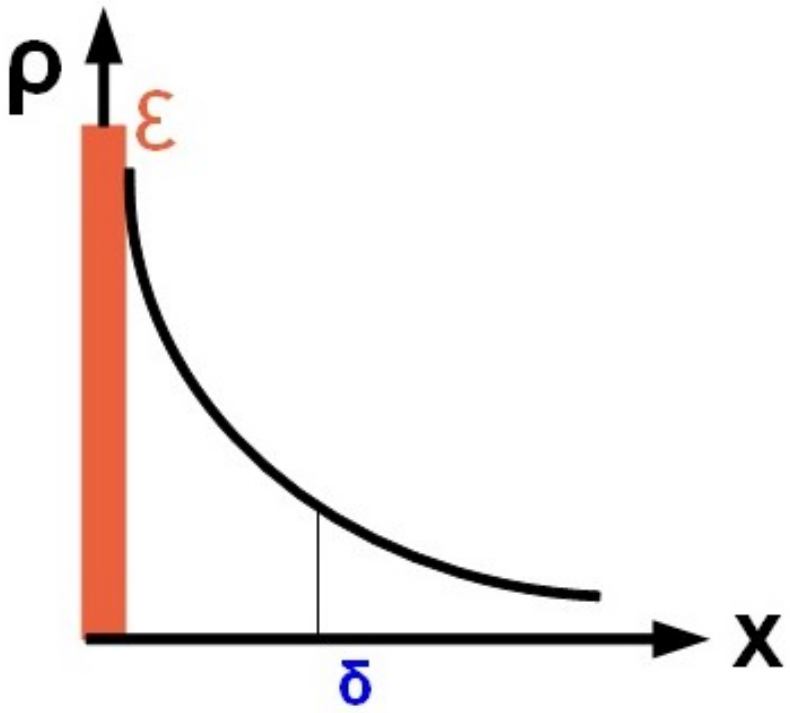

Figure 2.1.: Illustration of the screening length in materials with the help of one schematic capacitor plate: ρ denotes the charge density resulting from an applied voltage U and x denotes the depth profile of a material; with the screening length δ one can estimate the penetration depth of a charge. ϵ represents the dielectric constant for an interlayer between the capacitor plates.

In the case of semiconductors δ varies typically from 10 to 1000 lattice constants and can be estimated with [10, 22]

$$\delta = \sqrt{\frac{2\epsilon_0 \epsilon U}{ne}}, \tag{2.2}$$

where n denotes the charge carrrier density per volume and e the elementary charge .

However, these large penetration depths can not be reached in metals due to the high charge carrier densitiy. As a result of that applying a charge U to a conventional metal is not sufficient to influence macroscopic electronic properties in contrast to semiconductors. With the use of nanostructured materials the surface-to-volume ratio is strongly enlarged. In connection with applying high surface charge carrier densities via electrolytic charging it becomes possible to tune the electronic properties of the material. The advantage of electrochemical charging is shown by the following comparison: Applying a voltage of 5 V to SiO_2 as dielectric with an assumed thickness $d = 10\,\text{nm}$ and $\epsilon = 3.8$ corresponds

to a maximum charge of $Q = 0.02\,\mathrm{As/m^2}$ while charging with an aqueous electrolyte at a voltage $U = 1.2\,\mathrm{V}$ supports a charge $Q = 0.3\,\mathrm{As/m^2}$ (for charging in double layer regime see section 3.2.1.1). Due to electrochemical charging it is not necessary to employ a dielectric interlayer [10].

2.2. Formation of nanoporous structures by dealloying

In compacted nanocrystalline powder samples grain boundaries are controlling properties but are affected by charging to a minor extent only [11, 23, 24]. It is desirable to find materials with a grain size in the range of μm along with a porosity in the range of nm. Dealloying is a promising approach for creating such nanoporous structures. Due to the reduced number of grain boundaries compared to nanocrystalline materials one can expect a stronger influence of charging on the material properties for nanoporous (dealloyed) structures.

The basic idea is to remove the less noble component by immersing the master alloy in a suitable electrolyte. Upon applying an appropriate voltage the less noble component is removed from the master alloy. The noble component remains in the electrolyte as a nanoporous structure [25, 26]. One can think of it as a sort of metal foam consisting of interconnected ligaments. In the present work this approach is applied to a Au-Ag master alloy. Au and Ag are well suited as master alloy as they are perfectly miscible [27]. Surface diffusivity plays an important role in this morphological process. XRD measurements in literature [28] report 30 - 40 nm for the ligament size. However, Jin et al. [24] report a crystallite size of nanoporous Au down to 1-2 nm which is subject to grain coarsening. The influence of grain coarsening can result from mechanical strain due to adsorption/desorption processes of oxygen or might be a result of surface diffusivity.

A model for describing qualitatively the dealloying mechanism in AuAg-alloys is presented by Erlebacher et al. [25]. Due to the slow bulk mass transfer it can be assumed that the morphology is determined by processes in the alloy−electrolyte interface. Upon removing a Ag atom from the master alloy, this site is exposed to a lower number of Ag neighbours compared to other sites and leaves behind Au atoms with no lateral coordination. Before removing one further Ag layer, Au atoms form local clusters upon surface diffusion. The removal of the Ag atoms from undealloyed regions on the surface leads to a further size increase of these Au clusters. These clusters become undercut during the ongoing dealloy-

ing of the underlying alloy. Along with that the surface area is increased. The coalescence of Au atoms can be understood by the significantly higher concentration of Au adatoms in the alloy−electrolyte interface after removing the Ag atoms electrochemically. This leads to a strong driving force in oppostion to the concentration gradient of Au-atoms which forms Au-clusters. This behaviour is analogous to a 'spinodal decomposition' [25].

2.3. Magnetism in metal oxides

This chapter briefly summarizes the complex theory of magnetism in transition metal oxides. In the focus are the exchange interactions and spin order structures which are relevant for metal oxides, especially maghemite which is an important material class studied in the experimental section.

In metal oxides no direct exchange interactions as in metals are possible due to the large distances. Magnetic order structures in metal oxides mainly result from two exchange interactions [29]: i) superexchange interaction, ii) double exchange interaction.

The spinell structure basically consists of a face-centered cubic lattice of oxygen ions (see Fig. 2.2). 1/8 of the tetrahedral sites (A-sites) and 1/2 of the octahedral sites (B-sites) are occupied with cations. In a regular spinell structure with the structure $(X)_A[Y_2]_BO_4$ one cation species ('X-cations') occupies the tetrahedral sites and the second ('Y-cations') occupies the octahedral sites. The unit cell consists of 8 such formula units. The structure of the most prominent magnetic material, the magnetite is a so called inverse spinell. In the inverse spinell 1/8 of the tetrahedral sites is occupied with Fe^{3+}-ions and 1/4 of the octahedral sites is occupied by Fe^{3+}- and Fe^{2+}-ions. This is represented by the formula $(Fe^{3+})[\ Fe^{3+}\ Fe^{2+}]O_4$. The Fe^{3+} and Fe^{2+}-ions on the octahedral sites couple ferromagnetically via double exchange interaction while the Fe^{3+}-ions on the octahedral site exhibit antiferromagnetic coupling with the tetrahedral sites via superexchange interaction. As a result of that the contribution of the Fe^{3+}-ions to the magnetic moment m is cancelled out and only the Fe^{2+} ions contribute to m [30, 31].

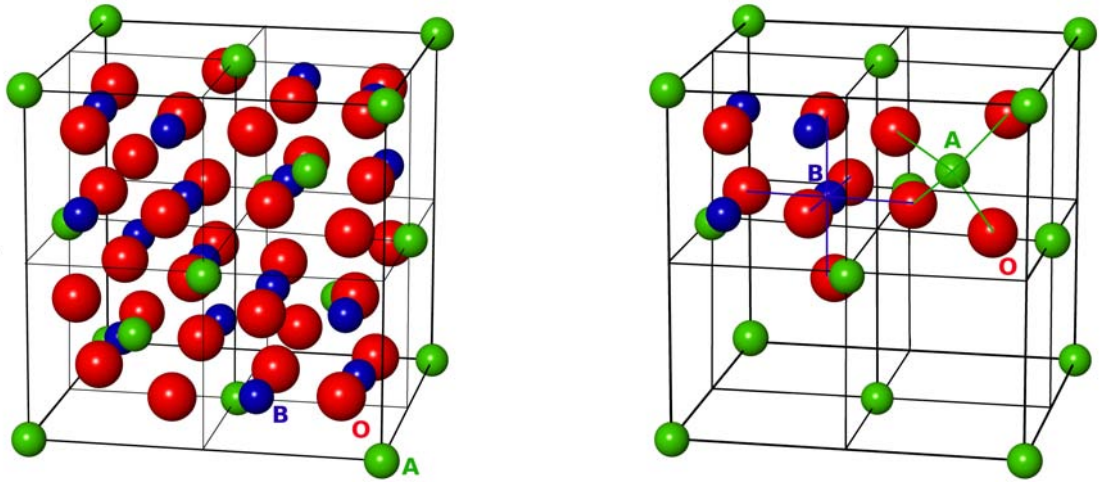

(a) unit cell of spinell

(b) illustration of two characteristic octants

Figure 2.2.: Unit cell of the spinell structure: (a) the oxygen atoms (O) form a cubic face-centered lattice. 1/8 of the tetrahedral sites and 1/2 of the octahedral sites are occupied with cations. (b) shows 2 octants of the unit cell for a better visualization of the structure [32].

This work has a focus on the iron oxide maghemite (γ-Fe_2O_3) which exhibits a structure related to that of magnetite (Fe_3O_4) [30, 33]. The γ-Fe_2O_3 is restricted to Fe^{3+}-ions. Oxygen exhibits an fcc-structure as in Fe_3O_4. All tetrahedral sites in the inverse spinell are occupied with Fe^{3+}-ions. The octahedral sites are only partially occupied, a remaining rest of the octahedral sites are vacancies which is represented by the formula $(Fe^{3+})[Fe^{3+}{}_{\frac{5}{3}}\,\square_{\frac{1}{3}}]O_4$. The Fe^{3+}-ions couple antiferromagnetically via superexchange interaction and do not contribute to the net magnetization. Due to the non-stoichiometric vacancies only 2/3 Fe^{3+}-ions with no partner ion for superexchange coupling contribute to the net magnetic moment [30, 33]. 2/3 of the Fe^{3+}-ions corresponds to a magnetic moment of $2/3 \cdot 5\mu_B = 3.33\mu_B$ for γ-Fe_2O_3 [34]. The Fe^{2+}-ions in Fe_3O_4 correspond to a magnetic moment of $4\mu_B$ [34] so that the magnetization for maghemite is lower than for magnetite.

CHAPTER 3

Experimental procedures

In the following chapter the methods for the synthesis of nanoscaled materials as well as the experimental setup for electrochemical characterization and measuring in dependence of charging are described.

3.1. Synthesis

The nanoparticle synthesis procedures comprise chemical and physical synthesis routes. FePt was synthesized chemically with a ligand coating while the metal powders Co, Pd and FePd were synthesized by means of nanocrystallite condensation in inertgas.

3.1.1. Chemical FePt-nanoparticle synthesis by hot-injection/polyol process

The synthesis of FePt mainly follows a method presented by Sun et al. [8]. FePt-nanoparticles are synthesized via a polyol process. For this purpose platinum acetylacetonate ($Pt(acac)_2$) is reduced and iron pentacarbonyl ($Fe(CO)_5$) is thermally decomposed. The addition of oleic acid and oleylamine stabilizes the nanocrystallites by forming a ligand shell. By means of this synthesis procedure chemically disordered fcc FePt nanoparticles are received which self-assemble in a hexagonal structure when deposited on substrates (see Fig. 9.2). The synthesis of FePt was performed at the Institute of Theoretical and Physical Chemistry with the support of Stephan Landgraf. The synthesis was performed in a fume hood. The detailed recipe and process of synthesis is decribed in the appendix (section 13.4).

3.1.2. Nanoparticle formation by condensation in inertgas

Nanoparticle formation by means of the so called inertgas condensation, IGC represents a physical synthesis method for nanocrystalline materials. With this method particle sizes of $\sim$10 nm can be achieved. Fig. 3.1 illustrates the experimental setup of an inertgas condensation facility.

Highly pure metal wires ($\geq$99.95 [%]) are placed in a tungsten crucible. The recipient for the production is evacuated down to 10^{-8} mbar. The wires are vaporized by Joule heating which is achieved by connecting the tungsten crucible to a power supply up to 4 kW[1]. Upon evaporation metal aerosols are formed near the source by homogeneous nucleation. Growth is effected by coalescence and incorporation of atoms from the gas phase [15, 16].

The metal aerosols are transported to the surface of a liquid nitrogen cooled stainless steel cylinder by means of convection and thermophoresis. With a stainless steel foil the powder is subsequently removed and collected in a transfer boat below the stainless steel cylinder. Via a transfer line the boat can be transported after reevacuation from the production chamber to the transfer chamber. The boat with the powder is moved above a lock with a small glass tube attached. Upon turning around the boat for 180 ° the powder falls into the glass tube. The lock can be sealed manually and then transported to the glove box for storage and further handling.

3.1.2.1. Powder preparation for charging experiments

As described in the sections 3.1.1 and 3.1.2 powder is gained for the experiments in the SQUID. For electrochemical charging the nanocrystalline powder has to be compacted slightly. For that purpose an extrusion die with a diameter of 3 mm is manufactured from stainless steel with two properly fitting counter dies for compaction. The die was specially designed to prepare pellets suitable for the in-situ SQUID measurements. Due to the strong sensitivity to air the powder is transferred into the extrusion die directly in the glove box. With the counter die the powder is slightly pre-compacted by hand under Argon. After that the extrusion die with the pre-compacted powder is locked out from the glove box and mounted into a bench vise. With the bench vise the final compaction of the powder is carried out manually. The diameter of the pellets is 3.0 mm and the thickness ca. 0.5 mm.

[1] The provided current is at the order of several 100 A but the voltage below a half volt in operating mode.

(a) View on the nanoparticle synthesis facility

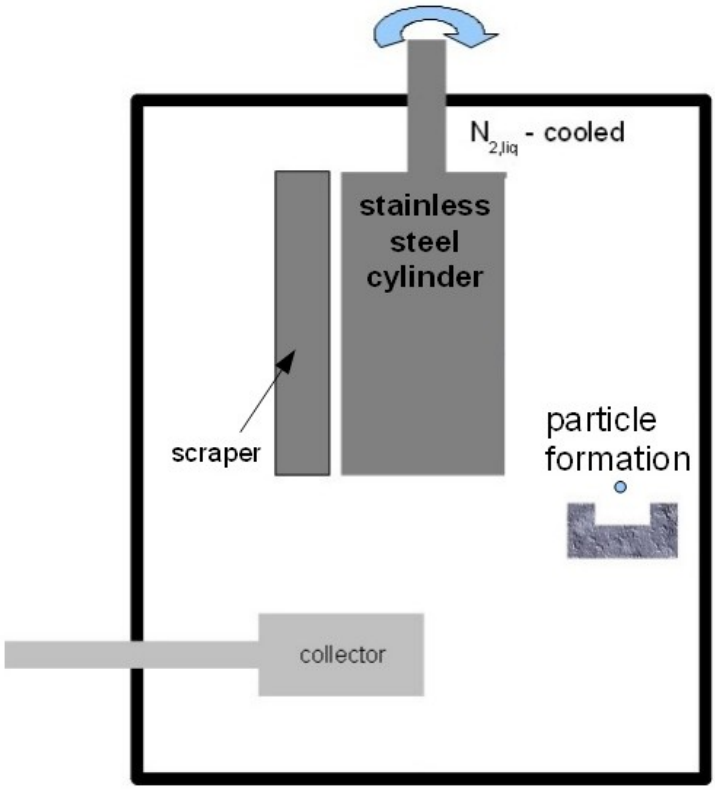

(b) scheme for inertgas condensation synthesis process

Figure 3.1.: View on the nanoparticle synthesis facility including a schematic illustration of the IGC-synthesis process.

3.2. Electrochemical characterization methods

Electrochemical investigations are performed in the standard three electrode geometry: i) working electrode (WE), ii) counter electrode (CE), and iii) reference electrode (RE). All three electrodes are connected to a potentiostat which is operated in potentiostatic mode. For pre-characterizations the potentiostats Voltalab PGZ 100 (Radiometer Analytical) and the potentiostat AUTOLAB PGSTAT128N (EcoChemie) are in use, for measuring at the SQUID only the Voltalab PGZ 100 is used. The WE is connected to the sample to be investigated. All potential and current settings are adjusted with respect to the WE. The voltage is set in reference to the RE.

The present work mainly focuses on two electrochemical methods: i) cyclovoltammetry and ii) chronoamperometry.

3.2.1. Cyclovoltammetry

Cyclovoltammetry is a widely spread quasi-stationary method in electrochemistry for the investigation of materials in electrolytes [35]. Between the WE and the RE a triangular voltage sequence with a pre-defined scan rate $\frac{dU}{dt} = \nu$ is applied. Plotting the voltage U vs. I yields the so-called cyclovoltammogram which allows the characterization and classificaton of electrochemical surface processes [35, 36]. In the present case the focus is on nanostructured materials which exhibt large surface-to-volume ratios. As chemical processes are supposed to be rather slow due to the large surfaces, rather small scan rates between $100\,\mu\mathrm{V/s}$ and $5\,\mathrm{mV/s}$ are chosen.

When discussing a cyclovoltammogram one mainly divides into three different regimes: i) the double layer regime, ii) the chemisorption regime and iii) the pseudocapacitive regime.

3.2.1.1. Double layer regime

Fig. 3.2 illustrates the three regimes in a Pt-cyclovoltammogram (Chempur, 20-40 $\mathrm{m^2\,g^{-1}}$). Double layer charging can be understood in terms of capacitive charging. A voltage is applied to the WE and charged either positively or negatively while charge carriers from the electrolyte of opposite sign settle on the surface, forming a Helmholtz-double layer [35]. This yields higher capacities compared to conventional capacitors as the distance between the charges is only slightly more than the radius of the solvated ion and the specific surface

of nanoscaled materials is rather high (up to $40\,m^2\ g^{-1}$ in the case of Pt) [10].

3.2.1.2. Chemisorption regime

In the chemisorption regime chemical surface reactions take place. In the case of aqueous electrolytes the most prominent example in the positive anodic branch is the adsorption of oxygen species. Upon reversing the voltage in the cathodic direction desorption occurs at a threshold voltage U_{thresh}. Adsorption and desorption processes are characterized by peaks and/or plateaus in the cyclovoltammogram. As can be seen in Fig. 3.2 adsorption and desorption are not completely symmetric. There is a voltage difference between adsorption and desorption, the so called 'overpotential'. This means that in the case of oxygen adsorption, the desorption occurs not immediately upon voltage reversal, but desorption is shifted towards values of reduced voltage in cathodic direction [35, 36].

3.2.1.3. Pseudocapacitive charging regime

Pseudocapacitive charging, a concept presented in recent literature [23], occurs when subsequent cycling in the adsorption regime of an oxide covered sample surface is performed without reaching the desorption regime. The oxide on the sample surface remains in place and the charge transfer to the sample is dominated by capacitive processes. However, a contribution from weakly bound ions which adsorb and desorb during subsequent cycling is supposed to add the capacitive processes [23].

3.2.2. Chronoamperometry

Chronoamperometry (CA) is rather common in electrochemistry for the investigation of potential jumps [37]. In the course of this work a constant potential is applied for charging the nanostructured metals/metal oxides and keeping the charge Q for a certain time t. Under standard conditions it is operated in 3-electrode geometry: the current flow is monitored between WE and CE, the potential is set between WE and RE. The current I between WE and CE is monitored by the potentiostat and plotted vs. t. After a certain time the charging voltage U is varied by a potential step. The influence of this potential step on the nanostructured materials is recorded concurrently. The current I decreases exponentially; the charging time t strongly depends on the charging regime and approaches exponentially a limiting value. One can always detect a certain leakage

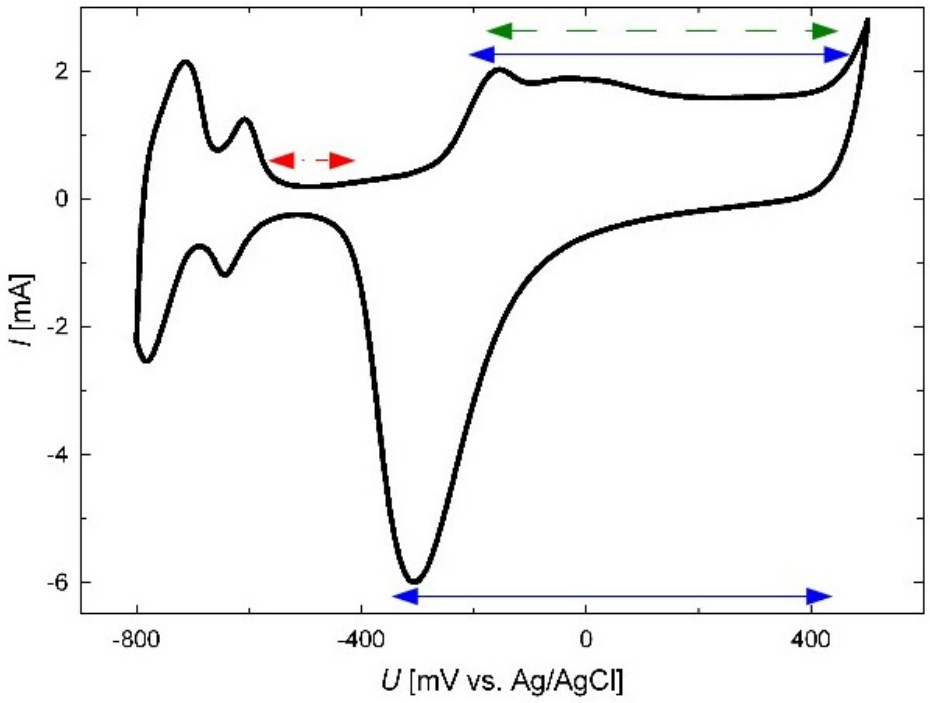

Figure 3.2.: Illustration of double layer regime, chemisorption regime and pseudocapacitive charging regime with the help of a cyclovoltammogramm of nanocrystalline Pt in 1M KOH, scan rate 500 μV/sec. The red dashed-dotted, blue-full and green-dashed line indicates the double layer regime, oxygen adsorption/desorption regime and pseudocapacitive regime, respectively.

current I_{leak} which has to be assigned to (not nearer detectable) electrochemical reactions at the sample surface or at higher potentials to electrolysis.

With t and I the charge ΔQ per potential step can be determined by integration. For this purpose the charge due to the leakage current has to be subtracted [13]:

$$\Delta Q = \int_0^{t_{meas}} [I(t) - \lim_{t\to\infty} I]dt \tag{3.1}$$

t_{meas} denotes the duration of the measurement and is chosen in a way that I decays to a constant value (I_{leak}) so that the equation above can be rewritten as [13]

$$\Delta Q = \int_0^{t_{meas}} I(t)dt - I_{leak}t_{meas}. \tag{3.2}$$

Consecutive charging steps of ΔQ_i yield the total applied charge

$$Q = \sum_i \Delta Q_i. \tag{3.3}$$

The determination of Q is performed automatically by a computer programme from Patrick Wahl. I_{leak} is determined by averaging over the last 10 % of the measurement steps. For a reliable determination of I_{leak}, an exponential current decay of more than 90 % is required. Fig. 3.3 shows an exemplary CA curve for nanocrystalline Pt (Chempur, 20-40 m^2/g). Decay occurs not always exponentially; especially when charging in chemically sensitive regimes strong deviations are possible.

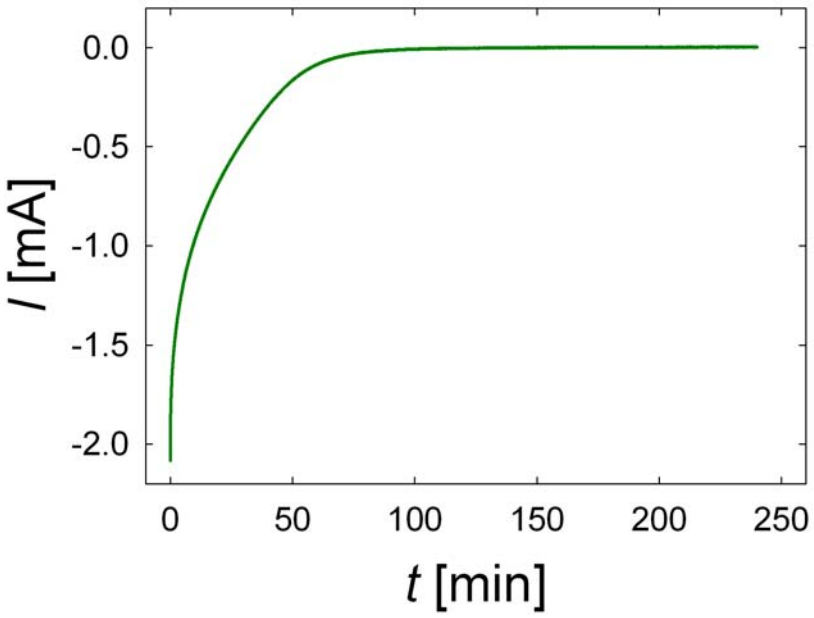

Figure 3.3.: Chronoamperomtetric charging curve of nanocrystalline Pt at a charging voltage of -300 mV.

As the magnetic charging experiments are performed in-situ in SQUID it is not possible to apply a RE during these measurements due to the restricted space ($\approx$ 3 mm working space). This requires careful pre-characterizations to obtain comparable voltages for charging only with WE and CE. Before starting the in-situ measurements, a pre-characterization setup with a non-sealed electrochemical cell, including the WE, in an electrolyte bath is performed. CE and RE are also immersed in the electrolyte and connected to the potentiostat. All measurements are performed with the charging voltage set with respect to the RE, denoted as U_{WE-RE}. The voltage between WE and CE, denoted as U_{WE-CE}, is recorded concurrently. Due to Ohm's law the recorded values U_{WE-CE} exhibit an exponential decay which reaches a plateau. The U_{WE-CE} from the plateau is then applied for the in-situ charging experiments. With this method one obtains a reasonably well approximation of the electrochemical 3-electrode state for 2-electrode charging purposes.

3.3. SQUID magnetometry

This section describes the magnetic measurements performed by means of the SQUID (Super Conducting Quantum Interference Device)-magnetometer (Quantum Design MPMS-

XL-7). All measurements are performed at the Graz Karl-Franzenzs University in the group of Heinz Krenn. According to the manufacturers' instructions the SQUID used for the measurements exhibits a measuring error of 10^{-8} emu[2] at magnetic fields smaller than 2.5 kOe and of 6×10^{-7} emu at magnetic fields up to 70 kOe (maximum field).

Measurements of the magnetic moment in SQUID are performed by magnetizing a sample in the sample chamber with a homogeneous magnetic field which is generated by a superconducting magnet. In the center of the magnetic field a superconducting coil is located. The sample is moved in discrete steps through the detection coil and induces a current proportional to the variation of the magnetic flux. This current is coupled inductively to the SQUID sensor by means of one further superconducting coil which is connected in series to the detection coil. The SQUID sensor consists of a superconducting ring which is interrupted by a non-superconducting Josephson contact (see Fig. 3.4). Variations of the magnetic flux induce a change of the current in the SQUID-sensor. This current is detected for each sensor signal with the help of an oscillating circuit. As a result of that the SQUID detects a voltage signal in dependence of the sample position. With a fit routine the magnetic moment is calculated under the assumption of a point-shaped magnetic dipole [38].

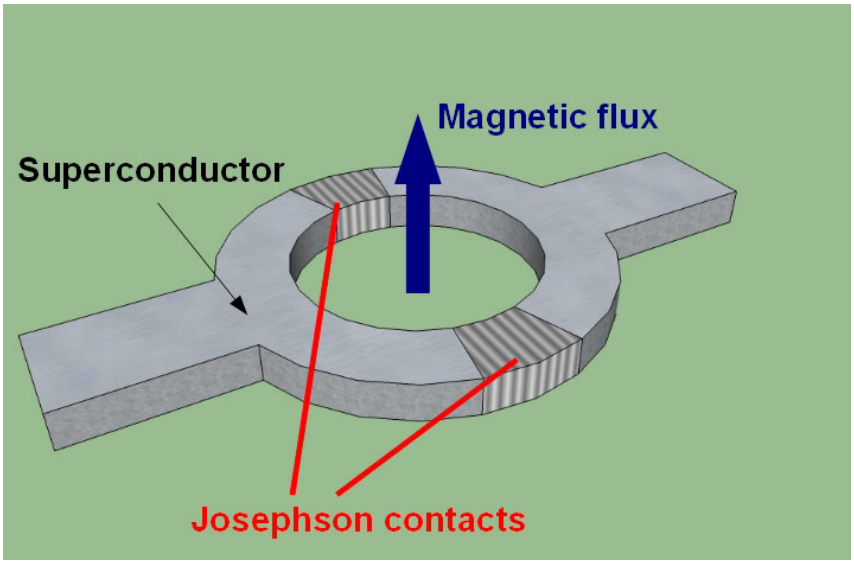

Figure 3.4.: Scheme of the SQUID sensor with two Josephson contacts in a SQUID magnetometer.

The SQUID sample holder is a plastic tube which is affixed to a transfer rod. Powder samples are filled in specially designed capsules which are placed in the lower third of the

[2] 1 emu corresponds to $10^{-3}\ \frac{A}{m^2}$.

straw. To ensure proper operation the sample holder is additionally fixed by tape. As high magnetic fields could make a magnetic powder sample move during the measurement, cotton is added to fix the powder in the capsule. For the handling of the electrochemical cells see the sections 3.1.2.1 and 3.3.1. A scan amplitude of 6 cm is used; 64 data points are recorded and 1 scan per measurement is performed.

For the standard magnetic characterization mainly three methods were applied: i) determination of the magnetic moment, ii) hysteresis measurements and iii) zero field cooling/field cooling (ZFC/FC).

3.3.1. Design of an electrochemical cell for in-situ charging

All charging experiments on magnetic materials are performed in the SQUID (Quantum Design MPMS-XL-7) described above. This requires an electrochemical cell design suitable for in-situ measurements in the SQUID. Fig. 3.5 shows a scheme of electrochemical cell. The electrodes of the electrochemical cell placed in the SQUID are contacted directly to the potentiostat for in-situ measurements. Apart from the sample all components of the cell must be made of diamagnetic materials so that the ferro- or paramagnetic measuring signal can be fully assigned to the sample. As a result of that the cell body consists of PTFE. For the electrical contacts Au-wires (Chempur, 99.9 % pure, diameter 0.25 mm) are used. Highly porous carbon tissue (Epcos, Standardtuch 99) serves as counter electrode and is coiled with Au-wire (diameter 0.25 mm). The sample is placed in the center of the electrochemical cell after coiling with a Au-wire (diameter 0.1 mm). WE and CE are electronically separated by a battery separator (Freudenberg, FS 2226). Both the battery separator and the carbon clothing are arranged concentrically around the pellet and rinsed with the electrolyte.

3.4. Dealloying and resistance measurement of nanoporous Au

The measurements, evaluations and discussions on nanoporous Au were done by Patrick Wahl within the framework of his master thesis under my co-supervision [39]. Text and figures presented in section 3.4 and chapter 11 are taken from the published article [40] with the permission of the editor.

The master alloy $Ag_{75}Au_{25}$ (at.%) was prepared from high purity Au and Ag ingot material (wires of purity 99.9 %) by arc-melting and subsequent homogenization at 950 °C for more

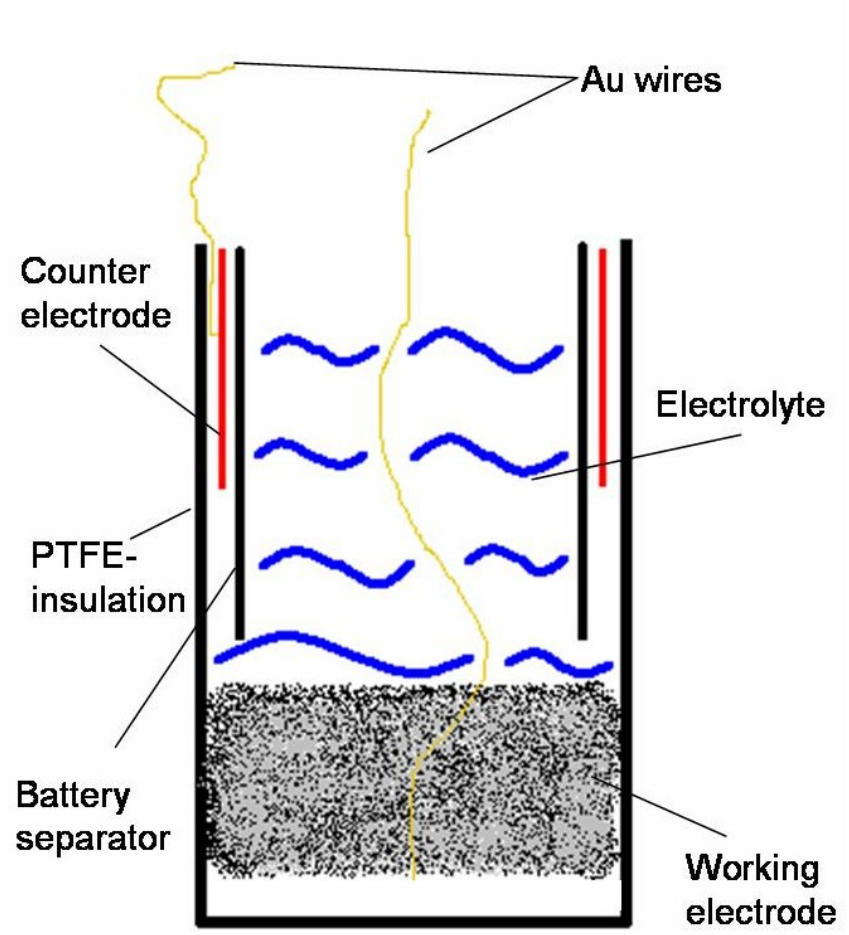

Figure 3.5.: Scheme of an electrochemical cell for in-situ SQUID-measurements

than 70 h (see [24]). Thin foils were obtained by rolling to a thickness of ca. 100 μm. Between the rolling steps and afterwards, the samples were annealed several times at 600 °C for 2 h. For dealloying stripes with dimensions of ca. $20 \times 5 \times 0.1$ mm^3 were cut. Different dealloying procedures were applied in order to prepare nanoporous Au without oxygen adsorption layer (sample sets I denoted "pure" in the following) and with an initial oxygen adsorption layer (sample set II, denoted "oxygen adsorbed" in the following).

Sample set I of pure nanoporous Au was prepared by dealloying the $Ag_{75}Au_{25}$ master alloy in diluted HNO_3 (volume ratio: 1:2) under potentiostatic control vs. Ag/AgCl reference electrode. In order to avoid precipitation of Ag during dealloying, 1-molar KNO_3 was used as salt bridge between the HNO_3 electrolyte and the 1-molar KCl reference electrode. A tungsten rod (diameter 1 mm) was used as the counter electrode. The dealloying was performed at a voltage of +1.30 V vs. Ag/AgCl and stopped after ca. 5h when the current fell below a threshold of 1 mA. After the dealloying process the sample was removed and rinsed with destilled water. The samples for set II (oxygen-adsorbed sample) were dealloyed in 1-molar $HClO_4$ solution at a constant potential of +0.75 V (versus Ag/AgCl in 1-molar $HClO_4$) as described previously [24]. After dealloying, a higher potential (+0.85 V) was applied for a few hours to further stabilize the structure size. The ligament size of the nanoporous Au samples is in the range of 20 nm [24].

The resistance measurements were performed in a standard electrochemical cell at ambient temperature using a potentiostat PGZ-100 (Voltalab Comp.) for charging with the specimen being immersed in an aqueous electrolyte solution of 1-molar KOH. The nanoporous Au specimen for resistance measurements served as working electrode. A commercial Pt-electrode (Radiometer Analytical) was used as counter electrode and a Ag/AgCl electrode (saturated KCl; Radiometer Analytical) as reference electrode. The dc electrical resistance was measured in situ in the cell by means of the 4-point method using a high-precision source- and multimeter Type 2400 (Keithley Comp.). For contacting the np-Au sample, soft springs made of Au wires (diameter 0.25 mm, Chempur, purity 99.9%) were used, four electrodes for the resistance measurement and one for charging.

Charging of the pure np-Au sample (I) was performed by multistep chrono-amperometric measurements. The voltage applied to the work electrode was incremented in steps of 100 mV at intervals of 2 min in the double layer regime and $3-30$ min in the chemisorption regime. For each step, the charge quantity was determined by integrating the charging current making a correction for the leak current of 40 μA in the double layer regime

and up to 250 μA in the chemisorption regime. In order to minimize errors due to this leak current, which may arise from Faraday current, the electrical resistance was recorded with a measuring current of 100 mA. Data points of the resistance were taken at the end of each charging interval when a constant value was attained. By reversing the sign of the measuring current it was further checked that the charging current did not affect the resistance measurement. Prior to the measuring run, cyclo-voltammograms with scan rates of 1 mV/s were recorded in order to choose the appropriate potential range for charging in the double-layer regime or in the regime of specific adsorption.

The resistance of the np Au-sample with the initial oxygen adsorbate (II) was monitored concurrently during cyclovoltammetric scanning. In this case, the charge in dependence of charging voltage was determined separately by chrono-amperometric measurements.

Part II.

Results and Discussion

CHAPTER 4

Overview of measuring results - charge-induced magnetic moment variation

The present section summarizes the measurements on the nanostructured materials in dependence of charging at varying magnetic fields. The preparation methods are presented in chapter 3. Tab. 4.1 summarizes the data for all investigated materials of the thesis. In the table the charge-induced variation of the magnetic moment Δm is depicted. For a better comparison of the various material classes, the relative variation of the magnetic moment $\Delta m/m_{ref}$ is presented along with the average imposed charge ΔQ at the respective fields. m_{ref} corresponds to the first measured magnetic data point. In addition the charge-coefficient $\beta = \frac{d(m/m_{ref})}{dQ}$ compares the response of the respective materials on charging (see also first paragraph of chapter 5).

Δm is presented in two physical units: i) in emu g^{-1} for a better comparison of the absolute magnetic moment variations of the respective materials and ii) in emu for studying the influence of the experimental setup on the measurements. Depicting Δm in emu allows a comparison with Δm_{coil}, which represents the influence of current loops in the SQUID due to the electrochemical cell design (for a further discussion see section 10.3). With the help of these consideration it is possible to evaluate the reliability of Δm received from the measurements (see section 10.3.1).

Sample	H **[Oe]**	Δm **[emu]**	Δm $[\frac{emu}{g}]$	$\frac{\Delta m}{m_{ref}}$ **[%]**	Q $[\frac{C}{g}]$	I_{leak} **[μA]**	Δm_{coil} **[emu]**	$d(m/m_{ref})/dQ$ $[\frac{g}{C}]$
Co	50	0.71×10^{-5}	0.78×10^{-3}	0.68	10.61	146	1.72×10^{-6}	-6.76×10^{-4}
	500	4.61×10^{-5}	4.89×10^{-3}	0.30	9.90	101	1.19×10^{-6}	-3.05×10^{-4}
	5,000	9.36×10^{-5}	9.86×10^{-3}	0.14	2.63	96	1.13×10^{-6}	-5.32×10^{-4}
	50,000	7.79×10^{-5}	8.27×10^{-3}	0.10	1.02	72	0.85×10^{-6}	-7.34×10^{-4}
Pd	200	0.76×10^{-5}	0.36×10^{-3}	5.30	22.97	906	1.13×10^{-5}	2.35×10^{-3}
	2,000	2.50×10^{-5}	2.63×10^{-3}	12.30	30.68	1,130	1.33×10^{-5}	1.78×10^{-3}
$Fe_{20}Pd_{80}$	70,000	2.97×10^{-4}	7.30×10^{-2}	0.33	26.11	118	1.39×10^{-6}	-0.11×10^{-4}
	20,000	1.60×10^{-4}	2.30×10^{-2}	0.09	20.34	121	1.43×10^{-6}	-0.56×10^{-4}
	2,000	1.05×10^{-4}	1.50×10^{-2}	0.06	19.29	128	1.51×10^{-6}	-0.38×10^{-4}
	200	0.67×10^{-4}	-1.00×10^{-2}	0.09	19.03	128	1.51×10^{-6}	0.95×10^{-4}
	20	0.26×10^{-4}	-1.50×10^{-2}	0.91	18.20	156	1.84×10^{-6}	2.84×10^{-4}
$Fe_{50}Pd_{50}$	20	0.69×10^{-4}	0.40×10^{-2}	1.83	42.50	406	4.78×10^{-6}	1.17×10^{-4}
	200	0.49×10^{-4}	0.40×10^{-2}	0.07	43.32	240	2.78×10^{-6}	0.14×10^{-4}
	2,000	2.64×10^{-4}	2.30×10^{-2}	0.12	42.23	260	3.02×10^{-6}	-0.28×10^{-4}
	20,000	6.29×10^{-4}	5.50×10^{-2}	0.22	42.56	240	2.88×10^{-6}	-0.53×10^{-4}
FePt 'chemroute'	500	0.06×10^{-4}	0.55×10^{-3}	0.18	0.08	9	1.03×10^{-7}	-9.12×10^{-3}
	5,000	0.03×10^{-4}	0.29×10^{-3}	0.02	0.07	8	0.98×10^{-7}	-1.85×10^{-3}
	50,000	1.07×10^{-4}	9.90×10^{-3}	0.16	0.08	9	1.01×10^{-7}	-4.73×10^{-3}
γ-Fe_2O_3/Pt -	50	0.98×10^{-6}	3.73×10^{-5}	0.33	3.88	544	6.40×10^{-6}	-6.59×10^{-4}
pseudocapacitive	500	1.38×10^{-6}	7.38×10^{-5}	0.05	2.94	143	1.69×10^{-6}	-1.85×10^{-4}
	5,000	4.73×10^{-6}	24.42×10^{-5}	0.02	2.67	116	1.37×10^{-6}	-0.84×10^{-4}
γ-Fe_2O_3/Pt -	5	2.31×10^{-5}	6.09×10^{-4}	10.20	63.93	776	9.14×10^{-6}	-1.75×10^{-3}
chemisorption	50	8.25×10^{-5}	0.17×10^{-2}	7.88	62.36	768	9.05×10^{-6}	-1.35×10^{-3}
	500	3.06×10^{-4}	1.86×10^{-2}	8.05	64.84	749	8.83×10^{-6}	-1.18×10^{-3}
	5,000	3.46×10^{-3}	6.97×10^{-2}	6.24	60.41	1,165	1.37×10^{-5}	-1.10×10^{-3}
	50,000	1.16×10^{-2}	5.71×10^{-2}	10.40	66.24	747	8.80×10^{-6}	-1.68×10^{-3}
C-tissue (reference)	1,000	-1.93×10^{-5}	-	-	-	257	3.02×10^{-6}	-
	5,000	0.16×10^{-5}	-	-	-	231	2.72×10^{-6}	-
	50,000	1.06×10^{-5}	-	-	-	204	2.40×10^{-6}	-

Table 4.1.: Summary of the charge-induced variation of the magnetic moment of nanocrystalline metals and metal oxides studied in the present thesis. H: magnetic field; Δm: absolute charge-induced variation of the magnetic moment m; $\Delta m/m_{ref}$: absolute value of relative charge-induced variation of m with respect to the first data point; Q: imposed charge; $\beta = \frac{d(m/m_{ref})}{dQ}$: charging coefficient; I_{leak}: maximum leakage current during CA; Δm_{coil}: variation of m induced by leakage current in current loop (estimated according to Eq. 10.1); I_{leak} corresponds to the maximum leakage current flowing during in-situ charging in SQUID; m_{ref} denotes the first measured data point to which all following data points are referred.

CHAPTER 5

Nanocrystalline Co

Co nanoparticles are synthesized by means of nanocrystallite condensation in inertgas and subsequent slight compacting for charging. The experimental procedure for in-situ SQUID measurements follows the descriptions in the sections 3.1.2.1 and 3.3.1. The weight of the sample amounts to 8.83 mg. Measurements were performed at magnetic fields between 50 Oe and 50 kOe. For all measurements the voltage is alternated in 2-electrode geometry between +1100 mV, which corresponds to oxygen adsorption, and −750 mV, which corresponds to the desorption of oxygen according to reference measurements in 3-electrode geometry. From the linear fit of $\Delta m/m_{ref}$ the charge coefficient $\beta = \frac{d(m/m_{ref})}{dQ}$ is deduced. β characterizes the sensitivity with respect to charging and is used throughout the thesis for comparison of the various investigated materials.

5.1. Electrochemical pre-characterization

For pre-characterization a cyclovoltammogram is recorded with a scan rate of 150 μV/sec. In the focus of interest is the study of the influence of adsorbed oxygen on the Co surface which can be removed reversibly. The oxygen adsorption and desorption regimes are indicated in Fig. 5.1.

In anodic direction three charging regimes occur which can be attributed to the chemical reactions described in the following [41]. At -800 mV the reaction

$$\mathrm{Co} + \mathrm{OH}^- \rightarrow \mathrm{Co(OH)}_{\mathrm{ads}} + e^- \tag{5.1}$$

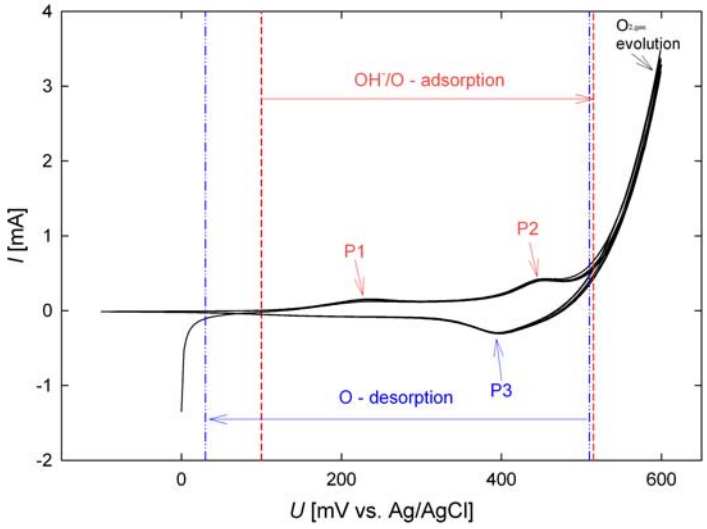

Figure 5.1.: Cyclovoltammogram of nanocrystalline Co recorded with a scan rate of 150 μV/sec

occurs (not shown in Fig. 5.1).

Upon cycling in anodic direction a passive film of CoO according to

$$\mathrm{Co(OH)_{ads}} + \mathrm{OH^-} \rightarrow \mathrm{CoO} + \mathrm{H_2O} + e^- \tag{5.2}$$

as well as $\mathrm{Co(OH)_2}$ according to

$$\mathrm{Co(OH)_{ads}} + \mathrm{OH^-} \rightarrow \mathrm{Co(OH)_2} + e^- \tag{5.3}$$

is formed [41].

At +200 mV the peak P1 evolves which is caused by the conversion of the outer layer of the oxide film at the oxide-solution interface into Co(II)/Co(III) oxide [41]:

$$\begin{aligned} \mathrm{Co(OH)_2} + \mathrm{OH^-} &\rightarrow \mathrm{CoOOH} + \mathrm{H_2O} + e^- \\ 3\mathrm{Co(OH)_2} + 2\mathrm{OH^-} &\rightarrow \mathrm{Co_3O_4} + 4\ \mathrm{H_2O} + 2\ e^-. \end{aligned} \tag{5.4}$$

P2 can be identified as the formation of Co(III) oxide $\mathrm{Co_2O_3}$ [41]:

$$2\ \mathrm{Co(OH)_2} + 2\ \mathrm{OH^-} \rightarrow \mathrm{Co_2O_3} + 3\ \mathrm{H_2O} + 2\ e^-. \tag{5.5}$$

According to Ismail et al. [41] this peak is localized at about +250 mV vs Ag/AgCl reference electrode. In Fig. 5.1 P2 is located at +450 mV which differs from the values of Ismail et al. [41]. The difference might be attributed to the different structure compared to that of Ismail et al. [41]. A Co rod is used for the measurements in [41] while in contrast to that, in the present studies Co is a porous structure made from compacted powder. For the CV in the present work, a scan rate of 150 μV/s is applied. In the work of Ismail et al. [41] a higher scan rate of 10 mV/s is used. In cathodic direction the overall desorped charge is smaller than in the anodic direction which indicates the formation of an irreversible passivation layer [41, 42]. Nevertheless the peak P3 occuring upon cycling in cathodic direction in Fig. 5.1 can be assigned to the reduction of the Co(III)-species exclusively. Reducing Co(II) is only possible at much more negative cathodic voltages (-1 V vs. Hg/HgO) [43]. The CV-sequences in the present work are not extended to such negative voltages.

U_{WE-RE} = +450 mV of P2 corresponds to a voltage of U_{WE-CE} = +1100 mV while the voltage for desorption U_{WE-RE} is +50 mV which corresponds to a voltage U_{WE-CE} of 0 mV. However, in order to guarantee a quantitative desorption of oxygen, a voltage U_{WE-CE} of -750 mV is chosen for the 2-electrode setup during SQUID-magnetometry. Setting a more negative value can be performed easily as Fig. 5.1 shows no significant chemical activities in the measured range. Briefly one can say that oxygen adsorption in 2-electrode geometry is achieved upon applying +1100 mV while oxygen desorption is achieved upon applying -750 mV (CA). Integrating current over time in the CA-curve yields the transferred charge of each cycle.

5.2. Charge-induced variation of magnetic moment

The charge-induced tuning is performed at magnetic fields from 50 Oe to 50 kOe. Here and in the following the diamagnetic contribution from the electrochemical cell has been subtracted (see chapter 10). The charging experiments in the SQUID were performed with the same type of electrolyte (1M KOH) as used for pre-characterization. The detailed m-U and m-Q characteristics are presented only for the magnetic field of 5 kOe. The complete data set can be found in the appendix (section 13.1).

During the experiment the charging voltage U is varied between -750 mV and +1100 mV. Positive charging leads to a decrease of the magnetic moment m while negative charging

increases it (Fig. 5.2). Measurements in all four magnetic fields exhibit qualitatively the same characteristic behaviour of Co, however with different amplitudes of variations of m. Here and in the following m exhibits case by case a linear drift with time. The same holds for the charge Q. These drifts are subtracted as linear background from the data both in the presentation and the evaluation of the m-Q characteristics.

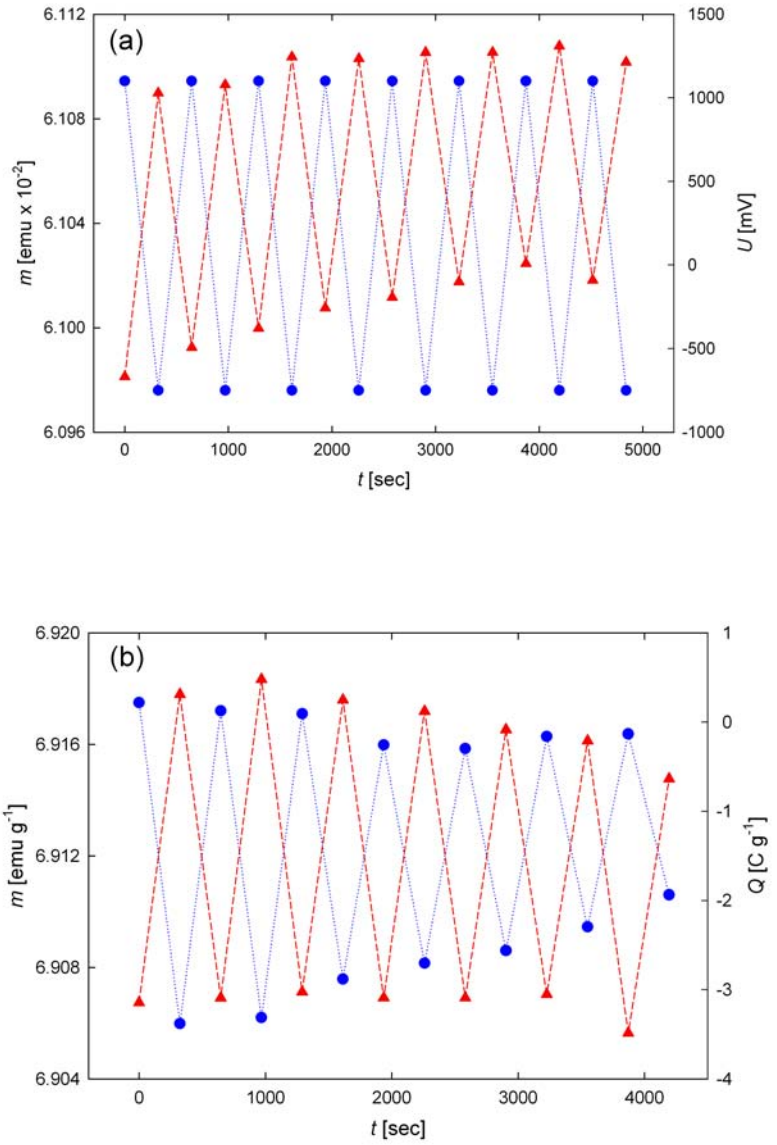

Figure 5.2.: Magnetic moment m (▲) of nanocrystalline Co measured at 5 kOe upon consecutive adsorption-desorption cycling: (a) charging voltage U (●), (b) imposed charge Q (●). t: time; m, Q in (b) drift-corrected, see text.

From the variation of m with Q for $H = 5\,\mathrm{kOe}$ (Fig. 5.3) a charge coefficient $\beta = \frac{d(m/m_{ref})}{dQ}$ can be derived. The corresponding plots for 50 Oe, 500 Oe, and 50 kOe can be found in the appendix.

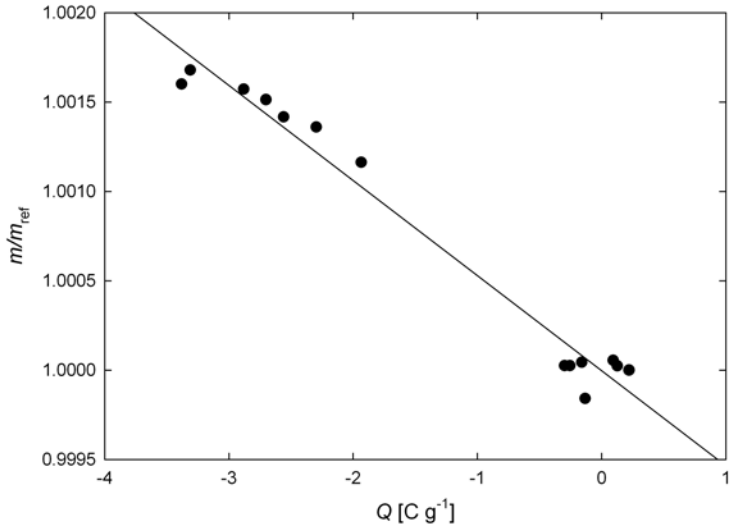

Figure 5.3.: Magnetic moment m in dependence of Q with a linear regression fit for the calculation of $\frac{dm}{dQ}$ at 5 kOe (m, Q drift-corrected).

Fig. 5.4 depicts the field-dependence of the charge-induced variation of the magnetic moment m. The magnetic moment m shows a sigmoidal increase with the applied magnetic field (Fig. 5.4 (a)). The variation of the magnetic moment Δm follows the same trend (Fig. 5.4 (b)). An exception is present at 50 kOe where Δm is slightly smaller compared to the maximum at 5 kOe. The relative change of the magnetic moment $\frac{\Delta m}{m_{ref}}$ decreases with the applied magnetic field H (Fig. 5.4 (c). The maximum $\Delta m/m_{ref}$ is observed at 50 Oe with 0.68 %. m_{ref} always refers to the first measured magnetic data point. β is rather similar at 50 Oe and 5 kOe while a minimum of the β occurs at 500 Oe (Fig. 5.4 (d)). This means that the sensibility of m on charging is highest at 50 Oe and 50 kOe. β is negative for all magnetic settings. In the following β will be used to characterize the response of the respective system on charging: $\beta < 0$ denotes a decrease of m with positive charging and an increase of m with negative charging; $\beta > 0$ denotes the opposite behaviour.

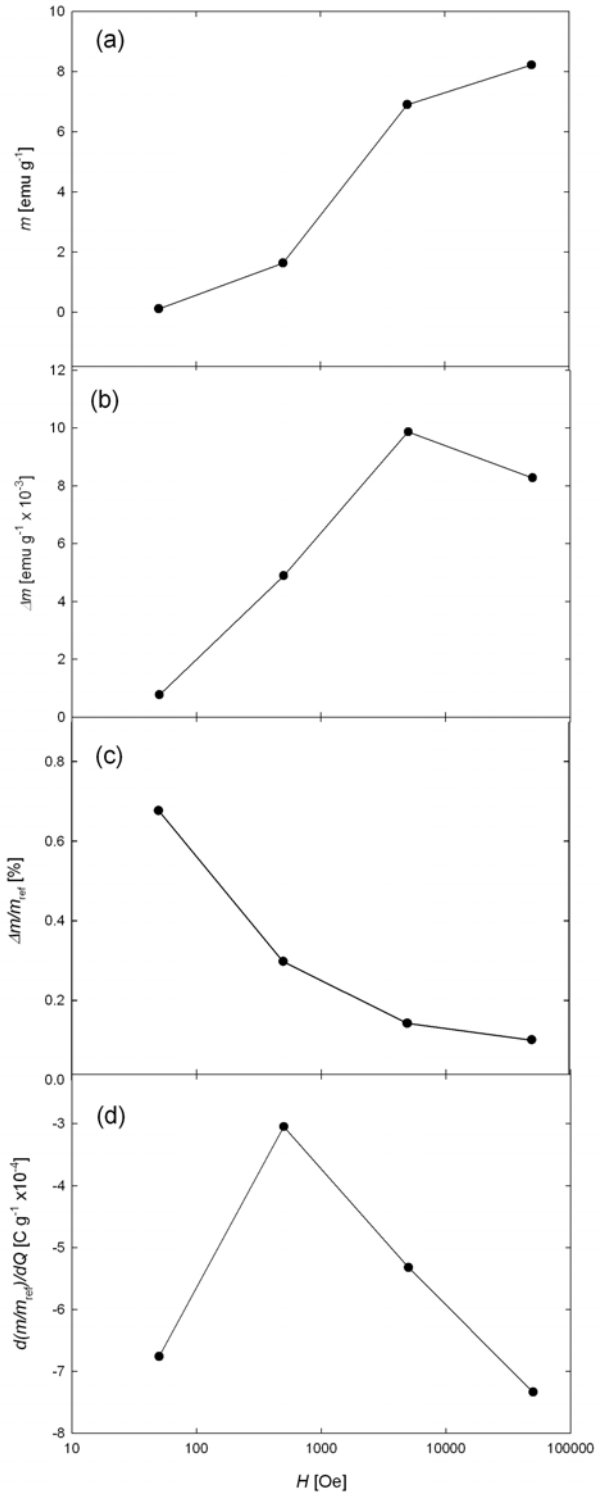

Figure 5.4.: Charge-induced variation of magnetic moment of Co upon cycling between -750 mV and +1100 mV in dependence of magnetic field H; (a) magnetic moment m, (b) variation Δm, (c) absolute value of relative variation $\Delta m/m_{ref}$ with m_{ref} denoting the first measured data point, (d) charge coefficient $\beta = \frac{d(m/m_{ref})}{dQ}$

H **[Oe]**	Δm $[\frac{emu}{g}]$	$\frac{\Delta m}{m_{ref}}$ **[%]**	$\frac{d(m/m_{ref})}{dQ}$ $[\frac{g}{C}]$	**Drift** $\frac{dQ}{dt}$ $[\frac{C}{g\ sec}]$	**Drift** $\frac{dm}{dt}$ $[\frac{emu}{g\ sec}]$	$r^2_{\frac{d(m/m_{ref})}{dQ}}$
50	7.76×10^{-4}	0.68	-6.76×10^{-4}	1.32×10^{-3}	7.62×10^{-7}	0.99
500	4.89×10^{-3}	0.30	-3.05×10^{-4}	no Drift	6.66×10^{-6}	0.83
5000	9.86×10^{-3}	0.14	-5.32×10^{-4}	-1.23×10^{-3}	1.04×10^{-6}	0.97
50000	8.27×10^{-3}	0.10	-7.34×10^{-4}	-4.08×10^{-4}	-1.24×10^{-6}	0.60

Table 5.1.: Charge-induced variation of magnetic moment; summary for Co. H denotes the magnetic field, Δm the variation of the magnetic moment m, $\frac{\Delta m}{m_{ref}}$ the relative variation of the magnetic moment where m_{ref} depicts the first measured data point in the sequence. $\beta = \frac{d(m/m_{ref})}{dQ}$: charge-coefficient, $\frac{dQ}{dt}$: charge drift, $\frac{dm}{dt}$: drift of m, r^2: variance of $\beta = \frac{d(m/m_{ref})}{dQ}$.

Tab. 5.1 summarizes the findings concerning the influence of an applied charge Q on the magnetic moment m. $\frac{dQ}{dt}$ decreases with rising magnetic field; at 500 Oe no drift of charge occurs. $\frac{dm}{dt}$ exhibits a decreasing trend with a sign change observed at 50 kOe. r^2 denotes the variance of the linear regression (obtained from the program 'Sigmaplot').

It is important to mention that upon raising H the imposed charge Q drops significantly. The reason could be a slow permeation of the electrolyte through the epoxy resin sealing after several hours of measurements under vacuum. Nevertheless the cell remained operable over a long measuring period so that other effects may also play a role as well. For instance it is well-known that voltage-induced desorption processes in electrolytes can significantly reduce the surface structure of a highly porous material [24]. Therefore one also has to bear in mind that consecutive adsorption/desorption processes induced on Co may decrease the overall surface and as a result of that the applied charge Q.

5.3. Influence of charging on hysteresis

In addition to the tuning of m it was attempted to reversibly influence the coercitivity of the Co sample by charging. At this time the sample already features some sort of aging effect concerning charging so that for the alternating charging sequence the adsorption voltage (anodic branch) has to be set to +1100 mV and the desorption voltage (cathodic branch) to -1100 mV. [1] Fig. 5.5 shows four hysteresis curves which are recorded with an alternating voltage of +1100 mV/-1100 mV (repeated twice).

Upon zooming into the positive flank of the magnetization curves around 0 Oe the hys-

[1] One reason for this aging could be loss of electrolyte due to permeation of the cell sealing since the SQUID operates under 25 mbar He-atmosphere.

teresis shows a splitting which can be assigned to each charging state, respectively.

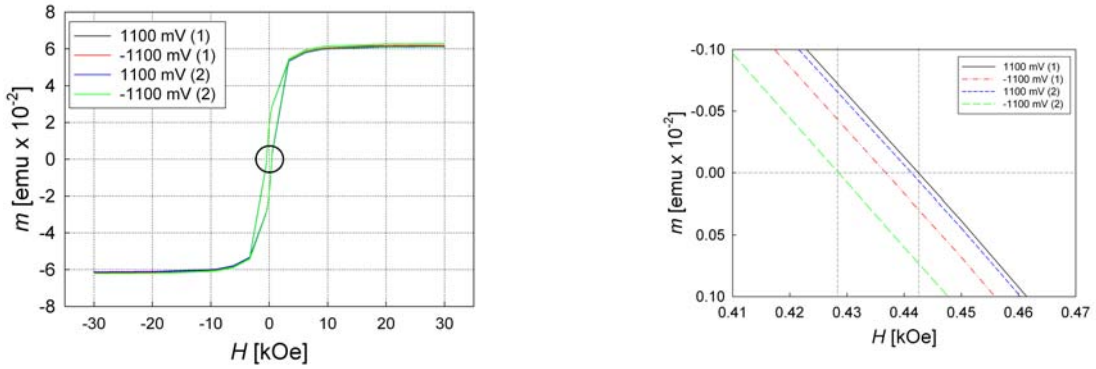

(a) full hysteresis curve of Co in the electrochemical cell

(b) positive hysteresis branch

Figure 5.5.: Charge-dependent hysteresis of Co; the black circle in (a) marks the range illustrated zoomed in (b). The associated negative flank is found in the appendix.

According to Fig 5.5 a systematic behaviour occurs in a way that positive charging leads to an enhancement of coercitivity H_c while negative charging tends to decrease it. One can observe an offset between positive slope and negative slope of the hysteresis loop. The charge-induced variation of the coercitivity H_c amounts to 8 Oe at the negative hysteresis flank and 14 Oe at the positive hysteresis flank.

5.4. Discussion

For nanocrystalline Co the charging coefficient β is negative for all field settings. In the present work this variation is discussed in terms of an electrochemically induced oxidation of the Co nanoparticle surface which can be partially reversed. Oxide formation on the Co nanoparticles is inevitable due to the exposure to air during constructing and sealing the electrochemical cell and during all electrochemical pre-chararcterizations performed on Co. In section 5.1 the surface reactions of Co in an KOH-environment are discussed on the basis of literature. Cyclovoltammetry in an alkaline environment is associated with at least four different Co-oxides/Co-hydroxides [41,44]: i) CoO, ii) Co_2O_3, iii) Co_3O_4 and iv) $Co(OH)_2$.

All Co-oxides/Co-hydroxides exhibit paramagnetic properties at room temperature [44]. The magnetic moment per Co atom of CoO, Co_2O_3, and $Co(OH)_2$ is 4.92 μ_B, 4.47 μ_B, and 4.88 μ_B, respectively, only Co_3O_4 is smaller with 2.79 μ_B. Co in CoO and $Co(OH)_2$ exhibits an oxidation state of 2+ while Co in Co_2O_3 has an oxidation state of 3+. In

Co_3O_4 Co^{2+} and Co^{3+} are present in the spinell-type structure of $Co^{2+}(Co_2^{3+})O_4$. Co^{3+} exhibits covalent bonding in the octahedral sites which is given as reason for the lower magnetic moment [44].

For the present studies variations of Co-oxides with chronoamperometric charging steps have to be discussed. Upon the adsorption of oxygen in anodic direction (+1100 mV in 2-electrode geometry) CoO and $Co(OH)_2$ are formed as a passivation film along with Co_3O_4 (P1 in Fig. 5.1). $Co(OH)_2$ is transformed to Co_2O_3 at higher voltages (P2 in Fig. 5.1) [41]. Upon inducing oxygen desorption with applying a voltage of -750 mV (2-electrode geometry) the peak P3 in Fig. 5.1 indicates a reduction of Co^3+ which goes hand in hand with an increase of the magnetic moment as the Co-oxides with Co^{2+} exhibit a higher magnetic moment than the Co-oxides with Co^{3+}-state [45]. A clear assessment whether a phase re-transformation of the oxides upon reversal of the voltage in cathodic direction takes place cannot be given. It is also not clarified which Co-oxides contribute to the variation of the magnetic moment. As Co_3O_4 and Co_2O_3 is formed as shell it is expected that the reduction of Co^{3+} in these two oxides gives the major part of the contribution. It must be emphasized here that charging in an alkaline environment makes it practically impossible to influence Co directly. The use of 1M-KOH is accompanied with the immediate formation of an oxide layer. Furthermore the list of Co-oxides is not exhaustive here; literature reports about CoOOH, $CoHO_2$ etc. are not further discussed here [41, 45].

Finally the maximum value of the charge-induced variation of m of 0.68 % at 50 Oe will be addressed. An estimation is given how large the variation of the magnetic moment of the Co-oxide layer is compared to the ferromagnetic signal of Co. The literature value for the magnetization of Co is 162.6 G cm^3 g^{-1} [46] while for Co_3O_4 3.7 G cm^3 g^{-1} can be estimated for 30 kOe [47][2]. This means that the signal of Co is a factor of 44 higher compared to the signal of Co-oxide. With the literature values for the magnetic moment of Co_2O_3 (4.47 μ_B) and Co_3O_4 (2.79 μ_B) [44], one can calculate a ratio of 1.6. With this ratio the magnetization of Co_2O_3 can be estimated with the help of the magnetization of Co_3O_4 and yields 5.9 G cm^3 g^{-1}. With the help of the simple picture of a spherical Co particle coated with a Co-oxide shell the volume fraction influenced by charging can be discussed. Assuming a particle radius of $r = 5$ nm and a Co-oxide shell thickness $\delta = 1$ nm the relative magnetization

[2]For this calculation example only Co_3O_4 is taken into consideration as this is better documented in literature compared to Co_2O_3 or $Co(OH)_2$

$$\frac{\Delta M}{M} = \frac{(M_{Co_2O_3} - M_{Co_3O_4}) \cdot \delta}{M_{Co} \cdot \frac{1}{3} r} = \frac{(5.9 - 3.7) \cdot 1}{162.6 \cdot \frac{1}{3} \cdot 5} \tag{5.6}$$

yields 0.81 %. This can be compared well with the maximum observed variation of 0.68 % at 50 Oe. The decrease of the relative variation of m with increasing field might be attributed to pinning of magnetic moments. Along with the partial exposition of the cobalt/cobalt oxide surface to the electrolyte due to compaction of the powder a further reducing influence on the charge-induced variation of m becomes plausible.

For future experiments it might be interesting to study the variation of m in a neutral environment as for example potassium chloride (KCl). The study of direct charging experiments on Co with a minimum of Co-oxides involved in the process is probably restricted to the use of non-aqueous electrolytes.

CHAPTER 6

Nanocrystalline Pd

For the electrochemical charging experiments Pd is synthesized by means of crystallite condensation in inertgas. As starting material for the crystallite condensation a Pd wire is used (Chempur; 99.95% pure; diameter 1 mm).

6.1. Electrochemical pre-characterization

The voltage regimes for oxygen adsorption and desorption on Pd are determined by means of cyclovoltammetry. Pre-characterizations as well as the magnetic measurements in dependence of charging were performed in 1-M KOH.

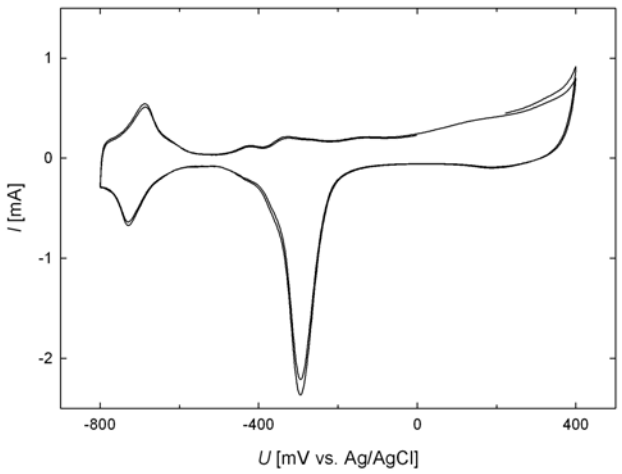

Figure 6.1.: Cyclovoltammogram of nanocrystalline Pd in 1-M KOH with a scan rate of $100\,\mu\mathrm{V\ sec}^{-1}$

The voltage range between -500 mV and -600 mV can be assigned to the double layer regime (Fig. 6.1). Below -600 mV in cathodic direction hydrogen adsorption is observed while in anodic direction the hydrogen is desorped. Hydrogen uptake can be excluded for the voltage regimes used in the present study. From +400 mV on in anodic direction oxygen species are adsorped which leads to the formation of PdO. PdO on the sample surface is identified with a subsequent current increase in anodic direction. At -300 mV electroreduction of PdO is represented by a peak in cathodic direction [48]. The experiment aims at the behaviour of Pd upon charging in the regime of chemisorption, e.g. adsorption and desorption of oxygen onto the Pd surface. For chronoamperometric charging two fix voltage values (vs. Ag/AgCl) are chosen: +200 mV in anodic direction for O-adsorption and -500 mV in cathodic direction for O-desorption. These voltages correspond in 2-electrode geometry to +1200 mV for adsorption and -400 mV for the desorption of oxygen.

6.2. Charge-induced variation of magnetic moment

The experimental procedure for the preparation of in-situ SQUID measurements follows the descriptions in section 3.1.2.1 and 3.3.1. The weight of the powder sample amounts to 21.4 mg.

Fig. 6.2 illustrates the dependence of Pd on charging in 1-M KOH at a field of 200 Oe. Positive charging increases the magnetic moment m while negative charging decreases it (see also Tab. 6.1). The observed variation of m is reversible. For 2 kOe (see appendix, 13.2) one can observe the same behaviour as for 200 Oe. However, it has to be mentioned that due to the small paramagnetic moment the charge-induced variation may be significantly effected by a current loop (see section 10.3). Below fields of 200 Oe no proper signal is received from SQUID and above 2 kOe the diamagnetism of the electrochemical cell becomes dominant. β is decreasing upon increasing the magnetic field. The charge coefficient $\beta = \frac{d(m/m_{ref})}{dQ}$ is positive for 200 Oe and 2 kOe. The maximum Q amounts to 30.68 C g^{-1}.

H **[Oe]**	Δm $[\frac{emu}{g}]$	$\frac{\Delta m}{m_{ref}}$ **[%]**	$\frac{d(m/m_{ref})}{dQ}$ $[\frac{g}{C}]$	$\frac{dQ}{dt}$ $[\frac{C}{g\ sec}]$	$\frac{dm}{dt}$ $[\frac{emu}{g\ sec}]$	$r^2_{\frac{d(m/m_{ref})}{dQ}}$
200	3.57×10^{-4}	5.3	2.35×10^{-3}	1.98×10^{-3}	no drift	0.99
2000	2.63×10^{-3}	12.3	1.78×10^{-3}	no drift	no drift	0.97

Table 6.1.: Charge-induced variation of magnetic moment; summary for Pd. For definition of symbols see Tab. 5.1.

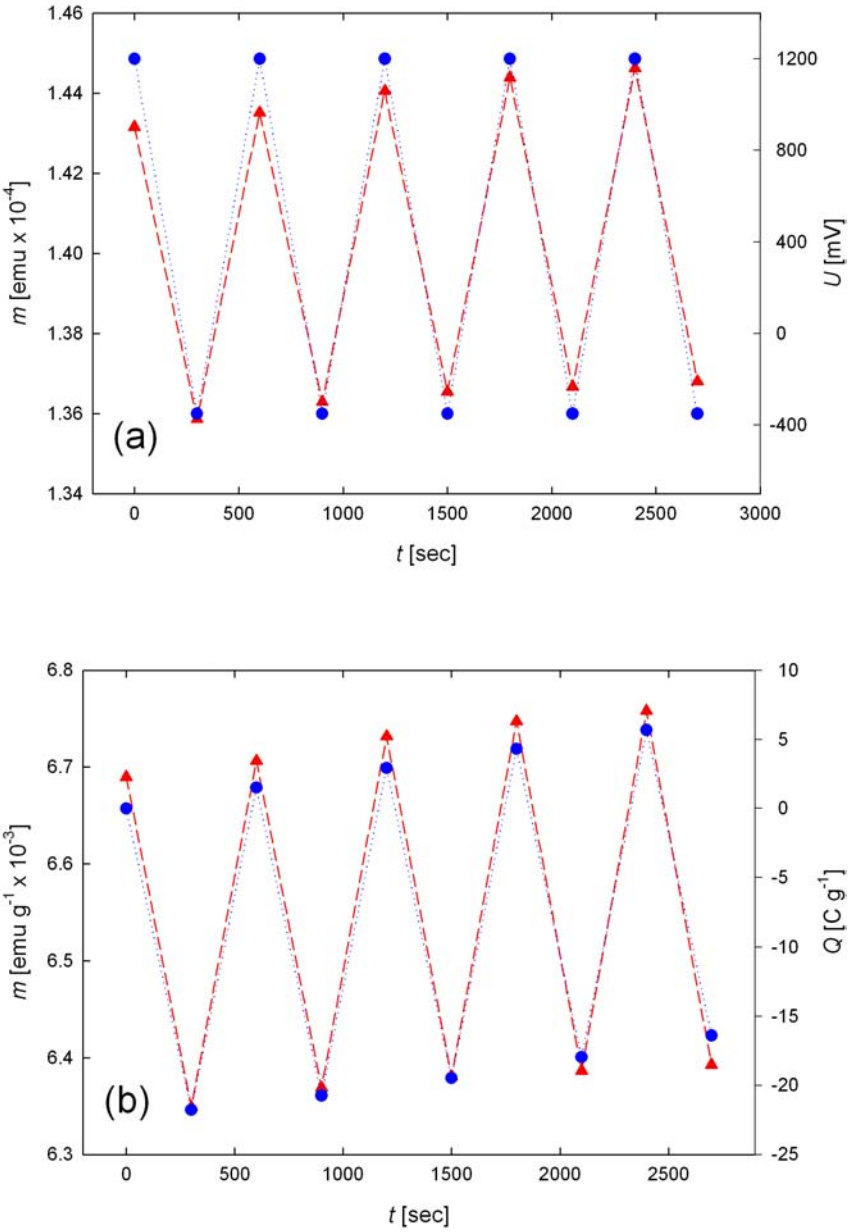

Figure 6.2.: Magnetic moment m (▲) of nanocrystalline Pd measured at 200 Oe upon consecutive adsorption-desorption cycling (a) charging voltage U (●), (b) imposed charge Q (●). m, Q in (b) drift-corrected.

6.3. Discussion

From a magnetic point of view Pd is a very interesting substance as its strong Stoner enhancement brings it near to the transistion to ferromagnetic behaviour [29]. Drings et al. [13] already investigated the tunability of nanocrystalline Pd in a magnetic field. The concept is based on influencing the Pd d-band by positive/negative charging. Positive charging decreases the number of electrons in the d-band which results in an increase of the magnetic moment m while negative charging decreases it. This behaviour can be understood with the Pauli susceptibility proportional to the density of states at the Fermi edge [13]. The work of Drings et al. [13] was focused on the double layer regime charging not taking into consideration the chemical regime in 1-M KOH electrolyte and was restricted to measurements at 90 kOe only. As a major result the variation of the magnetic susceptibility χ was varied reversibly upon charging by 1 % [13].

The present measurements performed on nanocrystalline Pd are extended to the chemical regime. The first (positive) voltage U of +1200 mV setting is assigned to oxygen adsorption while the negative voltage corresponds to -300 mV in 2-electrode geometry. Due to the low mass of 21.4 mg measurements at high magnetic fields (70 kOe) are disturbed by the diamagnetic background signal of the electrochemical cell components. This can be attributed to the deviation from a strictly linear behaviour of paramagnetic substances in a magnetic field while diamagnetic materials exhibit a linear response upon applied magnetic fields. At 200 Oe and 2 kOe the magnetic signal of Pd was detectable. This is of interest as in the work of Drings only measurements at 90 kOe are presented. Due to the extension to the oxygen adsorption and desorption regime a higher charge Q of 30 C g^{-1} can be applied to the sample (Drings et al. [13]: 15 C g^{-1}). The higher Q upon extending to the chemical regime is clear as adsorption and desorption are accompanied by higher currents in the CV which leads to a higher applied charge during in-situ CA. $\frac{d(m/m_{ref})}{dQ}$ is positive for both investigated field settings. $\frac{\Delta m}{m_{ref}}$ is found to be 5.34 % for 200 Oe and 12.3 % for 2 kOe [1]. The relative variation $\frac{\Delta \chi}{\chi_{ref}}$ of the susceptibility is estimated to 6 % which is 6× higher compared to the work of Drings[2]. Due to the high leakage current at the order of 1 mA a high influence of the cell current has to be accounted for. Therefore, the possible current loop influence is rather high for both field settings (see Tab. 4.1 and section 10.3). As a result of that the charge induced effects found for Pd in the present

[1] m_{ref} refers to the first measured magnetic data point.
[2] χ_{ref} denotes the susceptibility for the low-voltage charging state.

work have to be discussed with care.

It is obvious to assume that the model of influencing the Pd bandstructure plays also a role when extending the measurements to the chemisorption regime. The positive β for Pd is in contrast to the negative β observed for Co (see section 5.2). In the chemisorption regime charge transfer takes place in the anodic direction. O^{2-}-adsorption leads to a positively charged surface. Upon reversing to oxygen desorption in cathodic direction the charge is reversed. In addition to the charge-transfer model one has to bear in mind the electrochemically induced surface transformation to PdO in anodic direction [48]. As PdO is reported to be diamagnetic [49] one would expect an increase of m upon negative charging in negative direction which is not the case here. As positive charging increases m and negative charging decreases it, like in the double layer regime [13] the variation of m in the present chemical regime is obviously due to charge transfer and not due to surface transformations of Pd.

Upon summing up the considerations from above it turns out that for the present measurements the band-filling model still exhibits a fine explanation for the effects observed in the present work. The extension to the chemisorption regime allows the application of a charge $2\times$ higher compared to the work of Drings et al. [13]. This cannot explain that the observed effect is $6\times$ higher compared to [13]. An influence of possible surface modifications cannot be classified further. Moreover charge-induced strain effects may also affect the variation of the magnetic moment [2, 13].

CHAPTER 7

Nanocrystalline FePd

Nanocrystalline FePd powder is synthesized via co-evaporation of metal wires: (Fe: Chempur, 99.99% pure, diameter: 1 mm; Pd: Chempur/Goodfellow, 99.95% pure, diameter: 1 mm) and inertgas condensation in two different alloy compositions: i) $Fe_{20}Pd_{80}$, ii) $Fe_{50}Pd_{50}$. The experimental procedures for the mounting of the cell and in-situ SQUID measurements follow the descriptions in the sections 3.1.2.1 and 3.3.1.

7.1. Electrochemical pre-characterization

Comparing the cyclovoltammograms for Pd, $Fe_{20}Pd_{80}$, and $Fe_{50}Pd_{50}$ in Fig. 7.1 indicates a shift of the oxygen desorption peak to lower desorption voltages in cathodic direction with increasing Fe-fraction. This holds both for $Fe_{20}Pd_{80}$ (desorption peak at -380 mV) and $Fe_{50}Pd_{50}$ where the desorption voltage decreases in anodic direction to -460 mV. $Fe_{50}Pd_{50}$ exhibits much higher currents in anodic directions from -100 mV to +400 mV (Fig 7.1). This indicates a more pronounced adsorption of oxygen to the surface of samples with a high Fe-fraction. As there is less desorption of oxygen in cathodic direction one can conclude that oxygen binds irreversibly to the surface of Fe-rich alloy samples.

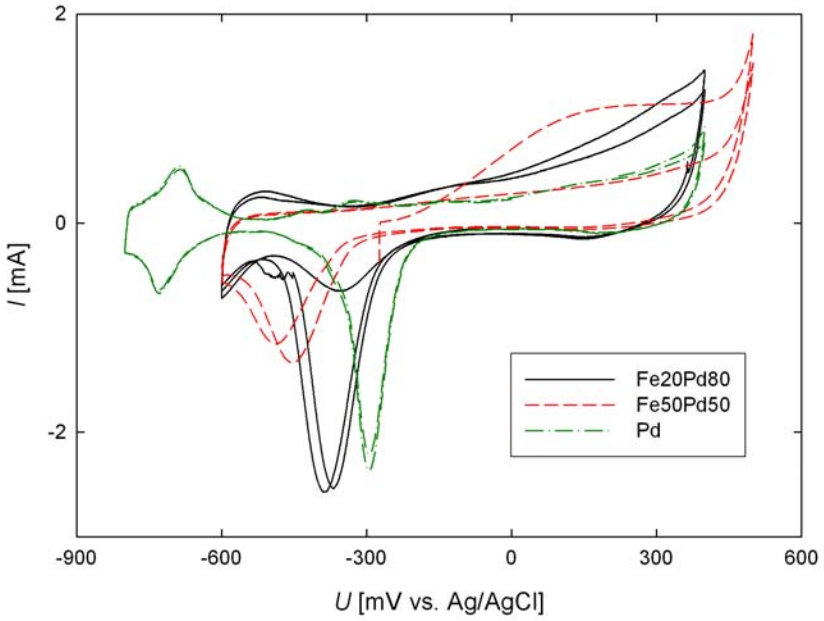

Figure 7.1.: Comparison of cyclovoltammograms measured on nanocrystalline Pd, $Fe_{20}Pd_{80}$ and $Fe_{50}Pd_{50}$ in 1-M KOH.

7.2. Charge-induced variation of magnetic moment of $Fe_{20}Pd_{80}$

Charging voltage in 2-electrode geometry

The precharacterization was performed by cyclovoltammetry in 3-electrode set-up, presented in Fig. 7.1 for $Fe_{20}Pd_{80}$. Charging in-situ in SQUID is performed in 2-electrode geometry . In Tab. 7.1 the adequate 2-electrode voltage between WE and CE consistent with 3-electrode geometry is listed.

The voltage $U_{WE-CE_{end}}$ between WE and CE refers to the end of the measurement. For constant values of U_{WE-RE} (between working electrode and reference electrode) one can notice significant differences between WE and CE upon consecutive cycling. A value U_{WE-RE} of 0 mV corresponds to $U_{WE-CE_{end}}$ of +311 mV at the beginning of the cycles and +745 mV at the end. Such a voltage shift might be due to surface modifications. In the present case this is related to electrooxidation and electroreduction of oxygen in the specific regimes [48, 50]. The pellet in use has a weight of 11.5 mg.

U_{WE-RE} **[mV]**	$U_{WE-CE_{max}}$ **[mV]**	$U_{WE-CE_{mid}}$ **[mV]**	$U_{WE-CE_{end}}$ **[mV]**
0	+179	+240	+311
-100	+202	+171	+162
+100	+393	+458	+533
-200	+218	+98	-11
+200	+441	+598	+757
-300	+204	+63	-404
+300	+430	+689	+992
0	+673	+592	+543
+100	+653	+678	+732
+200	+844	+867	+932
+300	+1044	+1076	+1153
+200	+1048	+1030	+1031
+100	+926	+905	+896
0	+790	+767	+745

Table 7.1.: 2-electrode charging voltages measured at three different times (start, middle and end) during chronoamperometry measurements vs. Ag/AgCl for $Fe_{20}Pd_{80}$

Magnetic measurements with in-situ SQUID charging - $Fe_{20}Pd_{80}$

The pellet used for the in-situ SQUID investigations has a weight of 22.81 mg. The in-situ SQUID measurements are started at 70 kOe and subsequently the applied magnetic field H is decreased down to 20 Oe. For each field setting in-situ charging experiments are performed. The charging sequence was started with one cycle at 0 mV, raised up to +1050 mV and down to +150 mV (Fig. 7.2). The maximum charging voltage was reduced to +900 mV after the measurement at a magnetic field of 70 kOe in order to prevent oxygen evolution at rather high voltages in SQUID which could cause damage of the electrochemical cell. The final state was set to +200 mV.

The variation of the magnetic moment upon cycling the voltage and charge is shown in Fig. 7.2. Positive charging decreases the magnetic moment while negative charging increases it. From the linear fit of Fig 7.3 a negative charge coefficient $\beta = \frac{d(m/m_{ref})}{dQ} =$ -0.11×10^{-3} g C^{-1} is deduced.

For magnetic fields at and below 200 Oe a sign inversion of the m-response on charging is detected (Fig. 7.4). Positive charging leads to an increase of m while negative charging decreases it. The charging coefficient β derived from Fig. 7.5 amounts to 9.51×10^{-5} g C^{-1}. At the beginning of the measuring sequence there is a steep increase of m which is not fully reversible upon reversing U. The data measured for the other magnetic fields are summarized in the appendix (section 13.3.2.2).

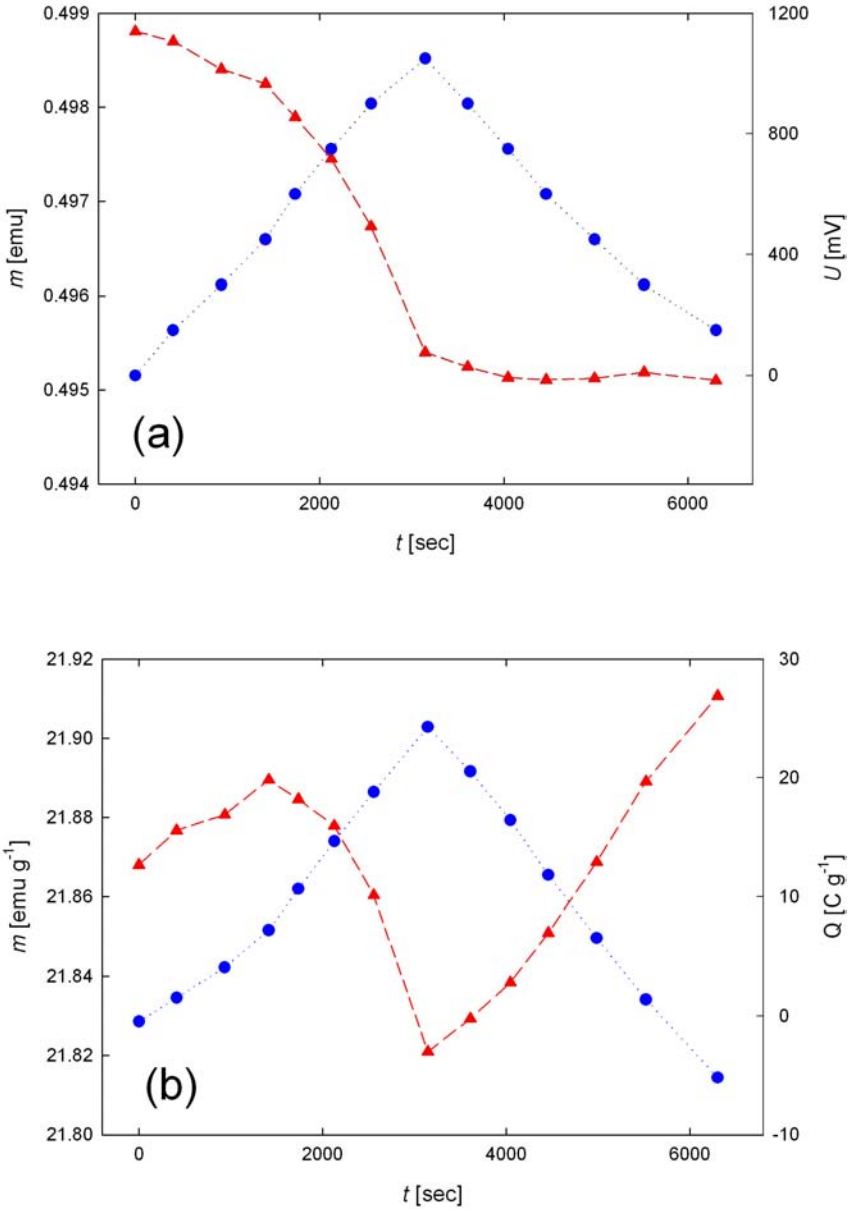

Figure 7.2.: Magnetic moment m (▲) of $Fe_{20}Pd_{80}$ measured at 70 kOe upon consecutive cycling: (a) charging voltage U (●), (b) imposed charge Q (●). t: time. m, Q in (b) drift-corrected.

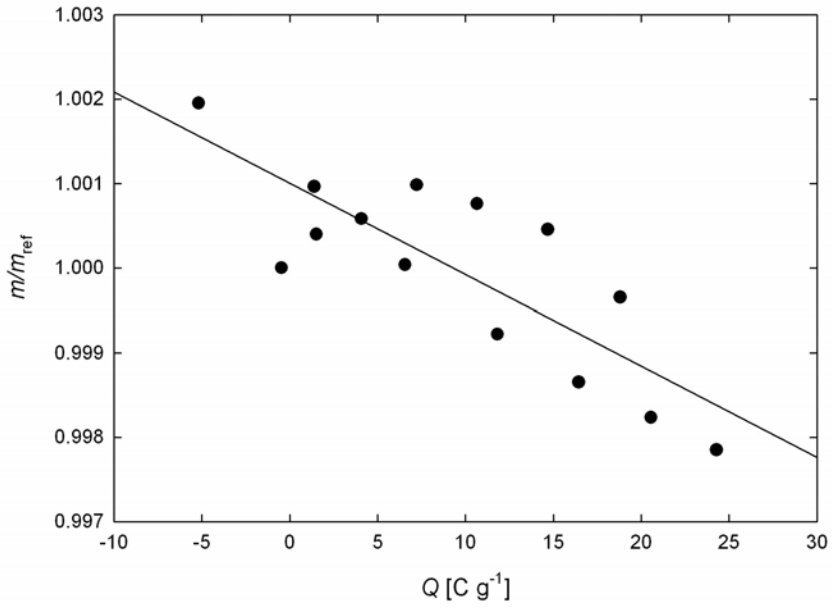

Figure 7.3.: Relative magnetic moment m/m_{ref} of $Fe_{20}Pd_{80}$ measured at 70 kOe in dependence of charge Q. m_{ref} refers to the first measured magnetic data point. m, Q drift-corrected.

The results of magnetic measurements on $Fe_{20}Pd_{80}$ in dependence of the magnetic field are shown in Fig. 7.6. The charge-induced variation Δm increases with H. Such a behaviour can be expected as an increase of m must be accompanied with an increase of Δm. An exception is the step between 20 Oe and 200 Oe where Δm slightly increases. Noteworthy is the slight decrease of m observed between 20 kOe and 70 kOe. One possible explanation can be given by an electrochemical 'cleaning' process where oxygen adsorbates on the sample are removed via electrochemical cycling since the measurements at 70 kOe were performed first, the subsequent measurements one day afterwards.

The charge-induced variation $\Delta m/m_{ref}$ is largest for 20 Oe with 0.91 %. From 200 Oe to 20 kOe $\Delta m/m_{ref}$ remains rather constant while at 70 kOe a slight increase is observed with $\Delta m/m_{ref} = 0.33$ %. The charge-coefficient β changes from positive to negative with increasing magnetic field.

Tab. 7.2 summarizes the magnetic measurements. H is listed in chronological order. m and Q show a linear drift superimposed to the charge-induced variation.

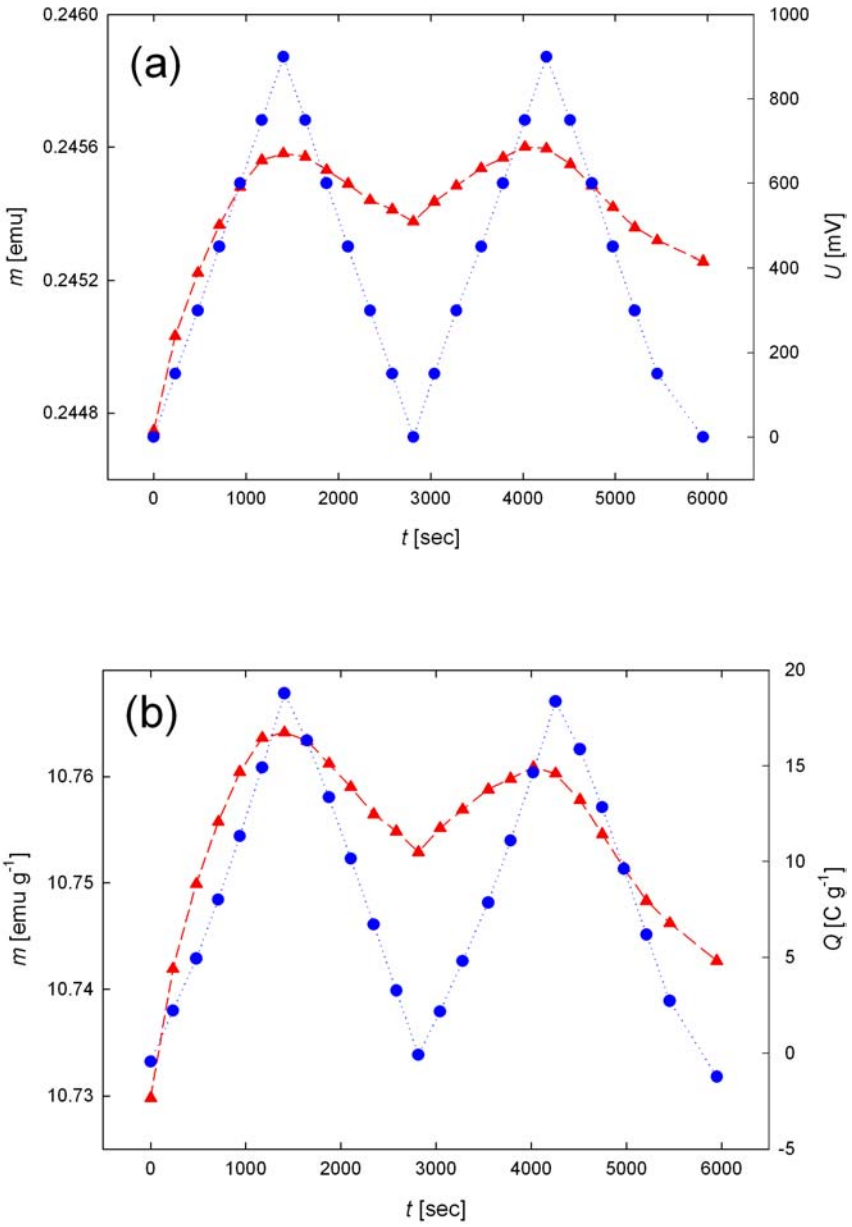

Figure 7.4.: Magnetic moment m (▲) of $Fe_{20}Pd_{80}$ measured at 200 Oe upon consecutive cycling (a) charging voltage U (●), (b) imposed charge Q (●). t: time. m, Q in (b) drift-corrected.

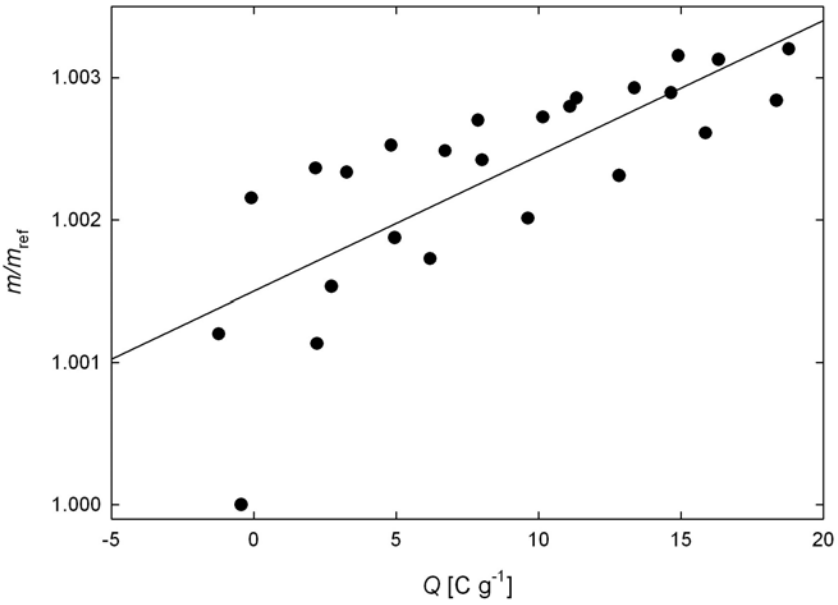

Figure 7.5.: Relative magnetic moment m/m_{ref} of $Fe_{20}Pd_{80}$ measured at 200 Oe in dependence of charge Q. m_{ref} refers to the first measured magnetic data point. m, Q drift-corrected.

H **[Oe]**	Δm $[\frac{emu}{g}]$	$\frac{\Delta m}{m_{ref}}$ [%]	$\frac{d(m/m_{ref})}{dQ}$ $[\frac{g}{C}]$	$\frac{dQ}{dt}$ $[\frac{C}{g\ sec}]$	$\frac{dm}{dt}$ $[\frac{emu}{g\ sec}]$	$r^2_{\frac{d(m/m_{ref})}{dQ}}$
70000	0.073	0.33	-1.09×10^{-4}	$+1.99\times\ 10^{-3}$	$-3.26\times\ 10^{-5}$	0.67
20000	0.023	0.09	-5.62×10^{-5}	-1.79×10^{-4}	-1.50×10^{-5}	0.55
2000	0.015	0.06	-3.83×10^{-5}	-3.72×10^{-4}	-1.16×10^{-5}	0.44
200	0.010	0.09	$+9.51\times10^{-5}$	$+1.85\times10^{-5}$	1.59×10^{-6}	0.59
20	0.020	0.91	$+2.84\times10^{-4}$	$+3.29\times10^{-4}$	3.69×10^{-6}	0.94

Table 7.2.: Charge-induced variation of magnetic moment; summary for $Fe_{20}Pd_{80}$. For definition of symbols see Tab. 5.1

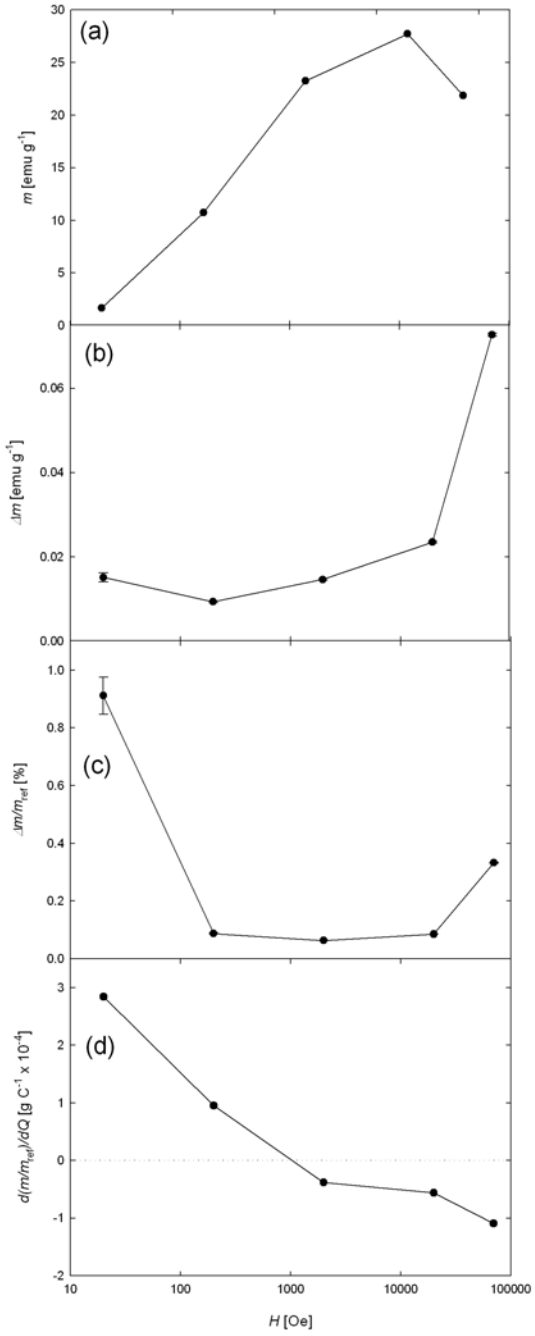

Figure 7.6.: Charge-induced variation of magnetic moment of $Fe_{20}Pd_{80}$ upon cycling between -750 mV and +1100 mV in dependence of magnetic field H: (a) magnetic moment m, (b) variation Δm (c) absolute value of relative variation $\Delta m/m_{ref}$ with m_{ref} denoting the first measured datapoint, (d) charge coefficient $\beta = \frac{d(m/m_{ref})}{dQ}$.

7.3. Charge-induced variation of magnetic moment of $Fe_{50}Pd_{50}$

The present chapter deals with the investigation of in-situ charged $Fe_{50}Pd_{50}$ synthesized by means of crystallite condensation under inertgas. A pellet with a weight of 11.45 mg is prepared according to the procedures described in the sections 3.1.2.1 and 3.3.1.

Determination of the 2-electrode charging regime

In Tab. 13.1 and Tab. 13.2 (see Appendix section 13.3.2.1) the voltage U_{WE-CE} of +1100 mV is assigned to a voltage U_{WE-RE} of ≈ 200-300 mV (3-electrode setup) where oxygen adsorption occurs. The desorption peak for oxygen is located at a voltage U_{WE-RE} of -450 mV which corresponds to a voltage U_{WE-CE} of -600 mV in two electrode geometry [48].

Magnetic measurements with in-situ SQUID charging - $Fe_{50}Pd_{50}$

In the case of $Fe_{50}Pd_{50}$ the charging sequences are started at a field of 20 Oe and subsequently raised up to 20 kOe. The first measuring sequence is alternating between a charging voltage of +1100 mV (oxygen adsorption) and -600 mV (oxygen desorption) as deduced from the pre-characterization. After having finished this for each single magnetic field, a more detailed measuring sequence was taken with chronoamperometric charging being performed from 0 mV to +1100 mV and back down to -600 mV in steps of $|\Delta U| =$ 300 mV. The variation of m upon stepwise consecutive charging is shown in Fig. 7.7 and Fig. 7.9 for 200 Oe and 20 kOe, respectively. The corresponding plot m/m_{ref} versus Q (200 Oe) is shown in Fig. 7.8. Results measured at further magnetic fields are summarized in the appendix.

For 200 Oe the magnetic moment increases upon positive charging and vice versa. From linear regression a charging coefficient $\beta = 1.41 \times 10^{-5}$ g C^{-1} is derived (Fig. 7.8). For 20 kOe the magnetic moment decreases with charging and vice versa. (Fig. 7.9). The linear regression fit yields a charge coefficient $\beta = \frac{d(m/m_{ref})}{dQ}$ of -5.26×10^{-5} g C^{-1}. As for $Fe_{20}Pd_{80}$ a sign inversion of β occurs.

Tab. 7.3 summarizes the results for $Fe_{50}Pd_{50}$ for alternating charging between +1100 mV and -600 mV. The drifts for m and Q are subtracted via linear regression fit when determining β.

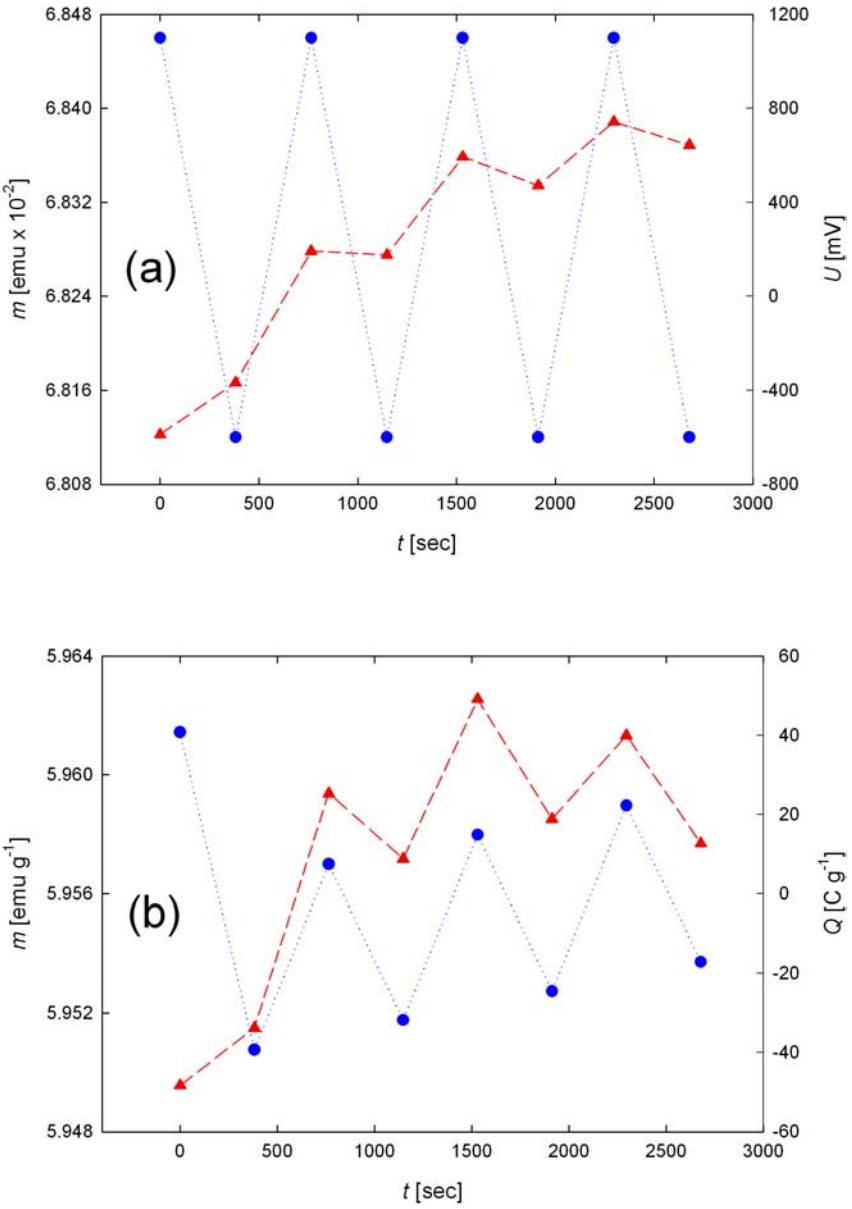

Figure 7.7.: Magnetic moment m (▲) of $Fe_{50}Pd_{50}$ measured at 200 Oe upon consecutive cycling: (a) charging voltage U (●), (b) imposed charge Q (●). t: time. m, Q in (b) drift-corrected.

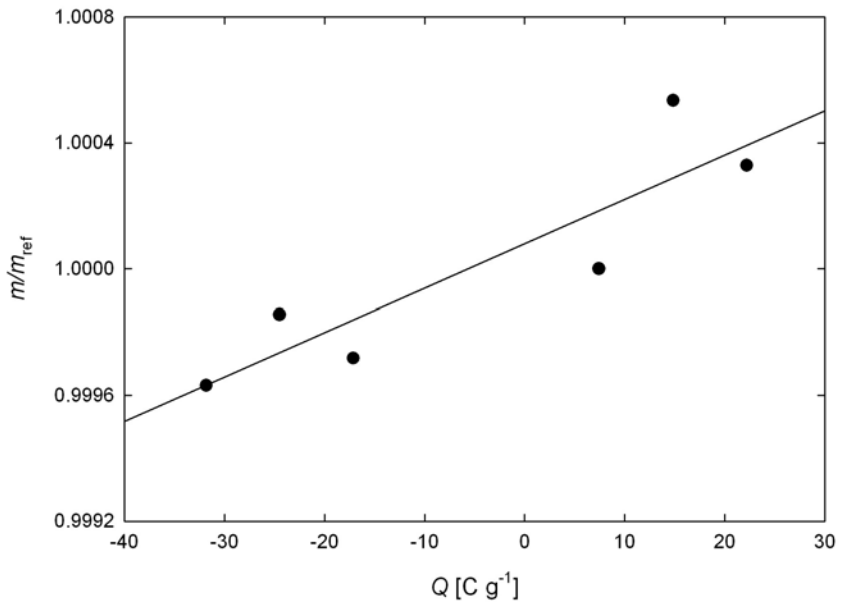

Figure 7.8.: Charge-dependence of the relative magnetic moment m/m_{ref} of $Fe_{50}Pd_{50}$ at 200 Oe. m_{ref} refers to the first measured m data point. The solid line shows the linear regression of the charging coefficient β. m, Q drift-corrected.

H **[Oe]**	Δm $[\frac{emu}{g}]$	$\frac{\Delta m}{m_{ref}}$ [%]	$\frac{d(m/m_{ref})}{dQ}$ $[\frac{g}{C}]$	$\frac{dQ}{dt}$ $[\frac{C}{g\ sec}]$	$\frac{dm}{dt}$ $[\frac{emu}{g\ sec}]$	$r^2_{\frac{d(m/m_{ref})}{dQ}}$
20	0.0041	1.83	1.17×10^{-4}	-8.06×10^{-3}	3.46×10^{-6}	0.95
200	0.0043	0.07	1.41×10^{-5}	1.39×10^{-2}	4.99×10^{-6}	0.80
2000	0.0230	0.12	-2.79×10^{-5}	-4.39×10^{-3}	-2.05×10^{-5}	0.99
20000	0.0554	0.22	-5.26×10^{-5}	-5.11×10^{-3}	-1.55×10^{-5}	0.99

Table 7.3.: Charge-induced variation of magnetic moment; summary for $Fe_{50}Pd_{50}$. For definition of symbols see Tab. 5.1

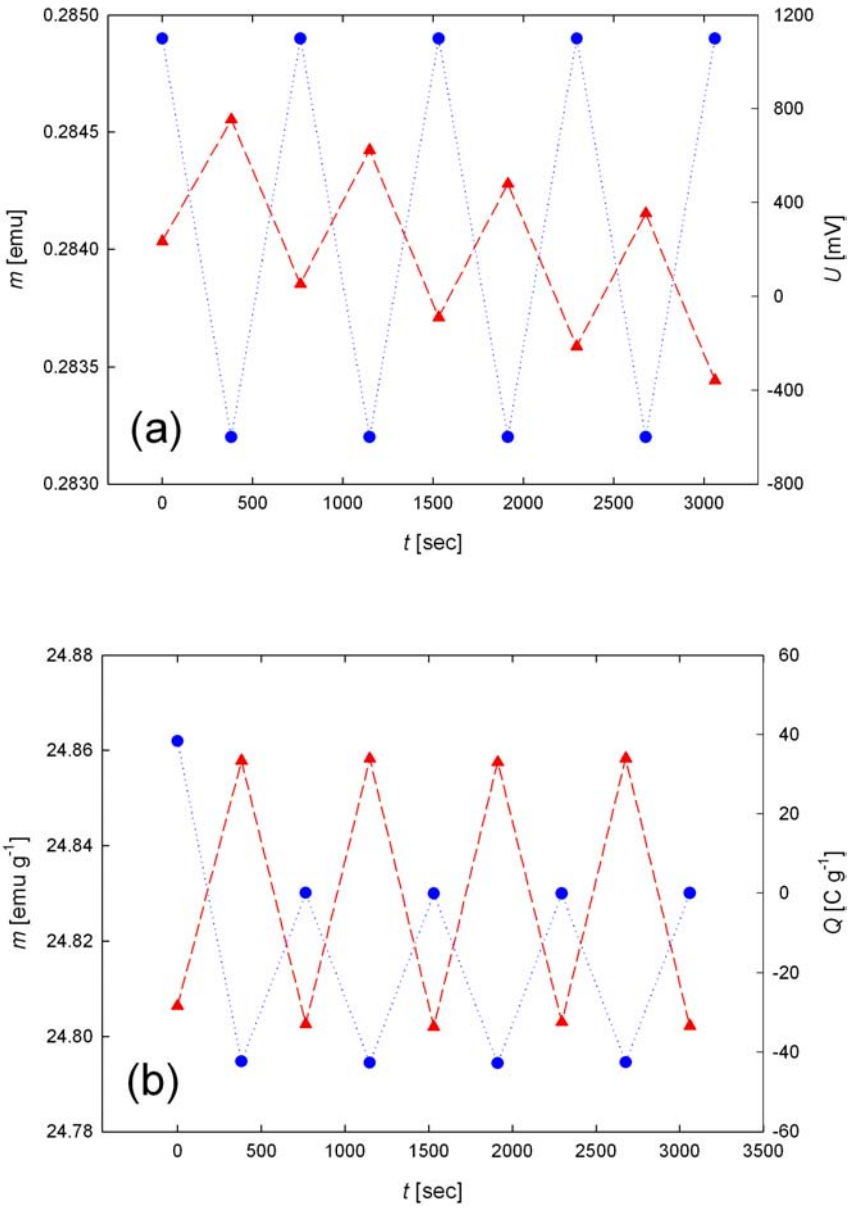

Figure 7.9.: Magnetic moment m (▲) of $Fe_{50}Pd_{50}$ measured at 20 kOe upon consecutive cycling (a) charging voltage U (●), (b) imposed charge Q (●). t: time. m, Q in (b) drift-corrected.

In the Fig. 7.10, 7.11 and 7.12, 7.13 the results for 200 Oe and 20 kOe are shown for the second measuring sequence with reduced voltage steps $|\Delta U| = 300$ mV. At 200 Oe m exhibits a kink upon reversing the sign of the charging voltage (Fig. 7.10 a)).

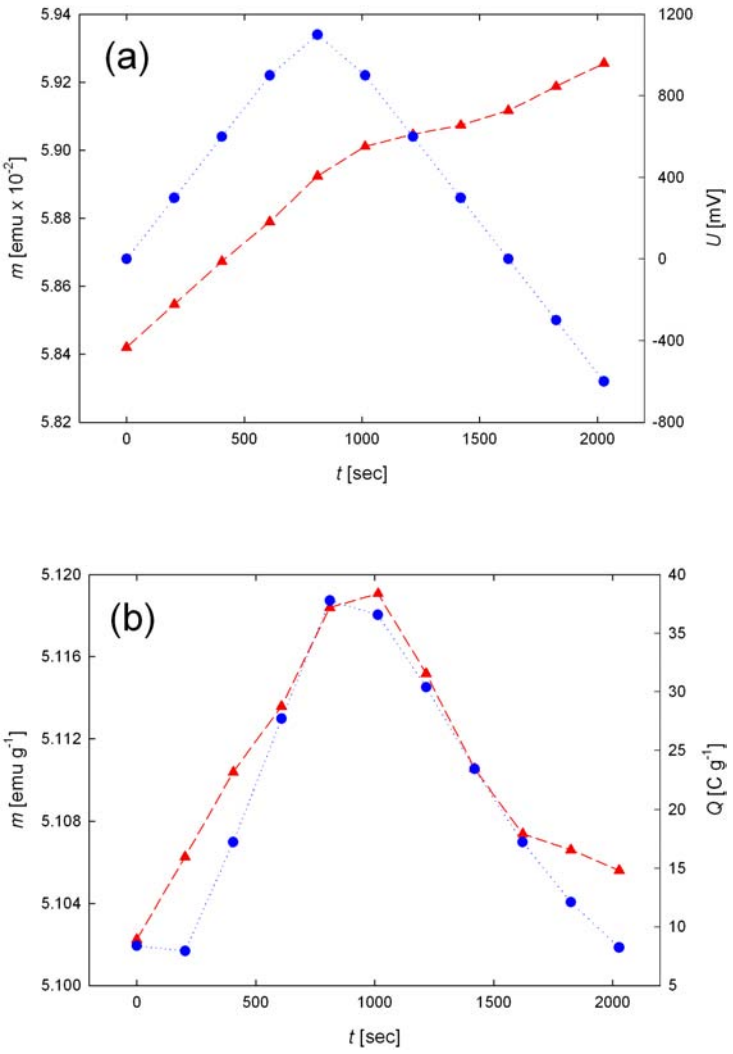

Figure 7.10.: Magnetic moment m (▲) of $Fe_{50}Pd_{50}$ measured at 200 Oe upon consecutive cycling in steps of $|\Delta U| = 300$ mV: (a) charging voltage U (●), (b) imposed charge Q (●). t: time. m, Q in (b) drift-corrected.

Electrochemical cycling at 20 kOe yields an opposite trend between magnetic moment and imposed charge (Fig. 7.12) compared to the measurements at lower fields. The charging coefficient β is negative (Fig. 7.13). The sign inversion of β with increasing field agrees with the results of the first measuring run as well as with results obtained for $Fe_{20}Pd_{80}$.

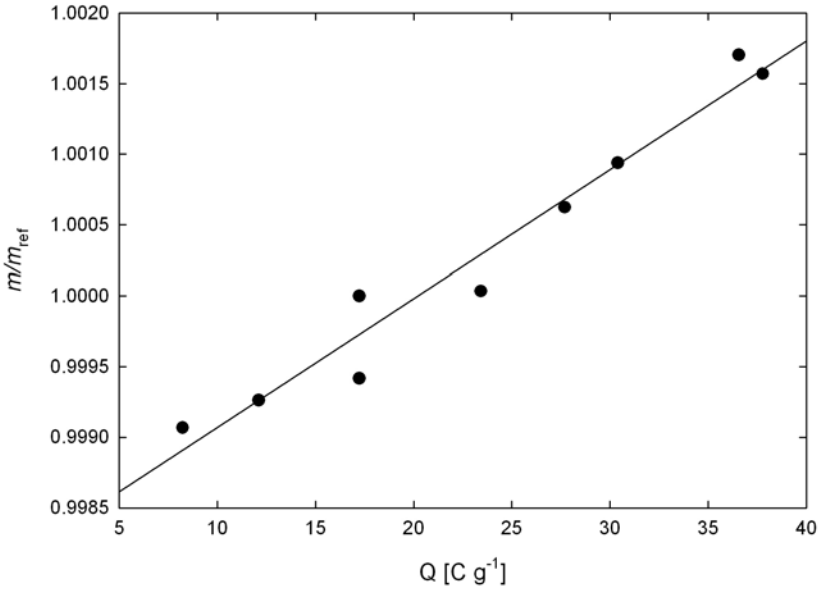

Figure 7.11.: Charge-dependence of the relative magnetic moment m/m_{ref} of $Fe_{50}Pd_{50}$ at 200 Oe in steps of $|\Delta U| = 300$ mV. m_{ref} refers to the first measured m data point. The solid line shows the linear regression of the charging coefficient β. m, Q in drift-corrected.

In Fig. 7.14 the magnetic field-dependence of $Fe_{50}Pd_{50}$ on charging is summarized. m shows a sigmoidal shape increase with H, as expected for magnetization in a magnetic field (Fig. 7.14 (a)). Δm indicates a slightly stronger increase in the first measuring cycle than in the second one Fig. 7.14 (b). At the maximum field of 20 kOe no significant differences for Δm are observed. The first measuring cycle shows a slight increase of $\Delta m/m_{ref}$ with H above 200 Oe while in the second cycle $\Delta m/m_{ref}$ remains rather constant (Fig. 7.14 (c)). At 20 Oe $\Delta m/m_{ref}$ is maximum. The charge coefficient $\beta = \frac{d(m/m_{ref})}{dQ}$ for all measured magnetic fields is illustrated in Fig. 7.14 (d). For fields at 200 Oe and below β is positive while for fields at 2 kOe and above β is negative.

Tab. 7.4 summarizes the data of the second, more detailed measuring sequence of $Fe_{50}Pd_{50}$. It is worth to mention here that the highest applied charge in the first measuring cycle is 42.65 C g^{-1} while for the second measuring cycle only 29.52 C g^{-1} could be imposed. Two reasons are considered to be responsible for this behaviour: The first could be coarsening due to ongoing adsorption and desorption processes as discussed for dealloyed Au [24]. The second possibility is a leakage of the electrochemical cell so that the evaporation of aqueous electrolyte due to the 25 mbar He-atmosphere in the SQUID leads to a loss of charging efficiency.

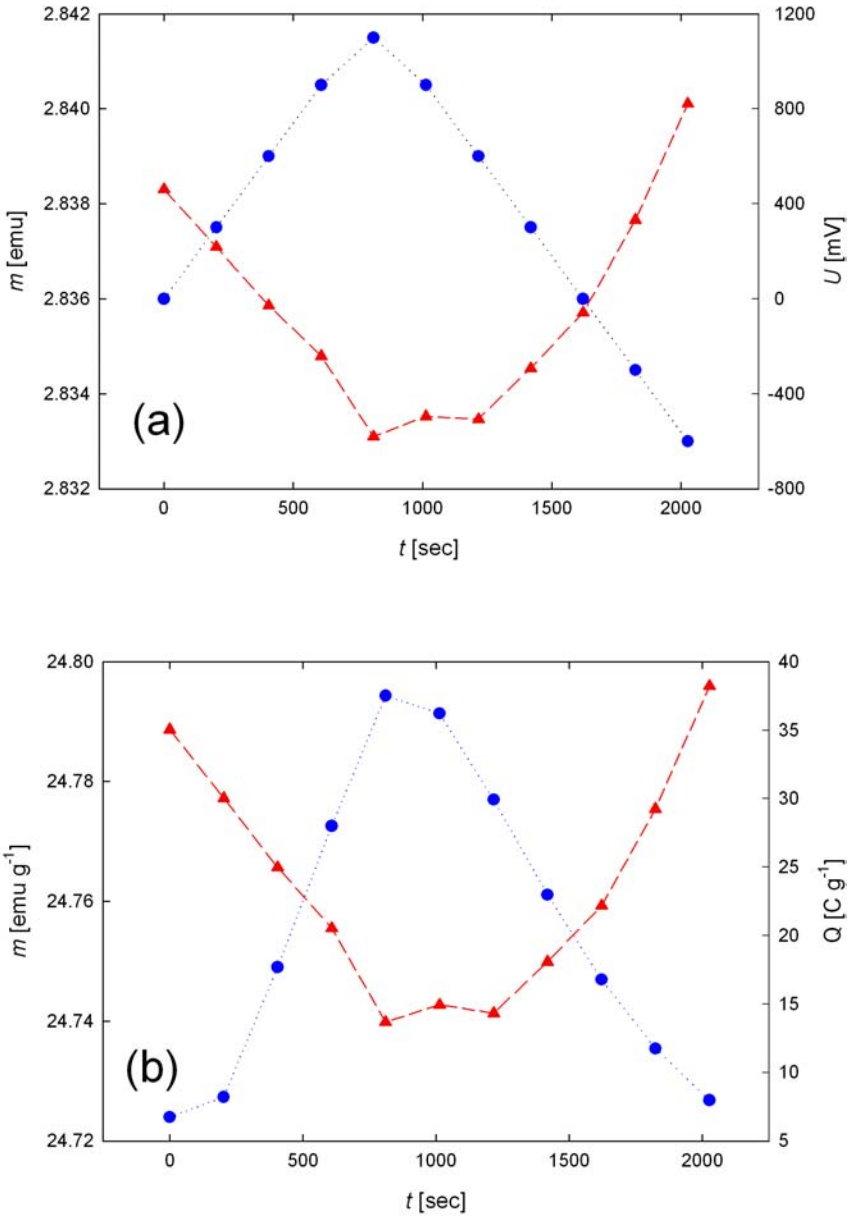

Figure 7.12.: Magnetic moment m (▲) of $Fe_{50}Pd_{50}$ measured at 20 kOe upon consecutive cycling in steps of $|\Delta U| = 300$ mV: (a) charging voltage U (●), (b) imposed charge Q (●). t: time. m, Q in (b) drift-corrected.

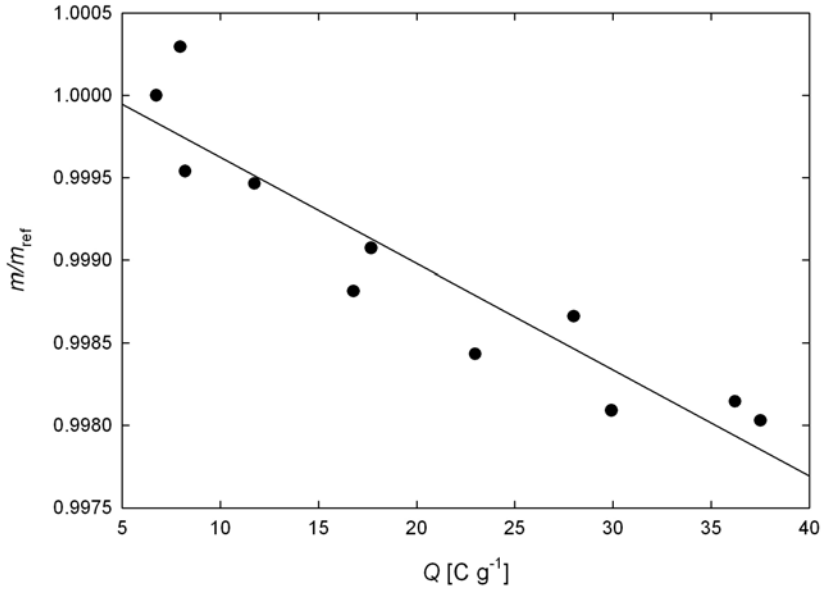

Figure 7.13.: Charge-dependence of the relative magnetic moment m/m_{ref} of $Fe_{50}Pd_{50}$ at 20 kOe in steps of $|\Delta U| = 300$ mV. m_{ref} refers to the first measured m data point. The solid line shows the linear regression of the charging coefficient β. m, Q drift-corrected.

H **[Oe]**	Δm $[\frac{emu}{g}]$	$\frac{\Delta m}{m_{ref}}$ **[%]**	$\frac{d(m/m_{ref})}{dQ}$ $[\frac{g}{C}]$	$\frac{dQ}{dt}$ $[\frac{C}{g\ sec}]$	$\frac{dm}{dt}$ $[\frac{emu}{g\ sec}]$	$r^2_{\frac{d(m/m_{ref})}{dQ}}$
20	-	-	-	-	-	-
200	0.0128	0.250	9.11×10^{-5}	-8.88×10^{-3}	3.43×10^{-5}	0.96
2000	0.0318	0.171	-5.30×10^{-5}	-8.65×10^{-3}	-1.69×10^{-5}	0.95
20000	0.0561	0.226	-6.44×10^{-5}	-8.88×10^{-3}	4.18×10^{-6}	0.87

Table 7.4.: Charge-induced variation of magnetic moment; summary for $Fe_{50}Pd_{50}$ with refined charging steps. For definition of symbols see Tab. 5.1

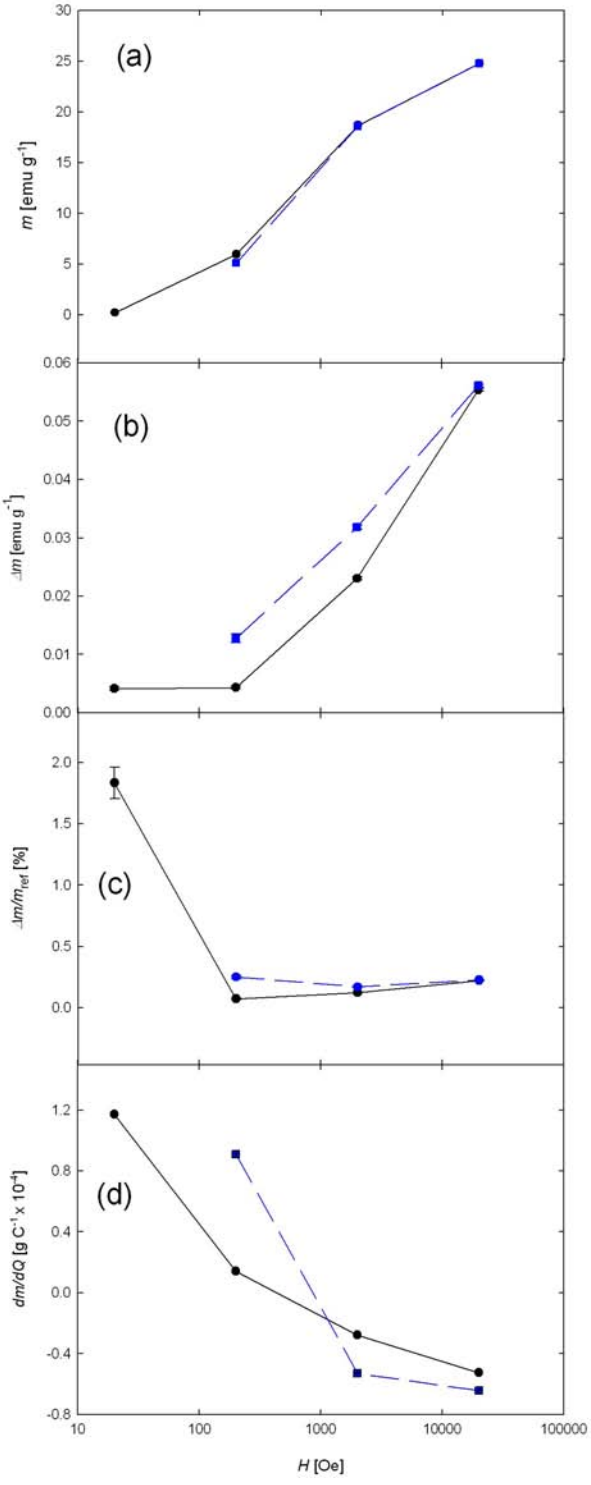

Figure 7.14.: Charge-induced variation of magnetic moment of $Fe_{50}Pd_{50}$ upon cycling between -750 mV and +1100 mV in dependence of magnetic field H; (a) magnetic moment m, (b) variation Δm, (c) absolute value of relative variation $\Delta m/m_{ref}$ with m_{ref} denoting the first measured data point, (d) charge coefficient $\beta = \frac{d(m/m_{ref})}{dQ}$. •, ■: data of first and second, more detailed measuring sequence, respectively. For the second measuring sequence no data point for 20 Oe could be obtained.

7.4. Discussion

Two alloy compositions of FePd are discussed in the present work: i) $Fe_{20}Pd_{80}$, and ii) $Fe_{50}Pd_{50}$. The FePd-alloys exhibit a charge-induced increase of the magnetic moment for 2 kOe and above and on the other hand a charge-induced decrease of the magnetic moment for 200 Oe and lower fields upon negative charging. The charging effect is reversible and reproducible for both FePd-compositions.

When looking at the measuring sequence it becomes clear that the sequential order of magnetic field application influences the results. For $Fe_{20}Pd_{80}$ the measuring sequence is started with 70 kOe. The sequence for $Fe_{50}Pd_{50}$ is started with 20 Oe and also provides the largest observed relative variation of magnetization for the FePd-alloys with 1.83 %. It seems that applying a high magnetic field at the beginning of the measuring sequence induces some sort of pinning so that the effect is smaller at low magnetic fields compared to a measuring sequence where one starts out with a low magnetic field.

Drings et al. [13] report a reversible tunability for the susceptibility of Pd ($\approx$1 %) where positive charging increases the susceptibility and negative charging decreases it. These findings correspond well with the findings for Pd in the present work (section 6.3). Also for FePd one can observe the same sign for the variation of m up to 200 Oe.

Ghosh et al. [14] discussed charge-induced variations of Pd-Co alloys in non-aqueous electrolytes. Positive charging induced a decrease of the magnetic moment while negative charging leads to an increase of m. These observations are assigned to a charge induced reversible strain in the Pd-Co alloy [14]. In the doctoral thesis of Ghosh [51] the variation of the magnetic moment with charge ($\frac{dm}{dQ}$) is explained with the pressure dependence of the magnetic moment $\frac{dm}{dP}$ taking into account the variation of the strain with charge ($\frac{d\epsilon}{dQ}$). Furthermore magnetostrictive effects are considered with a focus on the so-called magnetostriction coefficient $\frac{\partial\omega}{\partial H}$ with ω denoting the volumetric strain. With [51]

$$\frac{\partial\omega}{\partial H} = -\rho(\frac{\partial\sigma_s}{\partial P}) \tag{7.1}$$

the magnetostriction coefficient is related to the variation of the specific magnetization per mass (σ_s) with pressure P (ρ denotes the bulk density). The observed effects cannot be assigned clearly to one of the two models presented above [51]. Lemier et al. [52] investigated the charge-induced variation of Pd-Ni alloys in non-aqueous electrolytes. The magnetic

moment of $Pd_{67}Ni_{33}$ decreases upon positive charging and vice versa. For $Pd_{60}Ni_{40}$ the observed effect is reversed [52]. The charge-induced variation of the magnetic moment of Pd-Ni alloys is discussed in terms of magnetostriction (see also Eq. 7.1). The variation of the alloy composition in Pd-Ni alloys leads to a variation of the magnetocrystalline anisotropy which also influences the response on an imposed charge [52].

In the present work the FePd-alloy composition cannot be given as a reason, as the sign inversion is observed for both investigated FePd-alloys. For both Co and Pd studied in this work (see chapters 5 and 6 respectively) no field-dependence of charging was observable. For Co (negative β) the charge-induced variation of m was ascribed to electrochemical surface modifications while for Pd (positive β) the band-filling model was considered. Is is well-known that the magnetocrystalline anisotropy strongly influences the magnetic properties of a material [30, 53]. As charging may induce a huge pressure on a nanostructured material [2, 10, 14] it is evident to assume an influence of charging on the magnetocrystalline anisotropy of FePd-alloys. However, for FePd the charge-coefficient β is not alloy-dependent but field-dependent. Therefore, the complex behaviour of sign inversion with increasing field may indicate that the variation of m is not exclusively of electronic origin, but that also charge-induced lattice strain by means of magneto-elastic coupling may play a role. The relative contribution of the latter effect may increase with the increasing field. In order to further clarify this item, measurements on Fe-Ni with low magnetostriction are desireable.

As β is positive for fields smaller than 200 Oe and negative for fields higher than 2 kOe, two competing H-dependent effects might play a role. However, the magnetic field dependence of the charge-induced effect still demands further clarification.

CHAPTER 8

Maghemite/platinum nanocomposites

In this chapter the charge-induced variation of the magnetic moment of maghemite (γ-Fe_2O_3) is discussed. Due to the insulating properties of γ-Fe_2O_3, charging could be accomplished by means of a conductive interpenetrating network. In the present case this is provided by platinum. Measurements are presented for γ-Fe_2O_3, Pt and the composite of γ-Fe_2O_3 and Pt. γ-Fe_2O_3 was synthesized by Dorothée Vinga Szabo, Karlsruhe [19]. Fig. 8.1 shows γ-Fe_2O_3 investigated by TEM.

The measurements and evaluations presented in this chapter were performed by Stefan Topolovec in the course of his master thesis under co-supervision of the present author [32]. The main part of Stefan Topolovec was the structural characterization and data analysis and the main part of my work was on the magnetic measurements.

Findings on the γ-Fe_2O_3/Pt-composite (1:3 weight-%) where published in Physica Status Solidi: Rapid Research Letters [54].

8.1. Magnetic pre-characterization

Before starting the electrochemical pre-characterization and the in-situ charging experiments, γ-Fe_2O_3 and platinum are characterized by SQUID. For the characterization of γ-Fe_2O_3 2.5 mg are filled into a measurement capsule and centered in the SQUID. Fig. 8.2 shows two hysteresis loops: one at 4 K and one at 300 K. The coercitivity H_c significantly decreases at room temperature compared to 4 K indicating superparamagnetic behaviour. At 4 K H_c is found to be 550 Oe, at 300 K H_c is determined with 11.3 Oe. The mag-

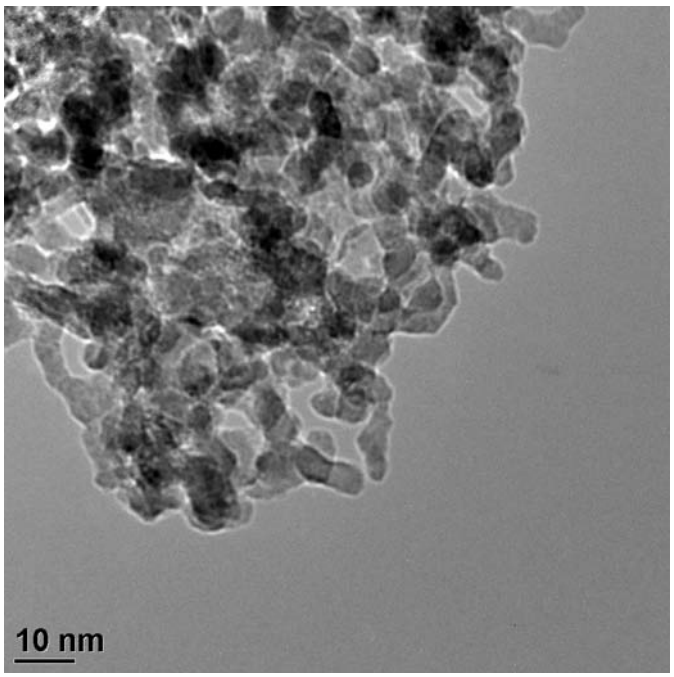

Figure 8.1.: TEM picture of γ-Fe_2O_3 (D.V. Szabo, Karlsruhe Institute of Technology).

netic moment m at 50 kOe gives a good estimation for the saturation magnetization M_{sat}. At 4 K $M_{sat,4K}$ amounts to 51 emu g^{-1} while at 300 K $M_{sat,300K}$ is found to be 43 emu g^{-1}. These values are significantly smaller compared to bulk-structured maghemite with 80 emu g^{-1} [32]. A decrease of the saturation magnetization for nanoparticles is well known, also for maghemite [55]. An explanation is given by the so called 'spin-canting' where the nanostructure of the particles prevents the spins from complete alignment at high fields [55–57].

Fig. 8.3 depicts a zero field cooling/field cooling characterization curve for γ-Fe_2O_3. For the field cooling part a magnetic field is set at 4.2 K. Then the temperature is raised up to 300 K where the magnetic field is switched off (the 'field cooling curve'). With no field applied the temperature is set to 4.2 K. Now the field is turned on again and the temperature is raised up to 300 K for obtaining the zero field cooling curve [58]. The ZFC/FC curve in Fig. 8.3 is characteristic for superparamagnetic behaviour [58]. One can derive a blocking temperature $T_B = 75$ K. For temperatures above T_B a slight splitting of the ZFC- and FC-curves can be observed. This indicates some sort of hysteresis effect superimposed to the superparamagnetism which may arise from dipolar coupling of the nanoparticles [59]. In summary it can be said that the present γ-Fe_2O_3 exhibits superparamagnetic behaviour but due to some sort of coupling effects this is slightly distorted and hysteresis is detected as a result of that.

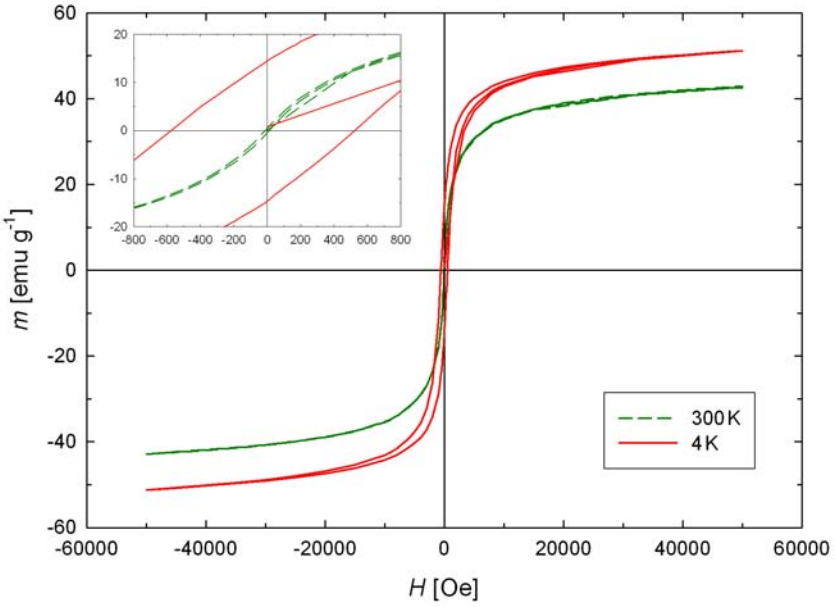

Figure 8.2.: Hysteresis loop of maghemite powder at 4 K and 300 K. The inset shows an enlarged picture for a better visualization of H_c [32].

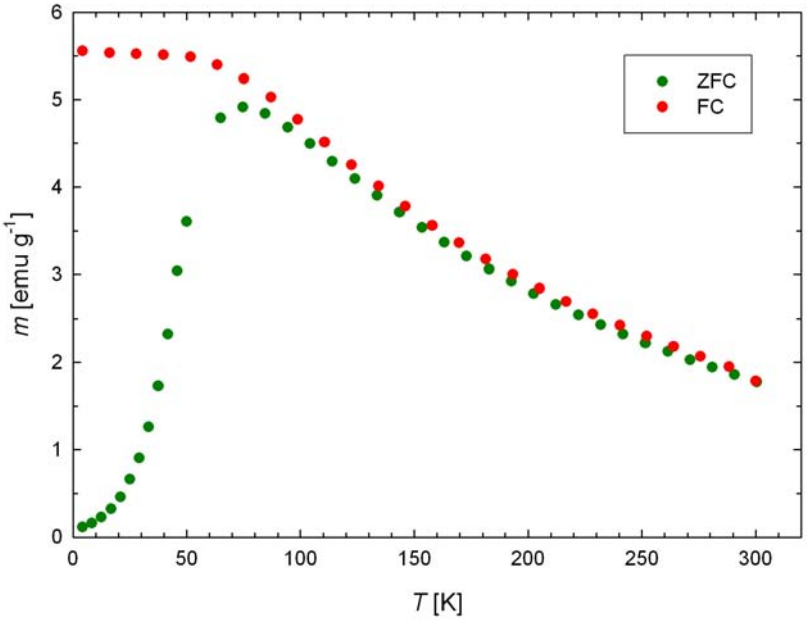

Figure 8.3.: ZFC/FC-curve of γ-Fe_2O_3 recorded in SQUID at a magnetic field of 50 Oe [32].

8.2. Electrochemical pre-characterization

In order to charge the insulating γ-Fe_2O_3 nanoparticles, a nanocomposite of the oxide nanoparticles and of an interconnected network of Pt nanoparticles was formed. For this purpose the γ-Fe_2O_3 nanoparticles were ultrasonically intermixed with commercial Pt nanoparticles (Chempur, particle diameter 6-10 nm) in a weight ratio of 1:3 and subsequently slightly compacted into a porous specimen with cylindrical shape (diameter 3 mm). For charging the porous specimen was immersed in an aqueous electrolyte of 1M KOH [54].

Electrochemical characterization of the porous γ-Fe_2O_3/Pt nanocomposite was performed in a standard electrochemical cell by means of a potentiostat (Autolab PGSTAT128N). The porous nanocomposite specimen contacted with a Au wire (purity 99.9 %, Chempur) served as working electrode, commercially available carbon clothing as counter electrode, and Ag/AgCl in saturated KCl as reference electrode (Eco Chemie) [54]. The cyclovoltammogram (CV) in the charging regime between -800 mV and +500 mV vs. Ag/AgCl is shown in Fig. 8.4 in comparison to that of a Pt sample made from the same Pt nanoparticles. The Pt sample exhibits the well-known characteristic regimes of chemisorption of oxygen species upon anodic cycling (charging voltage U > -100 mV) and subsequent desorption of oxygen species upon cathodic cycling (U < -300 mV) [35]. In the CV of the γ-Fe_2O_3/Pt nanocomposite additional shoulders at -500 mV in cathodic direction and -300 mV in anodic direction indicate electrochemical surface reactions of the γ-Fe_2O_3 which is part of the discussion of the results [54].

For in-situ charging in SQUID the 2-electrode geometry requires the determination of the charging voltage U between WE and CE. This is done by concurrent determination of the voltage between WE and CE when performing cyclovoltammetry in 3-electrode geomtetry vs Ag/AgCl as RE. Tab. 8.1 presents the respective voltage values.

Sample	**Charging regime**	U_{WE-CE} **[mV]**	U_{WE-RE} **[mV]**
Pt - pure	pseudocapacitive	850, 1250	-100, 200
Pt - pure	chemisorption	-450, 1250	-300, 200
γ-Fe_2O_3/Pt-composite 1:3	pseudocapacitive	850, 1250	0, 400
γ-Fe_2O_3/Pt-composite 1:3	chemisorption	-850, 850	(-550), 0

Table 8.1.: Determination of the 2-electrode voltage U_{AE-CE} between working electrode and counter electrode in comparison with the respective 3-electrode voltage U_{AE-RE} vs. Ag/AgCl [32].

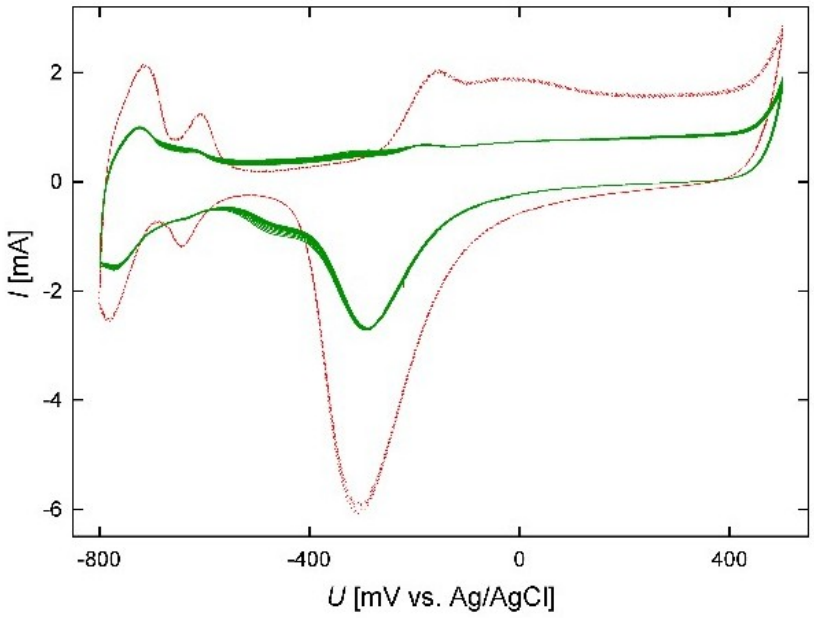

Figure 8.4.: Cyclovoltammogram: Charging current I versus charging voltage U during cycling at 0.5 mV/s of γ-Fe_2O_3/Pt nanocomposite (green) and of nanocrystalline Pt (red, dotted). U measured with respect to Ag/AgCl reference electrode [32, 54].

8.3. Charge-induced variation of magnetic moment

In this section the measuring results for the variation of the magnetic moment m in a γ-Fe_2O_3/Pt-composite with a 1:3 weight percent composition are presented. As outlined in the previous section two regimes for charging are chosen: i) pseudocapacitive charging regime (+850,+1250 mV), ii) chemisorption charging regime (-850,+850 mV).

8.3.1. Pseudocapacitive charging

The pseudocapacitive charging regime is scanned in voltage steps ΔU of 100 mV. The charging time during the in-situ SQUID measurements for chronoamperometry is 180 sec. The SQUID-measurements upon electrochemical cycling were performed at various magnetic fields ranging from 50 Oe to 50 kOe. Fig. 8.5 represents the measurements at 5 kOe. Positive charging leads to a decrease of m while negative charging increases it. The supplemental measurements at other H-fields can be found in the master thesis of Stefan Topolovec.

The charge coefficient $\beta = \frac{d(m/m_{ref})}{dQ}$ (obtained from a linear fit in Fig. 8.6) is negative for all field settings.

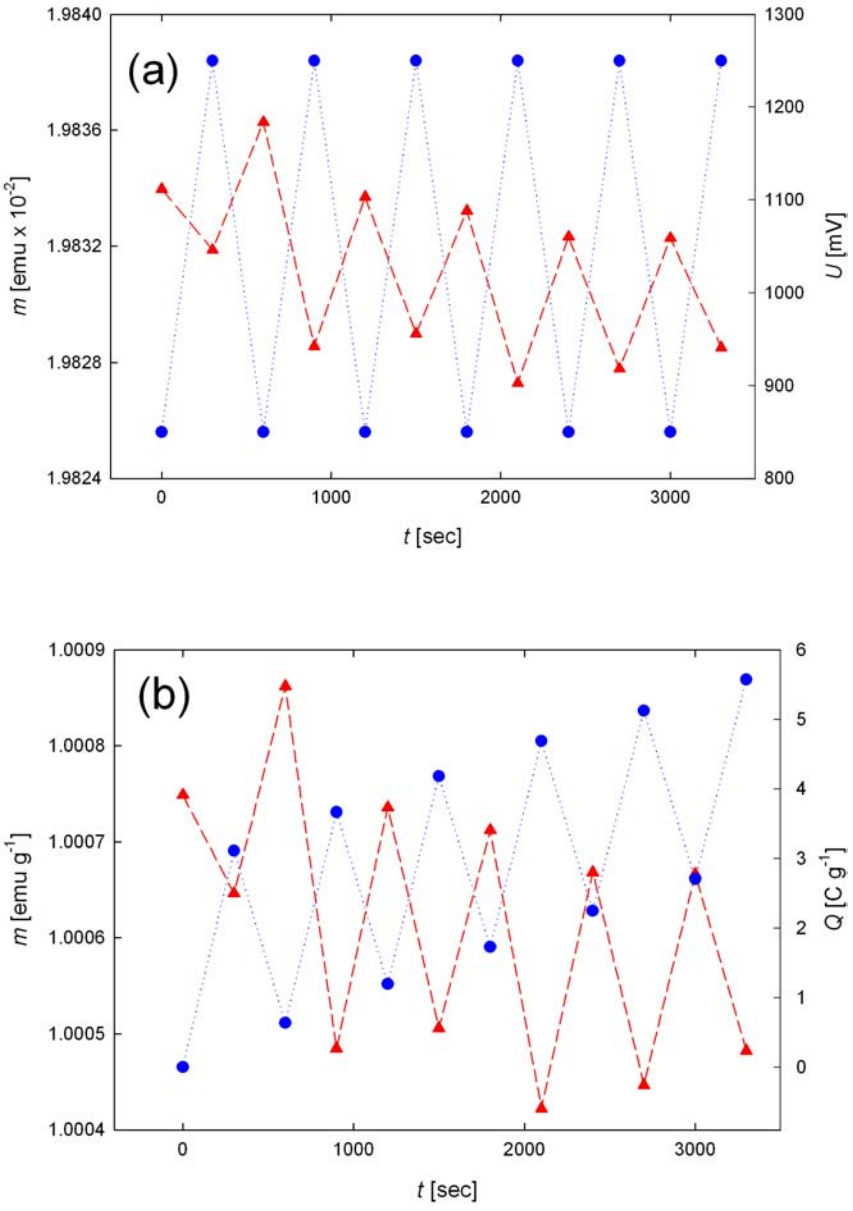

Figure 8.5.: Magnetic moment m (▲) of a γ-Fe_2O_3/Pt-composite measured at 5 kOe upon consecutive cycling in the pseudocapacitive regime (+850 mV/+1250 mV: (a) charging voltage U (●), (b) imposed charge Q (●). t: time [32].

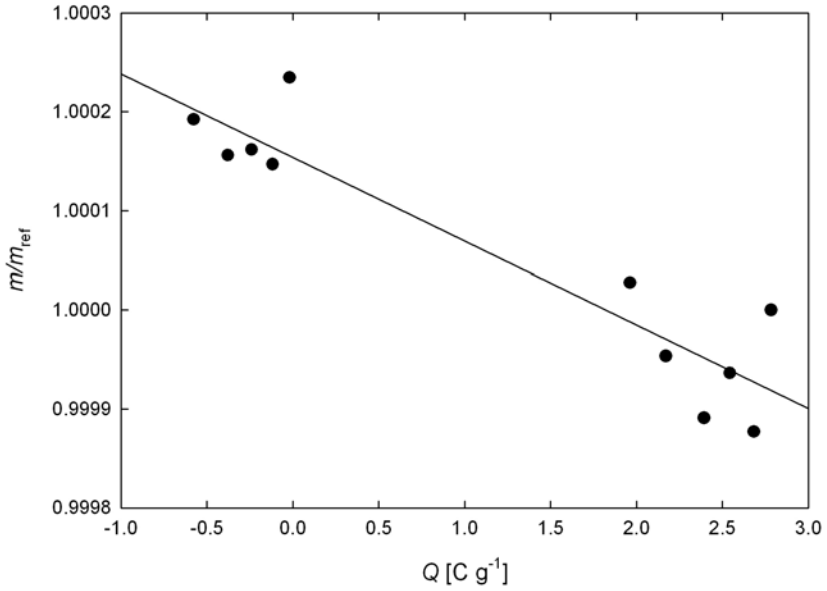

Figure 8.6.: Relative magnetic moment m/m_{ref} of γ-Fe_2O_3/Pt-composite in dependence of Q measured at 5 kOe in the pseudocapacitive charging regime. m, Q drift-corrected.

Fig. 8.7 shows that the variation of the magnetic moment Δm is increasing with the magnetic field.

However, the relative charge-induced variation of the magnetic moment $\Delta m/m_0$ decreases with H as depicted in Fig. 8.8. m_0 corresponds to the average value of all magnetic moments in the measurement cycle. For 50 Oe a maximum variation of 0.33 % occurs. The maximum variation of $\Delta m/m_0$ at the lowest fields is also reflected by the charge-coefficient β as depicted in Fig. 8.9.

Tab. 8.2 summarizes the results for the γ-Fe_2O_3/Pt-composite in the pseudocapacitive charging regime.

H **[Oe]**	Δm $[\frac{emu}{g}]$	$\frac{\Delta m}{m_0}$ [%]	$\frac{d(m/m_{ref})}{dQ}$ $[\frac{g}{C}]$	$\frac{dQ}{dt}$ $[\frac{C}{g\ sec}]$	$\frac{dm}{dt}$ $[\frac{emu}{g\ sec}]$	$r^2_{\frac{d(m/m_{ref})}{dQ}}$
50	3.73×10^{-5}	0.33	-6.59×10^{-4}	1.61×10^{-3}	no drift	0.74
500	7.38×10^{-5}	0.05	-1.85×10^{-4}	1.15×10^{-3}	-5.95×10^{-8}	0.95
5000	24.42×10^{-5}	0.02	-0.84×10^{-4}	1.09×10^{-3}	-6.38×10^{-8}	0.87

Table 8.2.: Charge-induced variation of magnetic moment; summary for a γ-Fe_2O_3/Pt-composite (composition: 1:3 weight-%) in the pseudocapacitve regime [32]. For definition of symbols see Tab. 5.1.

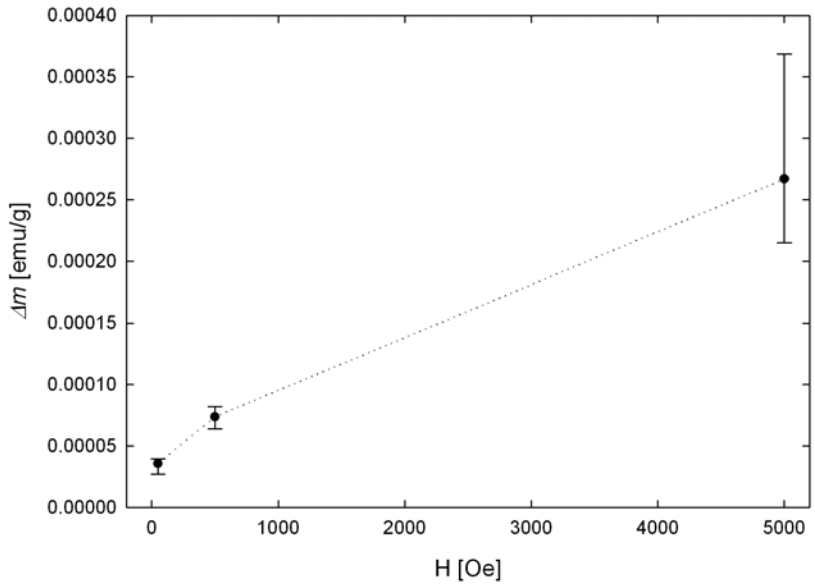

Figure 8.7.: Charge-induced variation of the magnetic moment Δm upon cycling between +850 mV and +1250 mV in dependence of the magnetic field H [32].

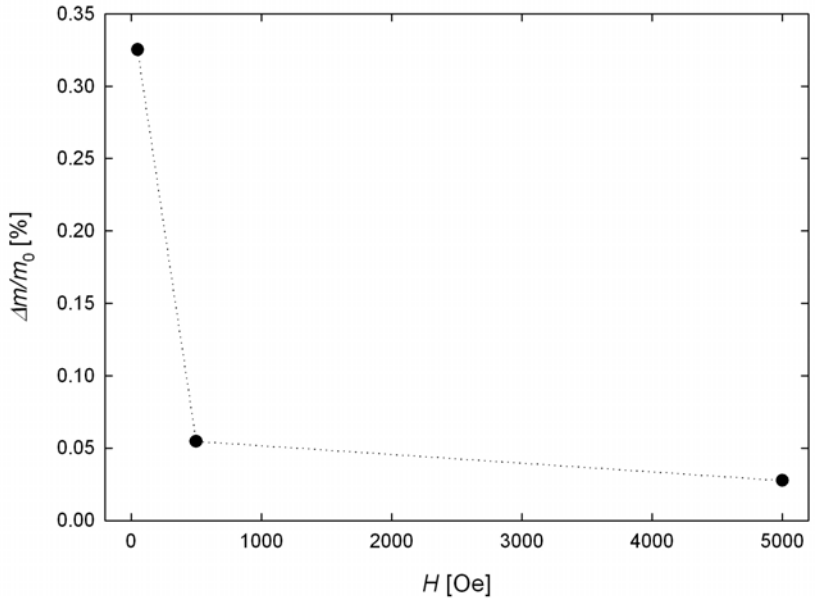

Figure 8.8.: Variation of the relative magnetic moment $\Delta m/m_0$ induced by charging in dependence of the magnetic field H. m_0 refers to the average value of all magnetic moments in the measurement cycle [32].

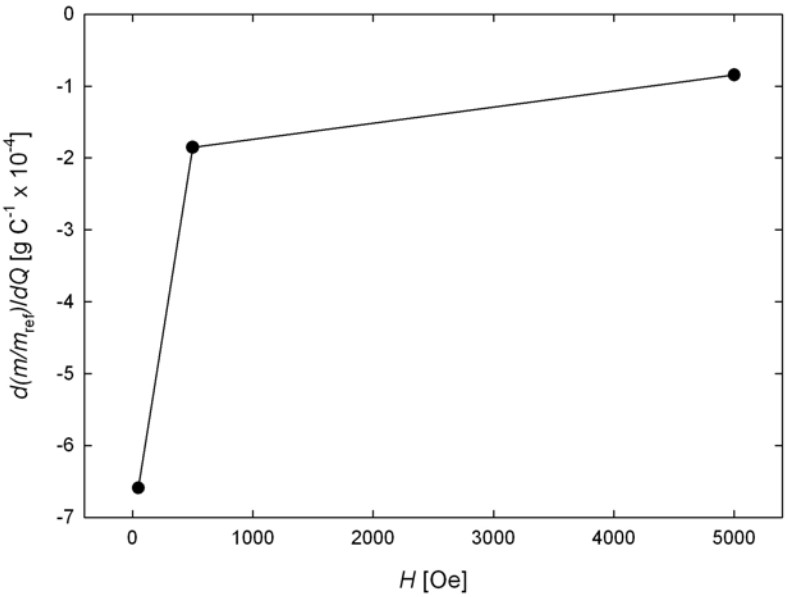

Figure 8.9.: $\frac{d(m/m_{ref})}{dQ}$ of γ-Fe_2O_3/Pt-composite in the pseudocapacitive charging regime in dependence of the magnetic field. m_{ref} refers to the first measured data point.

8.3.2. Charging in chemisorption regime

By subsequent cycling between +850 mV and -850 mV adsorption and desorption processes on the γ-Fe_2O_3/Pt-composite surface occur. The charging time for the electrochemical cell in the SQUID is 300 sec. The measurements are performed for magnetic field settings of 5 Oe, 50 Oe, 500 Oe, 5 kOe and 50 kOe.

As shown in Fig. 8.10, the magnetic moment can be tuned reversibly upon charging. The supplemental measurements for the other H-settings can be found in the master thesis of Stefan Topolovec [32].

With an increase of the magnetic field H also the variation of the magnetic moment Δm increases as shown in Fig. 8.11. In Fig. 8.12 a slight decrease with increasing H and a reincrease at the maximum field can be observed. $\Delta m/m_0$ in the chemisorption regime is significantly larger compared to the pseudocapacitive regime. The maximum $\Delta m/m_0$ in the chemisorption regime is more than 30 times higher than in the pseudocapacitive regime and attains a value of 10.4 %.

Reproducability was ensured by a second measurement on a separate γ-Fe_2O_3/Pt-composite with the same composition at a magnetic field of 50 kOe. The charge coefficient β for the second measurement was determined with -1.3×10^{-9} g C^{-1}, corresponding to $\Delta m/m_{ref}$

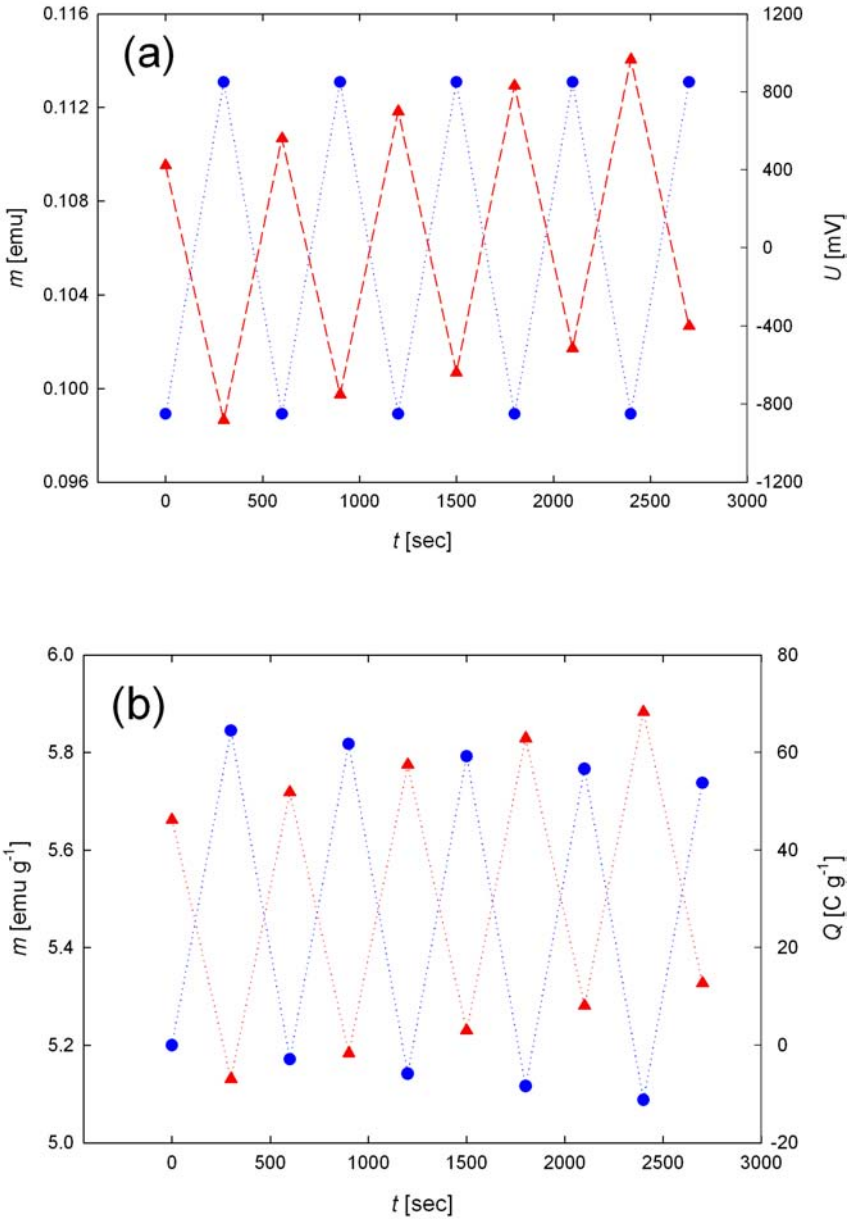

Figure 8.10.: Magnetic moment m (▲) of a γ-Fe_2O_3/Pt-composite measured at 5 kOe upon consecutive cycling in the regime of adsorption/desorption (a) charging voltage U (●), (b) imposed charge Q (●). t: time [32].

= 4.3 % and an applied charge Q of 32 C g^{-1}.

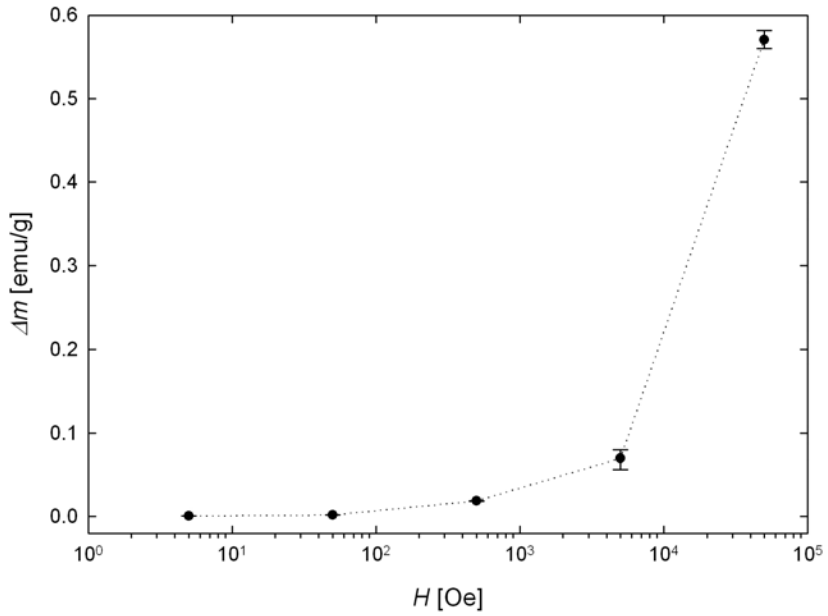

Figure 8.11.: Variation of the magnetic moment Δm with magnetic field H in the chemisorption regime. The error bars consist of the maximal and minimal determined value for the magnetic moment [32].

The variation of $\Delta m/m_0$ with H is also reflected in the field dependence of the charging coefficient β (Fig. 8.13).

Tab. 8.3 summarizes the characteristic values discussed above.

H **[Oe]**	Δm $[\frac{emu}{g}]$	$\frac{\Delta m}{m_0}$ [%]	$\frac{d(m/m_{ref})}{dQ}$ $[\frac{g}{C}]$	$\frac{dQ}{dt}$ $[\frac{C}{g\ sec}]$	$\frac{dm}{dt}$ $[\frac{emu}{g\ sec}]$	$r^2_{\frac{d(m/m_{ref})}{dQ}}$
5	6.09×10^{-4}	10.20	-1.75×10^{-3}	-4.48×10^{-3}	1.43×10^{-7}	0.98
50	1.69×10^{-3}	7.88	-1.35×10^{-3}	1.30×10^{-2}	6.42×10^{-7}	0.93
500	1.86×10^{-2}	8.05	-1.18×10^{-3}	-4.72×10^{-3}	3.26×10^{-6}	0.95
5000	6.97×10^{-2}	6.24	-1.10×10^{-3}	-3.13×10^{-3}	2.54×10^{-5}	0.97
50000	5.71×10^{-1}	10.40	-1.68×10^{-3}	-4.48×10^{-3}	2.94×10^{-5}	0.98

Table 8.3.: Charge-induced variation of magnetic moment; summary for a γ-Fe_2O_3/Pt-composite (composition 1:3 weight-%) in the adsorption/desorption regime. For definition of symbols see Tab. 5.1

8.4. Discussion

For the discussion of the present results, first of all it has to be pointed out that the charge-induced variation of the magnetization of the γ-Fe_2O_3/Pt-composite of 10 % is

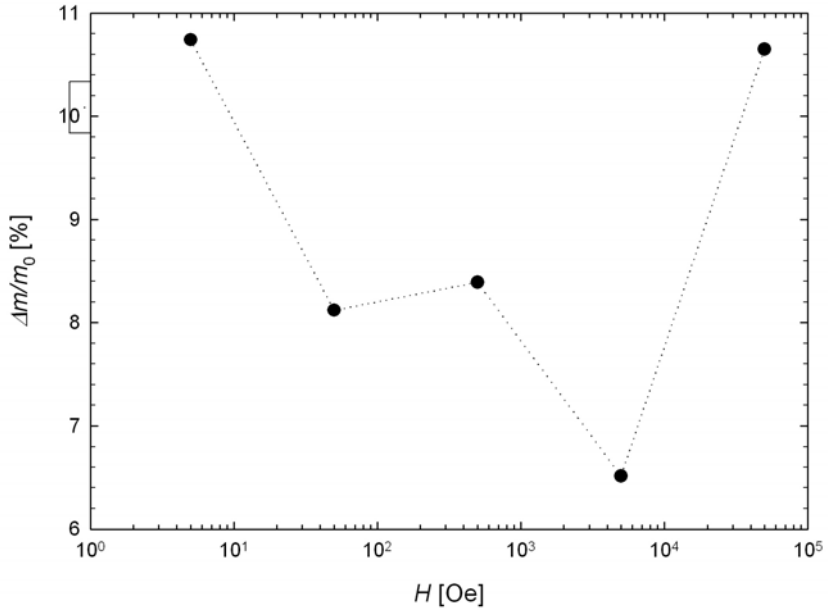

Figure 8.12.: Relative variation $\Delta m/m_0$ of the magnetic moment with magnetic field H in the chemisorption regime. m_0 refers to the average measured [32].

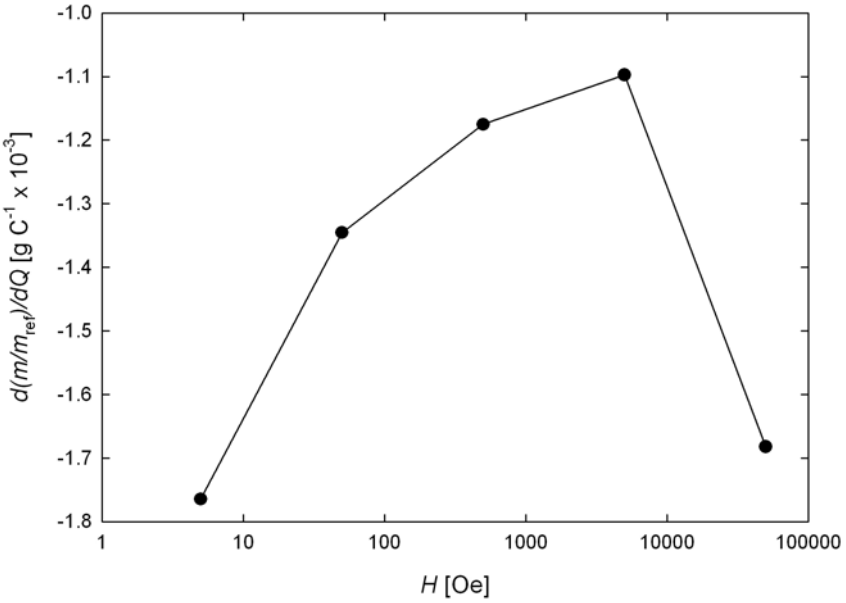

Figure 8.13.: Charge-coefficient β in dependence of the magnetic field H in the chemisorption regime of γ-Fe_2O_3/Pt-composite. m_{ref} refers to the first measured data point of m.

substantially larger in comparison to the few available results on porous nanophase metals where charging was performed in the same manner as in the present study [13, 14, 52, 54]. For ferromagnetic nanocrystalline $Pd_{90}Co_{10}$, a decrease of the magnetic moment of 3 % upon positive charging in the double-layer regime was observed [14]. This variation could not be explained in a simple picture of adding or withdrawing of electrons from the d-band, which in fact should have given rise to the opposite trend, but the charge-induced surface stress was considered as the dominant effect giving rise to the charge-induced tuning of the magnetic moment owing to magnetoelastic coupling [14].

Although, no information on charge-induced surface stress is available for the present γ-Fe_2O_3/Pt-composite, 10 % changes of the magnetization in magnetoelastic response to surface charges appear highly unlikely. Since chemisorption of oxygen species and desorption occurs in the voltage regime of charging, the variation of the magnetization is considered to arise from electrochemically induced reactions at the surface. In fact, in qualitative agreement with the observed trend, a decrease or an increase of the magnetization is to be expected in response to oxidation or reduction reactions at the surface of Fe-oxide, respectively.

According to Jacintho et al. [60], nanoparticles of γ-Fe_2O_3 adsorbed on a silver electrode in an aqueous electrolyte may undergo electrochemical reactions at the surface . The γ-Fe_2O_3 nanoparticles in the aqueous electrolyte are covered by a shell of Fe-hydroxides, essentially ferroxyhite (δ-FeOOH), which is reduced to magnetite (Fe_3O_4) upon cathodic scan. Fe-hydroxides are formed again by reoxidation upon anodic scan [60]. This is reflected in the additional shoulders in the cyclo-voltammogram of the γ-Fe_2O_3/Pt-composite (Fig. 8.4). Such kind of surface reaction, i.e., oxidation of Fe_3O_4 to δ-FeOOH upon positive charging, is in qualitative agreement with the present observation, that the magnetic moment decreases with positive charging, because the specific magnetization of δ-FeOOH ($<$10 emu g^{-1}) [61] is much smaller than that of Fe_3O_4 (90 emu g^{-1}) [61].

Since the difference between the specific magnetization of δ-FeOOH and Fe_3O_4 is in the range of the specific magnetization of γ-Fe_2O_3, one may conclude according to the above notion that the variation of the magnetization of the Fe-oxide by 10 % roughly corresponds to an equal amount of volume fraction (10 %) which undergoes this chemical transformation. In a simple picture of spherical nanoparticles (radius $r = 2.5$ nm) with an Fe-hydroxide shell of the thickness of two monolayers (thickness $\delta = 0.25$ nm), the volume fraction of the Fe-hydroxide shell corresponds to 30 % ($=3\ \delta/r$), which means

that not the entire surface shell but only a fraction of 1/3 of the surface shells undergoes the chemical transformation. This fraction appears to be quite reasonable taking into account that only the surface parts of the non-conducting γ-Fe_2O_3 nanoparticles which are in close contact with the conduction network of the Pt nanoparticles are taking part in the electrochemical reaction.

Indeed the conductive metallic network is necessary for charging as futile charging tests without the conductive network have confirmed. The notion that charging gives rise to chemical shells (δ-FeOOH, Fe_3O_4) with different magnetization is also in line with the observed slight increase of m/m_{ref} with H. The variation in the pseudocapacitive regime (Fig. 8.5) is presumably also due reversible chemisorption processes, but strongly reduced compared to cycling in the extended voltage regime covering complete reduction.

8.5. Comparison with magnetic tunability of multiferroics

The present research results demand for a comparison with other current research fields. One very prominent field of research is the class of multiferroics nowadays [3]. This means the exploration of properties in combined ferromagnetic/ferroelectric nanostructures or nano-sized layer systems which promise a new generation of hard disk writing heads controlled by voltage rather than current just to mention one of the serveral technological interests [6, 62].

With respect to practical application it is of great importance to learn more about the interaction between magnetic and ferroelectric properties. One key factor is the so-called magnetoelectric coupling constant α [3], describing the linear magnetoelectric effect which is deduced from the free energy F according to the Landau theory. Finding or engineering a single phase material in a way that with a linear α an influence of the electric polarization P on the magnetization M becomes possible and vice versa marks the key to revolutionary novel materials in data and information technology. Basically two approaches are feasible: The first is tuning of the linear magnetoelectric constant α in a single phase mulitferroic as Cr_2O_3, Gd_2CuO_4 or $BiFeO_3$ which exhibit ferroelectric as well as antiferromagnetic properties. The linear magnetoelectric constant arises from Landau-Theorie where one obtains the electric polarization term P_i [3]

$$P_i = \alpha_{ij} H_j + \frac{\beta_{ijk}}{2} H_j H_k + ... \tag{8.1}$$

and for the magnetization [3]

$$\mu_0 M_i = \alpha_{ji} E_j + \frac{\gamma_{ijk}}{2} E_j E_k + ... \tag{8.2}$$

with α_{ij} describing the linear magnetoelectric coupling. In fact the linear magnetoelectric coupling constant α is often forbidden or very small so that it is desirable to recover it by chemical substitutions or the application of high magnetic fields [3].

The second ansatz deals with the introduction of indirect coupling coming from induced strain which is not considered when discussing the linear or higher-ordered magneto electric phase. For the realization of the two phase solution a magnetostrictive and a piezoelectric material are brought into contact with each other [3]. Promising approaches are reported for a $Cr_2O_3(111)/(Co/Pt)_3$ heterostructure where cooling under a magnetic field $\mu_0 H$ of 0.6 T and an electric field of E leads to switchable transition of the magnetization M from plus to minus [63]. Theoretical calculations are performed for a $Fe/BaTiO_3$ layer system; for a layer thickness of 1 nm Fe and 2.5 nm $BaTiO_3$ a change of 0.3 μ_B per surface unit is calculated upon applying a coercive electric field E_c of 10 kV for $BaTiO_3$. Comparing this with the bulk moment of Fe with 2.2 μ_B these calculations predict a relative change of 27 %, not taking into account the influence of surface effects and superstructures [64]. Another interesting experimental work for multiphase materials is reported in connection with a $BiFeO_3/CoFe_2O_4$ heterostructure. Pillars of ferrimagnetic $CoFe_2O_4$ are embedded in a matrix of $BiFeO_3$ which acts as ferroelectric host here. A magnetic field is set up to 20 kOe. It is possible to vary the magnetic anisotropy of $CoFe_2O_4$ by applying a voltage of ± 12 V to $BiFeO_3$ (thickness: $\approx$200 nm) as a result of the piezoelectric effect. With a linear magnetoelectric coupling constant α ($\Delta M/\Delta E$) of 0.01 G cm V^{-1} the response of M on the electric field E is characterized [65].

Let us now draw a comparison between literature results and the results in the present work. For the above mentioned 200 nm $BiFeO_3/CoFe_2O_4$ heterostructure $\alpha = 0.01$ G cm V^{-1} can be transformed to $\Delta M/\Delta U$ by

$$\alpha = \frac{\Delta M}{\Delta U} = 10^{-4} \frac{1}{d} \frac{\Delta M}{\Delta E} \tag{8.3}$$

with d denoting the thickness of the sample. Eq. 8.3 yields 5×10^{-2} T V^{-1} for $\Delta M/\Delta U$. This can be compared well with measurements on $Fe_{50}Pd_{50}$ performed at 20 kOe. The

density of $Fe_{50}Pd_{50}$ is estimated with 10 g cm^{-3}. Multiplying the in-situ determined moment in emu g^{-1} with the density ρ, the volume weighted magnetization M is received in emu cm^{-3}. With a factor of $4\pi\times10^{-4}$ $\Delta M/\Delta U$ can be determined in units of T V^{-1}. $\Delta M/\Delta U$ is found to be 4.23×10^{-4} T V^{-1} for $Fe_{50}Pd_{50}$ ($\Delta m/m_{ref,Fe_{50}Pd_{50}} = 0.22\,\%$ at 20 kOe). In a similar way this evaluation can be applied to γ-Fe_2O_3/Pt-composite with the 1:3 weight-% composition ($\Delta m/m_{ref,\gamma-Fe_2O_3/Pt} = 10.4\,\%$ at 50 kOe). At 50 kOe $\Delta M/\Delta U$ amounts to 0.70×10^{-2} T V^{-1}. This comparison demonstrates that in the case of γ-Fe_2O_3/Pt-composite by applying a voltage of ±0.85 V α is at the same order of magnitude as in $BiFeO_3/CoFe_2O_4$ heterostructures where α is switched with ±10 V. This leads to the conclusion that charge-induced magnetic moment tuning in γ-Fe_2O_3/Pt-composites exhibits a competitive concept compared with other findings in literature.

CHAPTER 9

Nanocrystalline FePt

Nanoparticles and systems with ligament-stabilized nanoparticles are in the focus of many different scientific fields [66, 67]. Tailoring the properties of a nanoscaled system has been performed in manifold ways, for example thermal annealing [9], composition controlling [68] and ligand exchange [8, 18]. All these methods tailor the material properties irreversibly. FePt-nanoparticles produced according to the method of Sun et al. [8] exhibit a high surface-to-volume ratio due to the small crystallite size. The small size is only possible with the utilization of ligament stabilization by oleic acid and oleylamine. This ligament coating prevents the FePt-nanoparticles from charging in aqueous electrolytes which is the main focus of the present work. A method by Oliver Muth demonstrates one approach to remove the ligands with a repeated washing procedure [18]. Bare FePt-particles are well-suited for in-situ charging experiments in SQUID as they can be processed as common powder sample with a higher surface-to-volume ratio compared to commercially available nanopowder [11] or nanopowder received from other methods as for example nanocrystallite condensation under inertgas (see above in the present work).

At first FePt-particles with different coatings are synthesized and studied by XRD, TEM and SQUID magnetometry. The microstructure was studied to support the understandings of the magnetic properties. In the text to follow abbreviations for the ligand coatings are used. FePt/oleic acid/oleylamine will be denoted as $FePt_{ol}$, FePt/octanoic acid/octylamine as $FePt_{oct}$ and FePt/hexanoic acid/hexylamine as $FePt_{hex}$. After ligand removal the charge-induced variation of the magnetic moment of the bare FePt-nanoparticles is investigated.

9.1. Structural characterization by X-ray diffraction and Transmission Electron Microscopy

XRD of $FePt_{ol}$ in the as-received state reveals a fcc structure (Fig. 9.1). Upon annealing at 600 °C for 2h a tranformation to the ordered $L1_0$ structure is observed (Fig. 9.1).

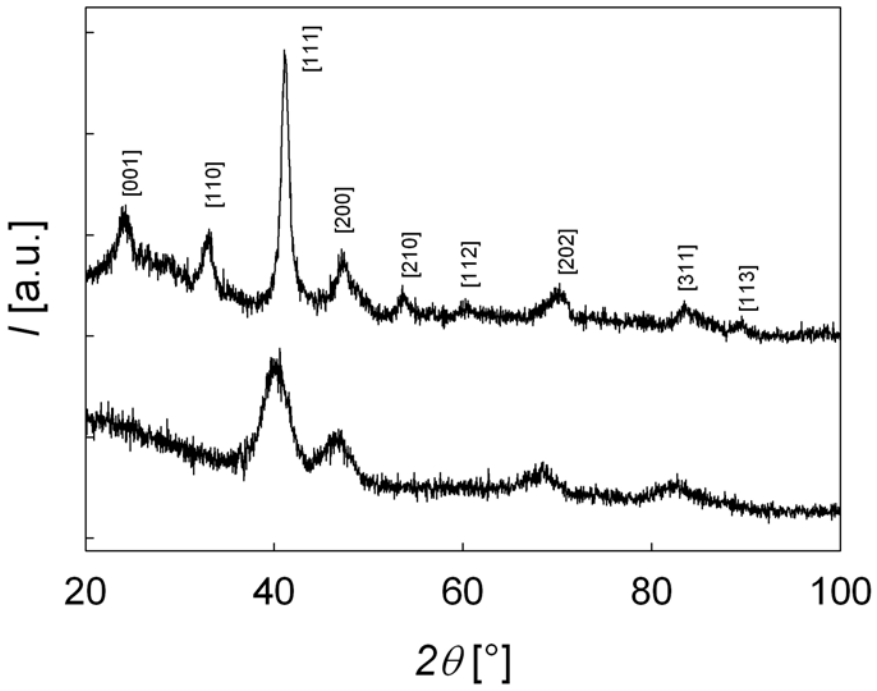

Figure 9.1.: XRD of FePt/octanoic acid/octylamine in as-synthesized state and after annealing (600 °C for 2 h; Miller-indices are given in brackets)

The crystallite size d is determined by means of the Scherrer formula [69]

$$d = \frac{G\lambda}{\Lambda cos(\theta)} \tag{9.1}$$

where Λ denotes the Full Width at Half Maximum for the XRD-peaks, λ stands for the wavelength of the diffractometer anode material (Cu K_α: 0.154 nm), θ denotes the diffraction angle of the goniometer and G the geometry factor.

From the broadening of the various Bragg peaks (Tab. 9.1) a mean crystallite size of 3.6 nm is derived for the as-synthesized state.

In addition to the crystallite size determined from XRD, TEM yields information on the crystallite size distribution. The particle size and particle size distribution is determined

θ [°]	Λ [°]	d [nm]
40.227	3.079	3.052
46.829	3.066	3.136
68.400	2.408	4.430
82.435	3.224	3.638

Table 9.1.: Particle size evaluated with Eq. (9.1)

from Fig. 9.2 by 'digital micrograph' pictures taken by Ilse Papst-Letofsky, Institute of Electron Microscopy and Fine Structure Research.

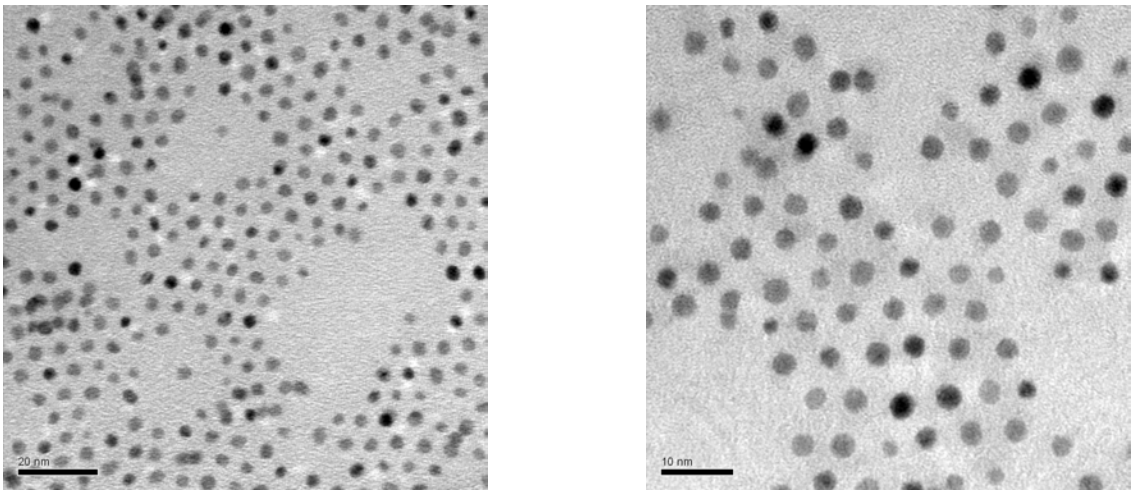

(a) (b)

Figure 9.2.: Bright field TEM pictures of FePt/oleic acid/oleylamine nanostructures

The histogram in Fig. 9.3 depicts the crystallite size distribution. A normal distribution yields a slightly better fit compared to a log-normal distribution. Log-normal size distributions are for instance observed for gas-phase synthesized particles owing to particle coalescence [70]. Due to the ligands in the wet-chemical synthesis, coalescence is suppressed which give may rise to the normal size distribution.

After ligand exchange from oleic acid ($FePt_{ol}$) with an interparticle distance of 3.3 nm to octanoic acid ($FePt_{oct}$) and hexanoic acid ($FePt_{hex}$) significantly smaller interparticle distances of ca. 2.5 nm and 1.9 nm are observed, respectively (Fig. 9.4, $FePt_{oct}$ not included - TEM pictures taken by Karin Wewerka, Institute of Electron Microscopy and Fine Structure Research). This demonstrates that the interparticle distance can be chemically tuned by means of the ligand shell.

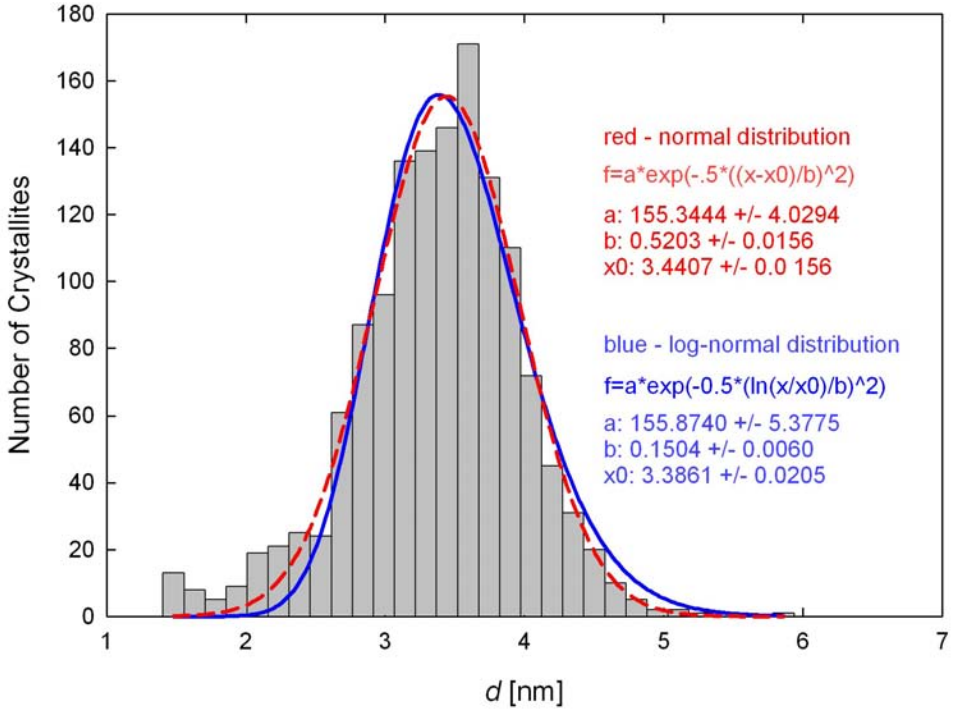

Figure 9.3.: Size distribution of FePt/oleic acid/oleylamine nanoparticles determined from TEM micrographs. The fitting parameters given in the plot characterize the fit for normal (red) and log-normal distribution (blue).

9.2. Magnetic pre-characterization

A Zero Field Cooling/Field Cooling (ZFC/FC) measurement of $FePt_{ol}$ is shown in Fig. 9.5.

Above the blocking temperature the same behaviour occurs for ZFC and FC as characteristic for superparamagnetism. The transition between ferromagnetism and superparamagnetism is marked by the blocking temperature T_b at 18 K (Fig. 9.5). The narrow size distribution as deduced from TEM is also nicely demonstrated by the sharp increase of the ZFC curve in Fig. 9.5 [59].

Fig. 9.6 illustrates the hysteresis behaviour for 4.2 K and 300 K. The transition from ferromagnetic to superparamagnetic behaviour with increasing T is demonstrated by the field dependence of m (Fig. 9.6). Comparing FePt-nanoparticles with different ligands, i.e. $FePt_{ol}$, $FePt_{oct}$ and $FePt_{hex}$ no significant variation of the magnetic moment m can be observed (Fig. 9.7). This indicates that the variation of the interparticle distance does not significantly influence the coupling between the particles. More detailed ZFC/FC studies on the coated FePt-nanoparticles were performed in collaboration with K. Nadeem [59].

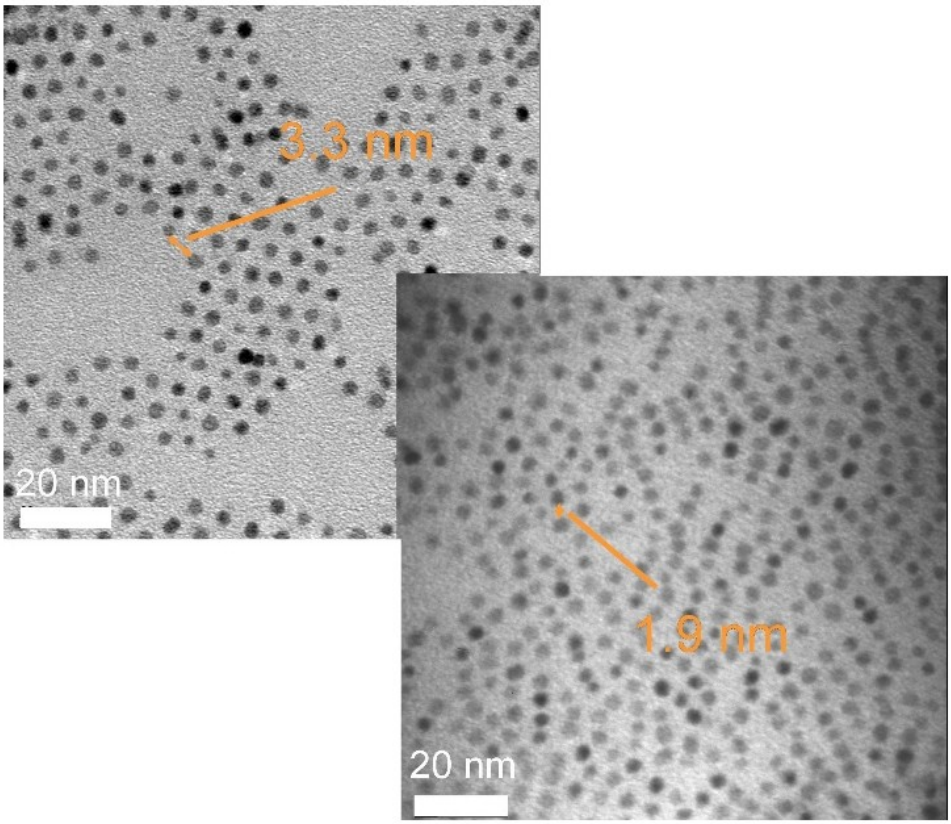

Figure 9.4.: Interparticle distance of FePt-nanoparticles with different ligands; left: oleic acid/oleylamine-shell: particle distance 3.3 nm, right: hexanoic acid/hexylamine-shell: particle distance 1.9 nm (octanoic acid/octylamine shell not shown here).

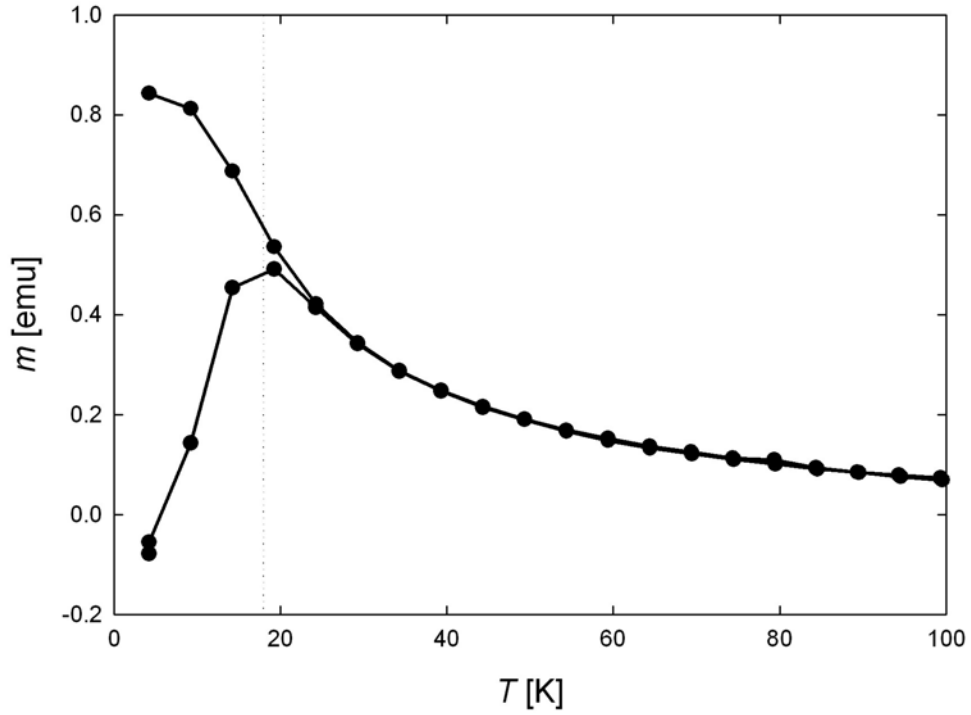

Figure 9.5.: ZFC/FC curve of FePt/oleic acid/oleylamine at 50 Oe; the dotted line marks the blocking temperature T_b at 18 K

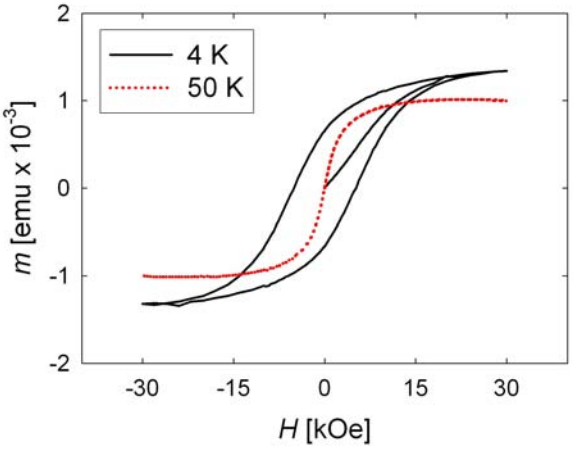

Figure 9.6.: Comparison of hysteresis curves for FePt/oleic acid/oleylamine at 4.2 K and 300 K.

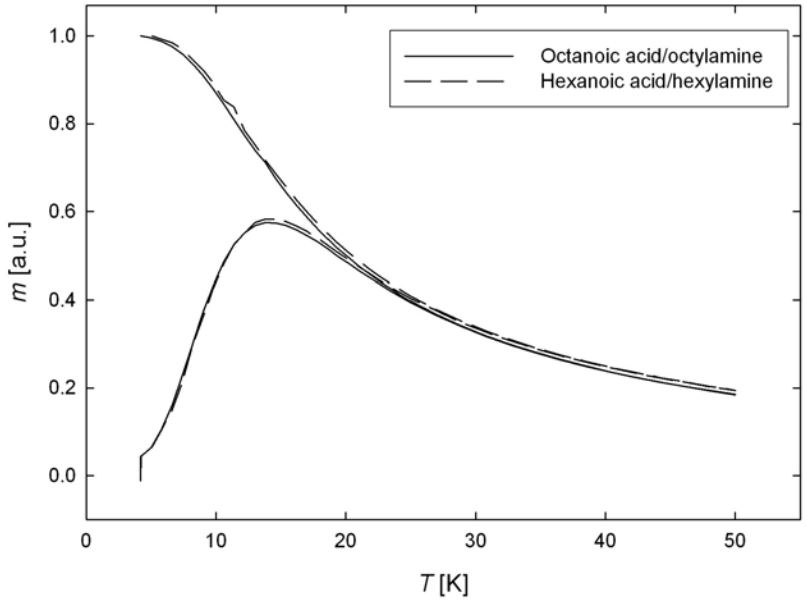

Figure 9.7.: Repeated ZFC/FC measurement for FePt/octanoic acid/octylamine and FePt/hexanoic acid/hexylamine at 50 Oe

9.3. Ligand removal and electrochemical pre-characterization of chemically synthesized FePt

Regarding the use for charging purposes the ligands from the FePt-particle surface have to be removed. For this purpose a method described in the doctoral thesis of O. Muth [18] was used in a slightly different manner as described in the appendix. For this approach 5 ml stock solution of $FePt_{ol}$ dispersed in n-hexane are taken and precipitated with 15 ml of ethanol. Subsequent centrifugation leads to a separation of FePt-particles and the oleic acid/oleylamine excess dispersed in n-hexane/ethanol. The excess solution is decanted and pure n-hexane (3-5 ml without any ligands is poured on it [18]. Ultrasonic treatment is avoided as an intermixture between ligands and FePt-particles is not desirable. $FePt_{ol}$ redisperses in n-hexane while a small amount of FePt (identifiable as dark grey precipitation) remains at the bottom of the centrifugation tube. Repeating this washing cycle 5-6 $\times$ leads to an undispersable precipitation of FePt which is dried for 1-2 h under $\approx$ 1 mbar vacuum. The resulting sample is stored under Argon atmosphere in the glove box (MBraun Unilab) for further processing (section 3.1.2.1).

The electrochemical behaviour of chemically synthesized FePt is performed by means of a cyclovoltammogram (CV) in 1 M KOH (Fig. 9.8). The applied charge Q (0.05 C g^{-1})

is too small for a clear discrimination between the CV of the Au-reference and the FePt sample. This indicates that removing of oleic acid/oleylamine ligand shell from the FePt particles is not completed.

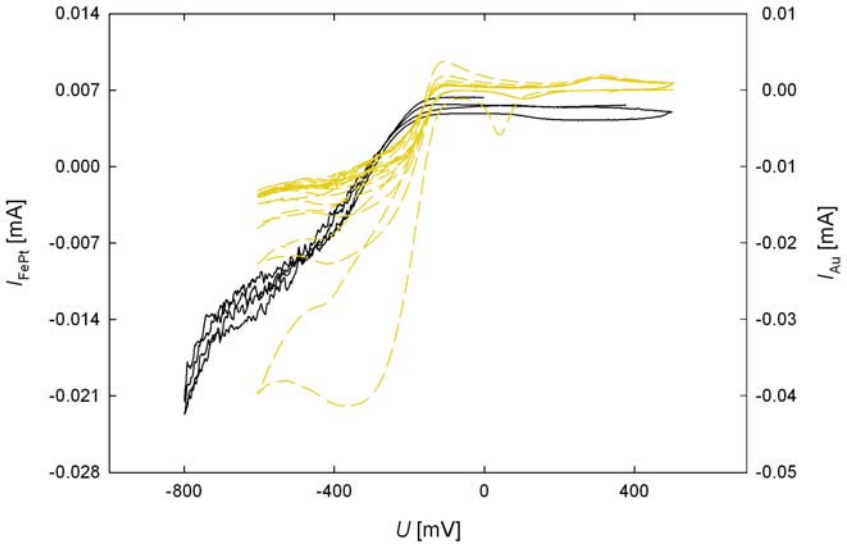

Figure 9.8.: Cyclovoltammogram of chemically synthesized FePt (full black line) in 1-M KOH compared with a reference measurement on a Au-wire wired around a piece of PTFE as reference (golden dashed line)

9.4. Charge-induced variation of magnetic moment

The FePt-sample is charged with an alternating voltage of +400 mV and -600 mV. The in-situ SQUID charging experiments where performed at fields ranging from 50 Oe to 50 kOe. Fig. 9.9 represents the measurements at 5 kOe. Positive charging decreases the magnetic moment of FePt while negative charging increases it. The supplemental measurements for the other fields are presented in the appendix (section 13.4.4).

The charge coefficient $\beta = \frac{d(m/m_{ref})}{dQ}$ (obtained by linear fitting in Fig. 9.10) is negative for all field settings.

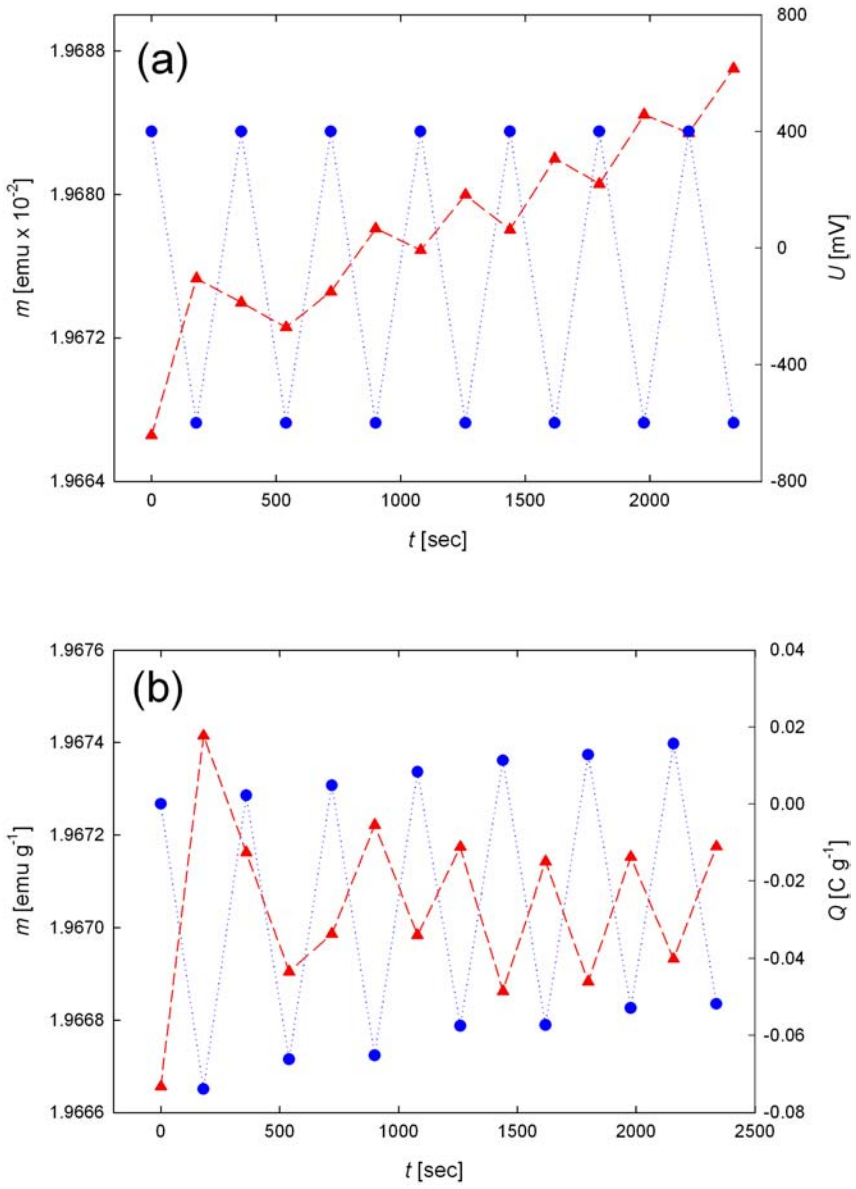

Figure 9.9.: Magnetic moment m (▲) of chemically synthesized FePt measured at 5 kOe upon consecutive cycling in the regime of adsorption/desorption (a) charging voltage U (●), (b) imposed charge Q (●). t: time. m, Q in (b) drift-corrected.

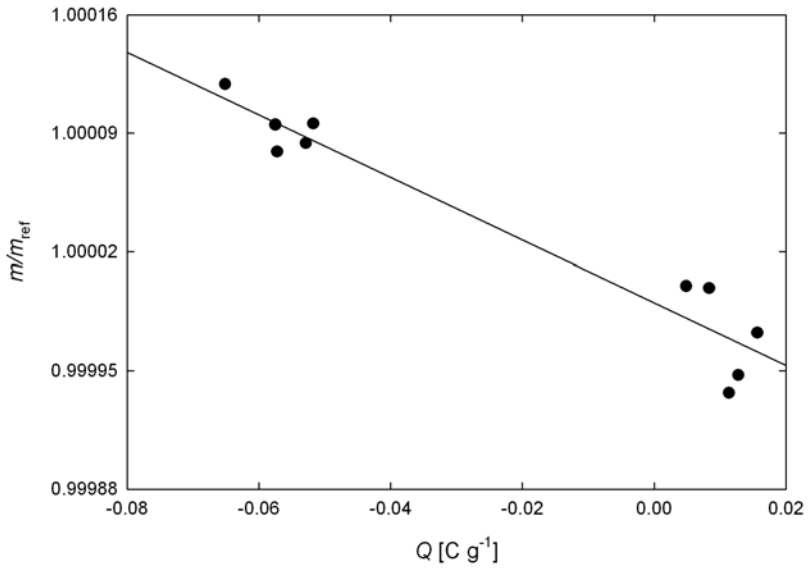

Figure 9.10.: Relative magnetic moment m/m_{ref} of chemically synthesized FePt measured at 5 kOe in dependence of charge Q. m_{ref} refers to the first measured data point. m, Q drift-corrected.

Fig. 9.11 illustrates the magnetic field dependence of FePt. The magnetic moment m shows the characteristic increase with increasing magnetic field. At 50 kOe a saturation magnetization of 6.09 emu g^{-1} is reached. The variation of the magnetic moment Δm is highest at 50 kOe. This can be expected as the highest m implies the highest Δm in the case of not extremely non-linear behaviour. When looking at the relative variation of the magnetic moment, $\Delta m/m_{ref}$, one can observe similar values at 500 Oe and 50 kOe while at 5 kOe $\Delta m/m_{ref}$ is significantly smaller. m_{ref} refers to the first measured magnetic moment data point. The charge coefficient $\beta = \frac{d(m/m_{ref})}{dQ}$ is smallest for a field H of 5 kOe while it is highest at 500 Oe.

Tab. 9.2 summarizes the data obtained from the in-situ SQUID charging experiments for chemically synthesized FePt. With a maximal applied charge of 0.08 C g^{-1} it becomes obvious that only a very small fraction of FePt is charged directly or indirectly via the coiled Au-wire. For proper charging the production process and especially the ligand removal have to be improved so that higher amounts of charge can be applied.

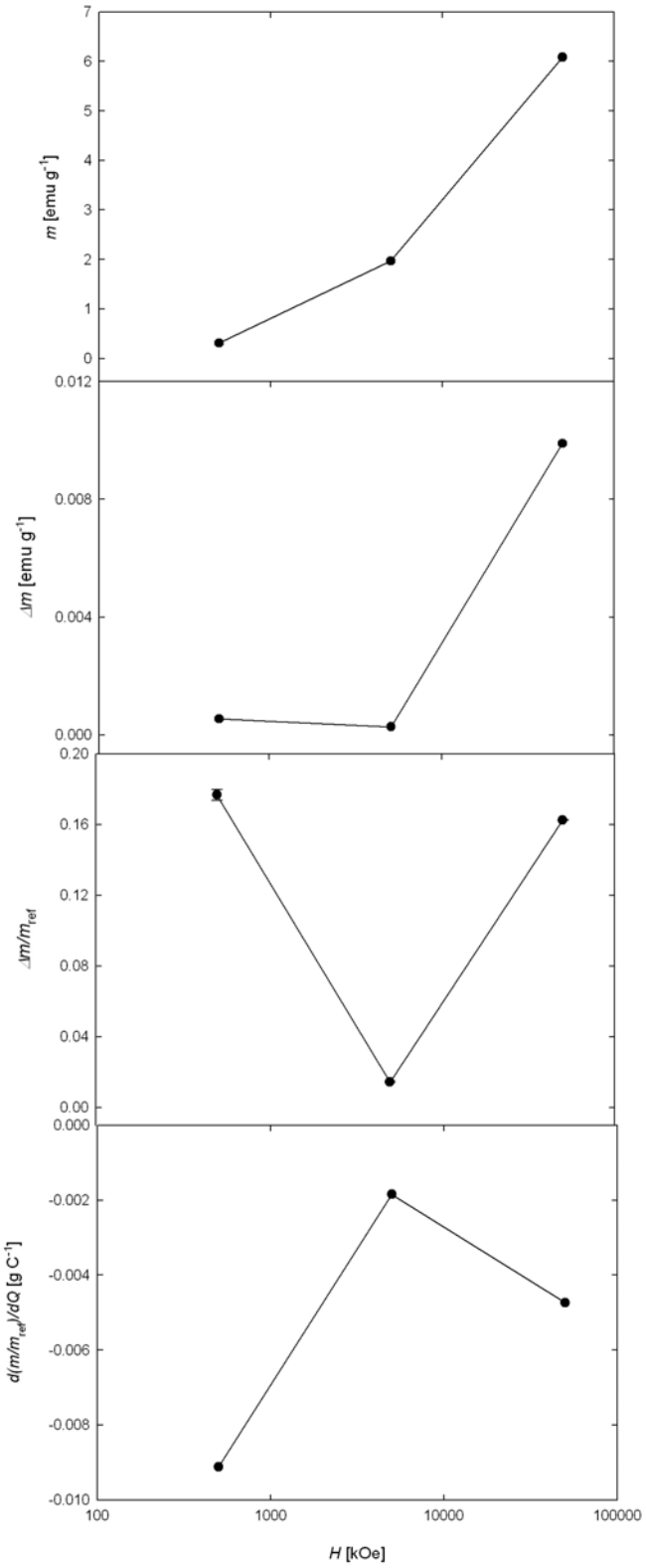

Figure 9.11.: Charge-induced variation of magnetic moment of chemically synthesized FePt upon cycling between -600 mV and +400 mV in dependence of magnetic field H; (a) magnetic moment m, (b) variation Δm, (c) absolute value of relative variation $\Delta m/m_{ref}$ with m_{ref} denoting the first measured datapoint, (d) charge coefficient $\beta = \frac{d(m/m_{ref})}{dQ}$

H [Oe]	Δm $[\frac{emu}{g}]$	$\frac{\Delta m}{m_{ref}}$ [%]	$\frac{d(m/m_{ref})}{dQ}$ $[\frac{g}{C}]$	$\frac{dQ}{dt}$ $[\frac{C}{g\ sec}]$	$\frac{dm}{dt}$ $[\frac{emu}{g\ sec}]$	$r^2_{\frac{d(m/m_{ref})}{dQ}}$
500	5.50×10^{-4}	0.18	-9.12×10^{-3}	1.17×10^{-5}	1.42×10^{-7}	0.30
5000	2.85×10^{-4}	0.02	-1.85×10^{-3}	1.37×10^{-5}	6.53×10^{-7}	0.93
50000	9.90×10^{-3}	0.16	-4.73×10^{-3}	5.98×10^{-6}	-7.44×10^{-6}	0.27

Table 9.2.: Charge-induced variation of magnetic moment; summary for chemically synthesized FePt. For definition of symbols see Tab. 5.1

9.5. Discussion

The charge-induced tuning turns out to be difficult as consecutive washing cycles only partially remove the ligands from the FePt-nanoparticles. As a result of that the applied charges are ca. a factor 100-500× smaller compared to charges on FePd or Co received from inertgas condensation (Tab. 4.1). The variation $(\Delta m/m_{ref})_{max}$ of 0.18 % at 500 Oe is smaller compared to most of the nanocrystalline powder samples. However, the charge-coefficient β for FePt exhibits the highest values of all investigated samples in the thesis. The surface-to-volume ratio is 3.5× higher than for inertgas condensed powder. This enhancement can be given as one explanation for the high β. A classification whether pseudocapacitive charging, adsorption and desorption processes or double layer charging contribute to the change of the magnetic moment can not be given since a small amount of charge could be imposed only (Fig. 9.8).

For 500 Oe, 5 kOe and 50 kOe positive charging increases the magnetic moment while negative charging decreases it. This is consistent with the findings for Co in the present work (Tab. 4.1) and findings in literature [14]. As a consequence the variation of m cannot be explained in terms of band filling [13] or spin dependent charge carrier screening [71]. The H-dependent sign inversion observed in the FePd compositions is not observed for FePt. Ghosh et al. [14] assigned the variation of m for CoPd in a non-aqueous electrolyte to a reversible strain where the contraction corresponds to a decrease in magnetization while the expansion of CoPd yields an increase of m . Similar studies were performed on NiPd in ethylacetate/$LiClO_4$ where charge-induced magnetostriction is given as reason for Δm [52]. The effect of charge on strain of nanoporous Pt in 1-M KOH has been directly demonstrated by Weissmüller et al. [2]. A further interesting approach is given by DFT-calculations of Zhang et al. [72] where charging of FePt-supercells influences the magnetocrystalline anisotropy energy MAE. In these studies positive charging decreases the MAE while negative charging increases it. However, these calculations where performed

for a monolayer system. In the present case of a complex nanocrystalline FePt-structure the response of the MAE and moreover the magnetic moment m upon charging is not straightforward.

We expect that a complete removal of the ligand shell would lead to a much larger variation of m.

CHAPTER 10

Reference measurements of in-situ charging in SQUID

The principle of in-situ charging of nanophase metals for property tuning was applied in the present work for the first time with SQUID magnetometry. The few other available studies on this topic were performed by vibrating sample magnetometers [13]. Therefore, reference measurements are necessary in order to study in how far the SQUID measurements are affected by the electrochemical charging. Along with the complex measurement setup the diamagnetism of the electrochemical cell components has to be considered.

10.1. Diamagnetic response of electrochemical cell

When investigating the response of nanophase samples on electrochemical charging by SQUID magnetometry the diamagnetic response of the electrochemical cell has to be taken into account. For the evaluation of the magnetic moment of the sample this diamagnetic contribution is subtracted. For this purpose the magnetic moment m of an empty electrochemical cell is measured at 70 kOe, 20 kOe, 5 kOe, and 2 kOe (Fig. 10.1). Below 2 kOe no reliable diamagnetic cell signal can be obtained. From the linear regression a diamagnetic susceptibility χ_{dia} with -1.243$\times 10^{-7}$ $\frac{emu}{Oe}$ is obtained [32]. For a ferromagnetic sample the relative diamagnetic contribution to the magnetic signal is negligible (1.9 % for γ-Fe_2O_3/Pt-composite at 50 kOe).

Especially for measurements on paramagnetic samples (Pt, Pd) at high magnetic fields the diamagnetism of the electrochemical cell components may become dominant. Upon

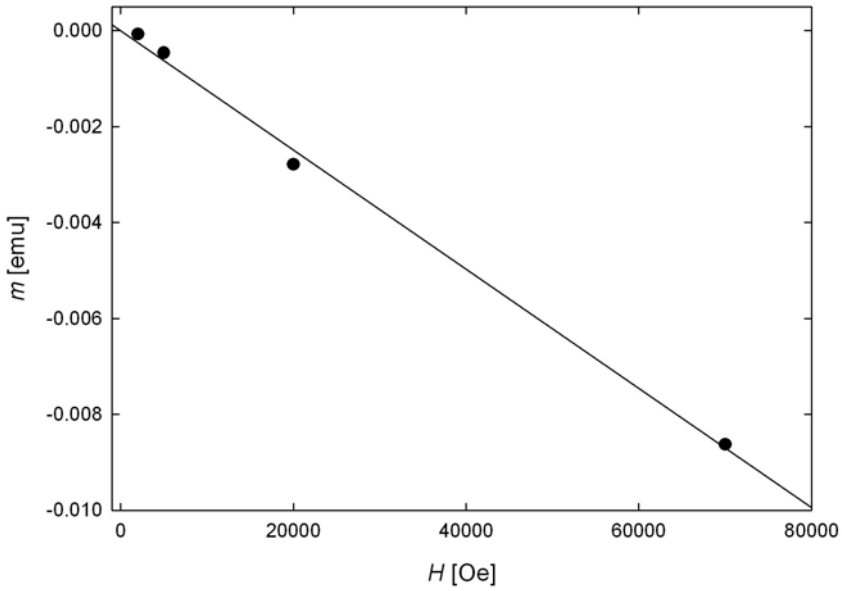

Figure 10.1.: Magnetic moment m of the electrochemical cell [32]. H: magnetic field.

using an empty electrochemical cell the diamagnetic susceptibility is determined. The moment of the empty cell as determined above is subtracted from all measurements.

10.2. Charge-dependent magnetic moment of reference sample

In order to verify the measured effects on the magnetic samples (Co, Pd, FePd) and to study the behaviour of the electrochemical cell currents in an applied magnetic field H, reference measurements under in-situ charging with carbon tissue as WE were performed. All other cell components including the carbon tissue counter electrode CE remain the same as for the measurements on the nanophase samples. Centering the sample in SQUID is difficult below a magnetic field of 1 kOe as the fit from the SQUID for determining m features significant deviations. Therefore the magnetic measurements for the reference cell were restricted to 1 kOe, 5 kOe and 50 kOe.

The most important influence on the measurements is expected to result from the measuring current I_{meas} which is flowing in the electrochemical cell during every chronoamperometry charging sequence. Reproducing the current flow in the electrochemical reference cell is achieved by applying a charging voltage U of ± 500 mV to the electrochemical reference cell which is associated with a current of more than 80 μA.

For 50 kOe an increase of m upon positive charging and vice versa is observed (Fig. 10.2 (a)). The variation Δm of the magnetic moment is 1.06×10^{-5} emu. Normalizing Δm

with the mean of the measured m-data points yield a relative variation of $\frac{\Delta m}{m_0} = 0.4\,\%$. The behaviour at 5 kOe is qualitatively similar to that at 50 kOe (Fig. 10.2(a) and Fig. 10.2(b)). Positive charging leads to an increase of m while negative charging decreases it. The variation Δm of the magnetic moment is 0.16×10^{-5} emu which corresponds to a relative variation of $\Delta m/m_0$ of 3.3 %. Compared to 50 kOe and 5 kOe, the magnetic moment of the reference cell at 1 kOe shows an opposite trend with charging (Fig. 10.2(c)). The charge-induced variation of m is -1.93×10^{-5} emu which corresponds to a $\Delta m/m_0$ of 58 % [32].

In addition to cycling, the magnetic moment of the reference cell was also monitored during chronoamperometric charging (Fig. 10.3). m shows a linear variation with the charging current.

10.3. Discussion

The validation of an influence of the measuring setup on the magnetic moment measurements is an important issue both for assessment of present measurements of charge-induced property tuning of nanophase materials as well as for electrochemical studies in SQUID in general. In the following the response of the reference cell upon charging and the influence of the charging current is discussed. Jette et al. [73] describe in-situ cyclovoltammetry in a SQUID where the measured magnetic moment corresponds well to the current characteristic. In contrast to that the review article from Juzeliũnas [74] discusses the in-situ investigation of corrosion currents in a SQUID and concludes that the various directions of the current in the SQUID cancel out the respective influences on the magnetic moment.

10.3.1. Effect of charging current

In order to discuss the influence of the charging current, we adopt the simple picture that the Au contact wire acts as a magnetic coil which gives rise to a magnetic moment [21]

$$\Delta m_{coil} = n I_{leak,max} A \tag{10.1}$$

with n denoting the number of windings, A the cross section of the coil, and $I_{leak,max}$ the residual leakage current which is flowing during the magnetic measurement after charging

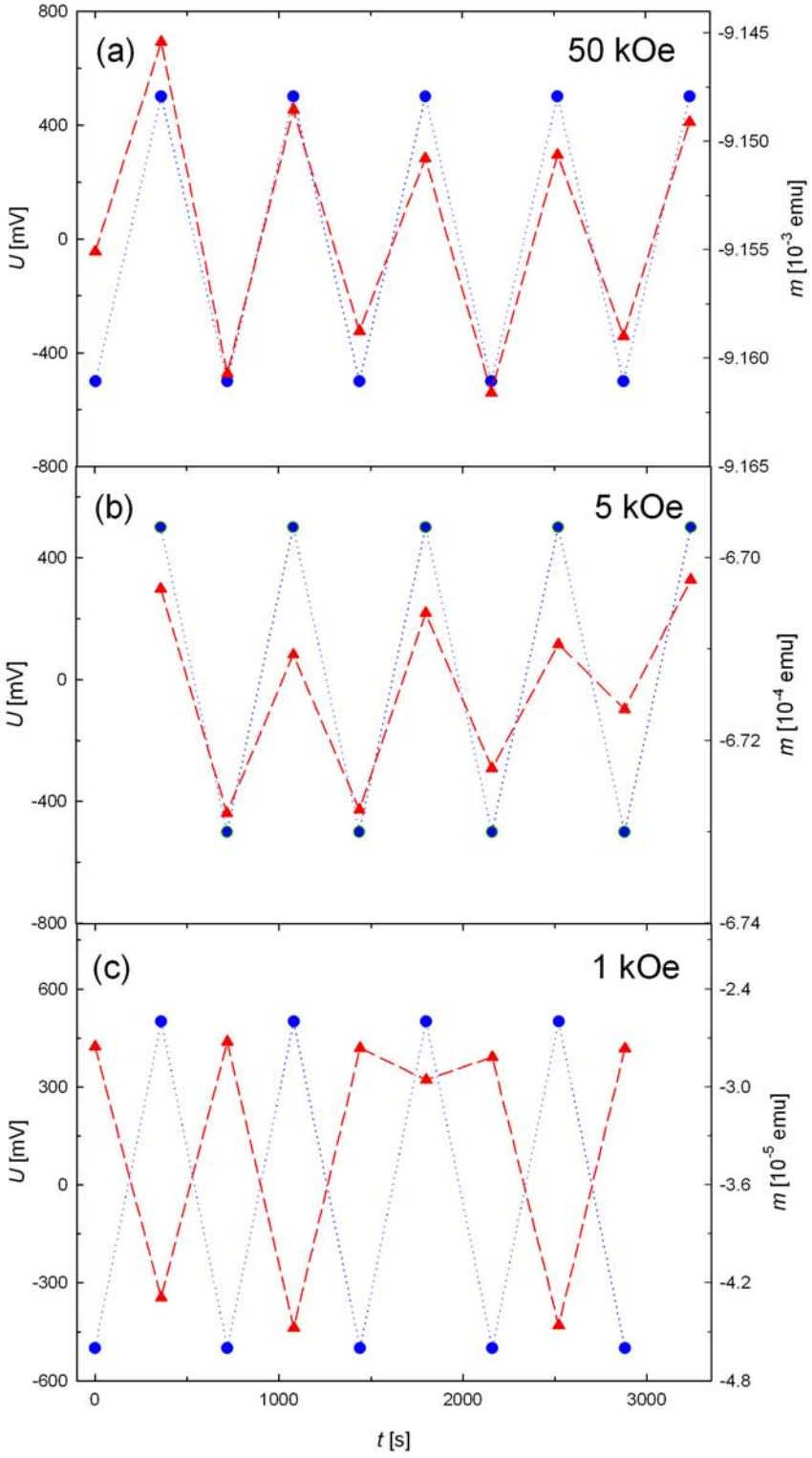

Figure 10.2.: Magnetic moment of reference cell upon cycling between the charging voltage U of $\pm 500\,\mathrm{mV}$. t: time; (a) 50 kOe, (b) 5 kOe and (c) 1 kOe.

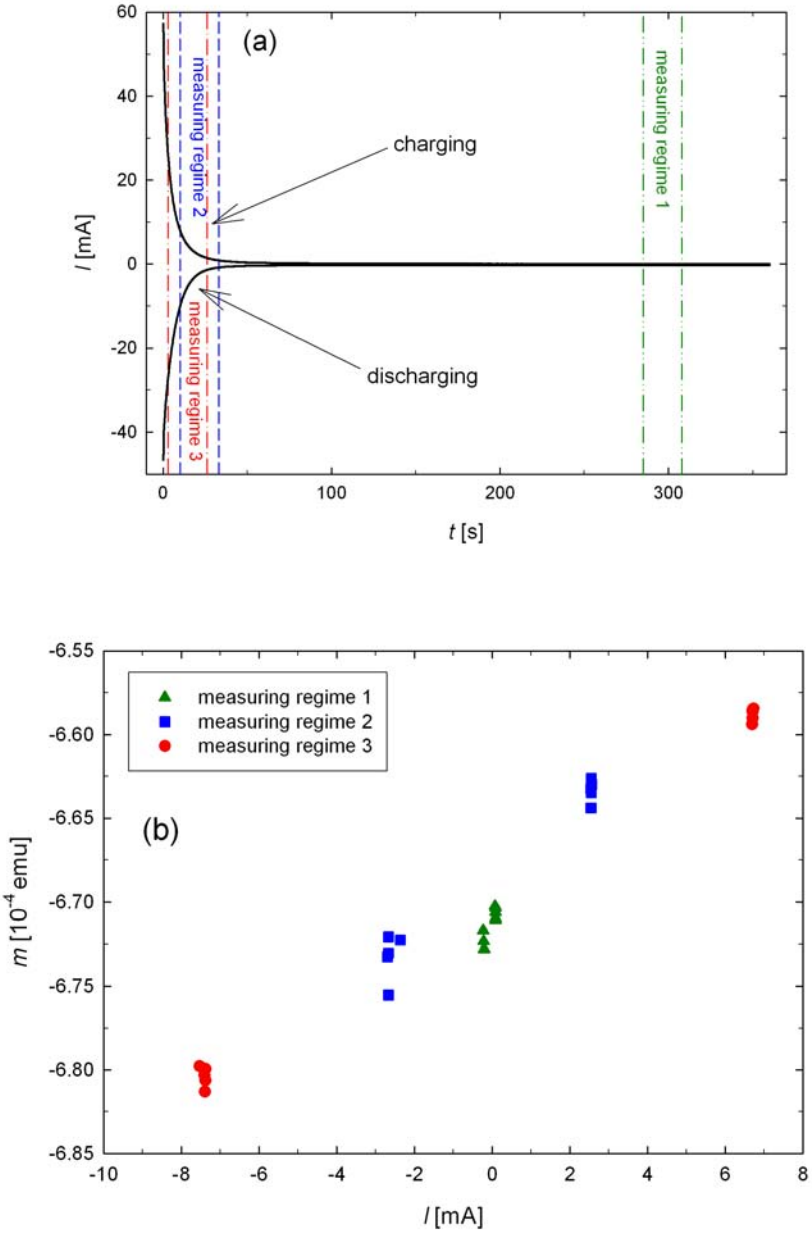

Figure 10.3.: Magnetic moment m of reference cell measured during chronoamperometric charging for various charging intervalls at 5 kOe. (a) charging characteristic, (b) m in dependence of charging current [32].

is completed. For the coil an area of $1\,mm^2$ is assumed (see appendix, section 13.5 for more details). Since Δm_{coil} is independent of H, whereas the charge-induced variation Δm of the magnetic moment increases with m the effect of Δm_{coil} is largest at low fields when m is low. Δm_{coil} is listed in detail in Tab. 4.1.

10.3.2. Effect of cell

In order to check whether the charging effects vanish upon using a diamagnetic reference sample, a cell is measured with carbon tissue as working electrode (see section 10.2). Simply charging an empty cell in potentiostatic mode is not suitable as the occuring currents are at least two orders of magnitude too small[1]. The evaluation of the results in section 10.2 exhibits at the first sight a strong correlation between leakage current and variation Δm_{ref} of the reference cell at the order of 10^{-5} emu with $I_{leak} \approx 250\,\mu A$ (Fig. 10.3). Upon employing Eq. 10.1 one can calculate with a current I of $250\,\mu A$ an influence of the moment of $\Delta m_{coil} = 2.9{\times}10^{-6}$ emu which is one order of magnitude smaller compared to the measuring result of the reference cell at 50 kOe. However, at 5 kOe Δm_{ref} and Δm_{coil} are at the same order of magnitude. Upon only taking into consideration a current flow through a coil one would expect Δm_{coil} to be constant which is not the case here. When going down to 1 kOe Δm changes the sign. This behaviour can not be explained by simple electrodynamics and therefore another reason must exist. The variation might also be assigned to charging effects imposed on the carbon cloth used for the reference measurements.

10.3.3. Comparison with magnetic measurements on nanocrystalline samples

With the help of Tab. 4.1 it is possible to validate the variation Δm of the magnetic moment for the studied material classes. Upon comparing the measured variation Δm of the magnetic moment (in emu) with Δm_{coil} calculated with Eq. 10.1 it is found that the measured Δm is in general larger compared to Δm_{coil}. An exception is the pseudocapacitive charging regime of the γ-Fe_2O_3/Pt-composite at 50 Oe and 500 Oe. Also for Pd at 200 Oe Δm_{coil} is larger than the charge-induced Δm. For all other magnetic measurements Δm_{coil} is lower than the measured Δm.

Fig. 10.4 depicts the influence of the variation of m of a reference cell with a carbon tissue

[1]Potentiostatic charging yields $\approx 1\,\mu A$ upon potentiostatic charging of a Au-wire while charging a nanoporous pellet exhibits leakage currents at the order of $\approx 100\,\mu A$

as working electrode on the magnetic measurements at 50 kOe. It clearly demonstrates that for ferromagnetic samples in the chemical regime the influence of the cell is negligible. This holds for all measurements at and above 1 kOe.

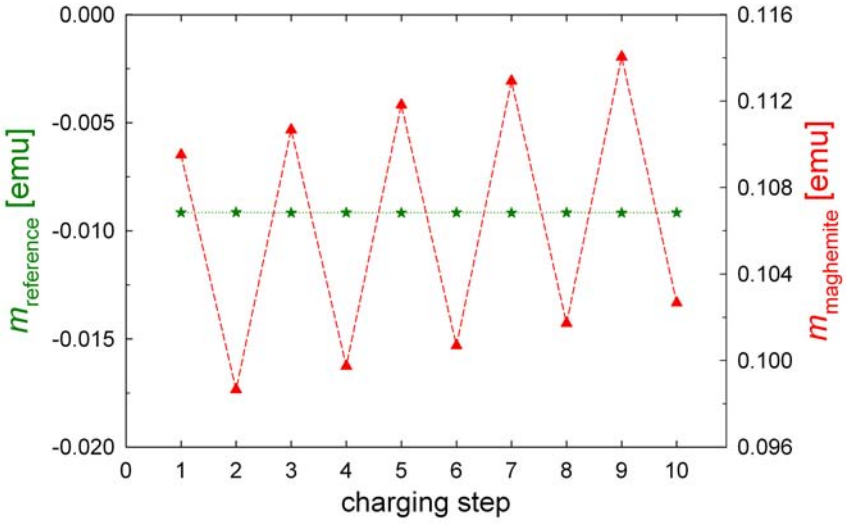

Figure 10.4.: Charge-induced magnetic moment variation of a γ-Fe_2O_3/Pt-composite compared with the charge-induced magnetic moment variation of a reference cell (carbon tissue) at 50 kOe [32].

CHAPTER 11

Charge-induced resistance variation of nanoporous Au

The measurements on nanoporous Au aim at a comparison of the charge-induced variation of magnetism with the charge induced variation of resistance [1]. Furthermore the relative variation of the resistance $\Delta R/R$ between nanoporous and nanocrystalline metals is investigated to clarify the influence of grain boundaries. Compared to earlier studies the charging regime is also extended to the regime of adsorption and desorption of oxygen.

11.1. Experimental Results

Results of electrical resistance measurements on pure nanoporous Au in dependence of voltage $U_{charging}$ used for charging in the range $-700\,\mathrm{mV}$ and $+100\,\mathrm{mV}$ are shown in Fig. 11.1a. The corresponding variation with the imposed specific surface charge ΔQ upon cycling is depicted in Fig. 11.1b. A fully reversible variation of the electrical resistance of ca. 6% occurs, where adding or removing of electrons gives rise to a decrease or increase of R, respectively. The variation of R with $U_{charging}$ (Fig. 11.1.a) in this regime is nearly independent of the direction of charging, indicating that this variation is due the imposed surface charge (i.e., double layer formation) rather than due to chemical effects. This conclusion is further supported by cyclic voltammograms of the np-Au sample (Fig. 11.2). From the linear part of the $\Delta R/R - \Delta Q$ curve (Fig. 11.1b) a charge

[1] The measurements, evaluations and discussions on nanoporous Au were done by Patrick Wahl within the framework of his master thesis under my co-supervision [39]. Text and figures of presented in section 3.4 and 11 are taken from the published article [40] with the permission of the editor.

coefficient $(\Delta R/R)/\Delta Q = 2.2 \times 10^{-2}$ g/C can be deduced (Table 1).

Upon increasing the charging voltage towards more positive values, the regime is reached ($U_{charging} > 100$ mV) where specific adsorption of negative ions occurs as shown in the cyclo-voltagram in Fig. 11.2. The most common interpretation is the chemisorption of oxygen atoms to the Au surface (Au-OH and Au-O). This electrochemical process is reversed upon charging in the cathodic direction which gives rise to desorption with a maximum at $U_{charging} = -100$ mV. Cycling in this extended voltage range of specific adsorption and desorption gives rise to a pronounced increase of the charge-induced resistance variation as compared to the regime of double layer charging. The resistance increases reversibly by ca. 43% upon cycling between -400 mV and $+800$ mV. The R-$U_{charging}$ characteristic shows a significant hysteresis (Fig. 11.3a). The much larger resistance variation in the regime of specific adsorption and desorption as compared to the double layer is due to the higher charge imposed chemically (compare ΔQ in Fig. 11.3b and Fig. 11.1b). Although the resistance variation in the chemical regime is much higher, the charge coefficient $(\Delta R/R)/\Delta Q$ is more than 2× smaller compared to the double layer regime (Table 1).

The charge-induced resistance variation of the np-Au sample (II) with the initial adsorbed oxygen layer is shown in Fig. 11.4. Upon cycling in the positive voltage regime (A, Fig. 11.4), where the initial adsorbed oxygen layer is stable [24], the resistance changes reversibly between a lower value at $U_{charging} = +300$ mV and a higher value at $U_{charging} = +600$ mV corresponding to a charge coefficient $(\Delta R/R)/\Delta Q = 1.4 \times 10^{-2}$ g/C. Removing the oxygen layer by a cathodic sweep from $U_{charging} = +300$ mV to -400 mV gives rise to an irreversible decrease of R by a factor of ca. 1.8. Subsequent cycling in the double layer regime (B, Fig. 11.4) is associated with a slightly larger resistance variation ($(\Delta R/R)/\Delta Q = 2.0 \times 10^{-2}$ g/C, Table 1) as compared to the initial state. Extending the voltage regime from -400 mV/+100 mV to -400 mV/+600 mV into the chemical regime where specific adsorption and desorption of negative ions occurs, the resistance variation substantially increases ($\Delta R/R = 19\%$). Similar to the pure sample (I), however, the charge coefficient $(\Delta R/R)/\Delta Q = 0.6 \times 10^{-2}$ g/C in the regime of specific adsorption and desorption is significantly smaller as compared to the double layer regime (Table 1).

It is worthwhile to mention that upon removal of the oxygen layer, the resistance slightly drifts with time upon consecutive cycling (part B and C, Fig. 11.4) which may indicate some structural reordering on a longer time scale after desorption of oxygen. Prior to the removal of oxygen (part A, Fig. 11.4), no significant drift of the resistance occurs. The

same pertains to sample I indicating that in those cases a quasi-stationary state without structural reordering prevails.

11.2. Discussion

The present measurements on nanoporous Au in dependence of charging in an electrolyte reveal as a major result that the resistance can be varied in the several percentage range or by up to 43% upon charging in the double layer or chemical regime, respectively. The charge coefficient $(\Delta R/R)/\Delta Q$ in double layer regime is $2.4 - 3.3\times$ higher than in the regime of specific adsorption (Table 1).

At first, the resistance variation in the double layer regime will be addressed. The presently observed charge-induced resistance change in the double layer regime fits quite well to that observed by Mishra *et al.* [12] recently on np-Au (compare charge coefficients in Table 1). For discussion of the resistance variation, we start from the free electron model of conductivity [75]

$$\sigma = \frac{e^2 n \tau}{m}\,, \tag{11.1}$$

where e, m, n, and τ^{-1} denotes the electron charge, the electron mass, the charge carrier density and the scattering rate, respectively. Charging may affect the resistance in different ways, namely by variation of (i) the charge density, (ii) the volume, or (iii) the scattering rate. As we will see in the following, the observed resistance variation has mainly to be attributed to a change of the scattering probability.

(i) From the maximum variation of the net charge of $\Delta Q = 1.7$ C/g due to double layer formation in the regime $U_{charging} = -500$ to -100 mV, a volume averaged charge variation of $\Delta n/n = 3.5 \times 10^{-4}$ is estimated taking into account the free charge carrier density $n = 5.9 \times 10^{28}\,\mathrm{m}^{-3}$ of bulk crystalline Au. This value $\Delta n/n$ is by two orders magnitude lower than $\Delta R/R$ and, therefore, by far cannot account for the present charge-induced effect. This notion also holds for the actual situation that the imposed excess charge, arising from double-layer formation, is concentrated at the nanostructure−electrolyte interface rather than being uniformly distributed in the nanostructure. This follows by describing the interconnected porous network as a cylindrical nanostructure for which the cylindrical surface shell with a modified carrier density and the cylindrical core act as parallel conduction paths.

(ii) Next, we will consider the influence of a charge-induced variation of the volume on

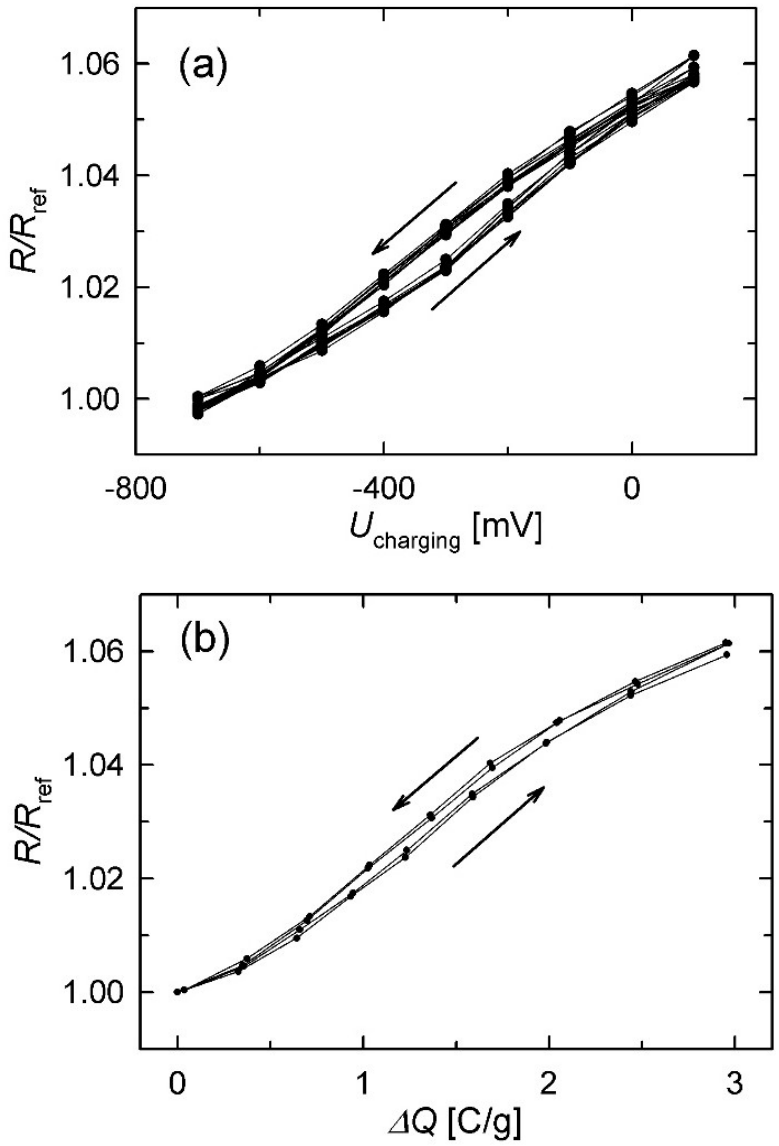

Figure 11.1.: Variation of resistance R of nanoporous Au (sample I) with (a) voltage $U_{charging}$ used for charging and with (b) corresponding imposed charge ΔQ during consecutive chrono-amperometric cycles between $U_{charging} = -700$ mV and $+100$ mV. ΔQ is obtained by integration the charging current; ΔQ and the reference value R_{ref} of the resistance refer to $U_{charging} = -700$ mV. The charge coefficient $(\Delta R/R)/\Delta\sigma$ given in Table 1 is obtained from the linear portion of the curve which corresponds to the double layer regime between -500 mV and -100 mV (cf. Fig. 11.2). $U_{charging}$ measured with respect to Ag/AgCl reference electrode [39, 40].

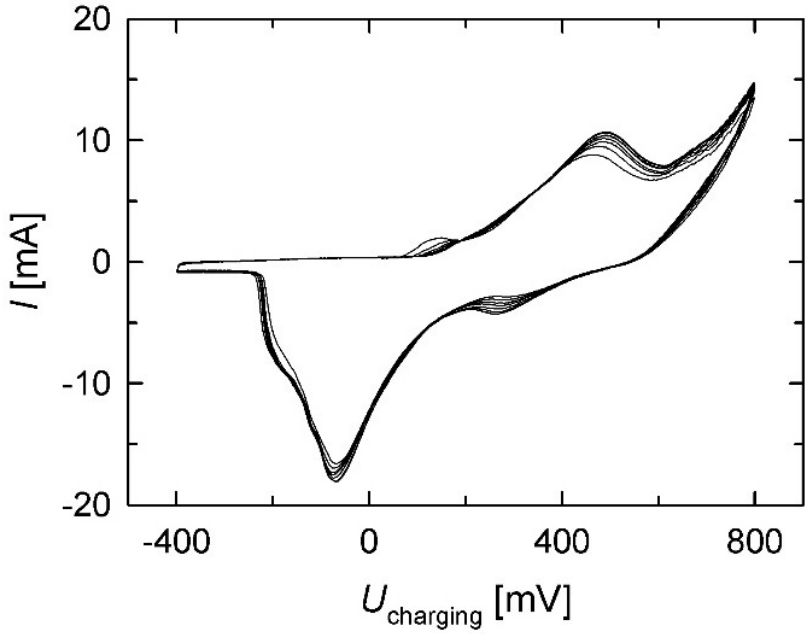

Figure 11.2.: Charging current I versus charging voltage $U_{charging}$ during sucessive 8 cycles at 1 mV/s of sample I (cyclovoltammogram). $U_{charging}$ measured with respect to Ag/AgCl reference electrode. Peaks above $U_{charging} = +100$ mV (anodic direction) and at $U_{charging} = -100$ mV (cathodic direction) indicate specific adsorption of oxygen species and desorption, respectively. Double layer regime between -500 mV and -100 mV [39, 40].

the electrical conductivity. Charging experiments on nanoporous pure Au revealed a reversible expansion $\Delta l/l = 0.4 \times 10^{-4}$ upon positive charging up to $\Delta Q = 0.8$ C/g [24]. Taking into account the bulk modulus $K = 173$ GPa and the pressure coefficient $(\Delta R/R)/p = -3 \times 10^{-6}$ bar^{-1} of the resistance of Au [76], this charge-induced volume expansion corresponds to a relative increase $\Delta R/R$ of the resistance of 6×10^{-4}. Therefore, also the charge-induced volume change cannot account for the observed value $\Delta R/R$ which is two orders of magnitude larger. This negligible effect of the volume on the resistance is further supported by another comparison. Although the charged-induced volume changes in the regimes of double layer charging and specific adsorption/desorption are almost identical [77], the relative resistance variations with respect to imposed charge are quite different in these regimes (see $(\Delta R/R)/\Delta\sigma$, Table 1).

(iii) Since the charging effect on the charge-carrier density and the volume obviously cannot account for the observed resistance variation, one has to conclude that the observed charge-induced variation of the resistance predominantly arises from variations of the scattering probability τ^{-1} with charging. In fact, charge carrier scattering at the crystal-electrolyte interfaces is the dominating factor of the electrical resistance of the nanoporous

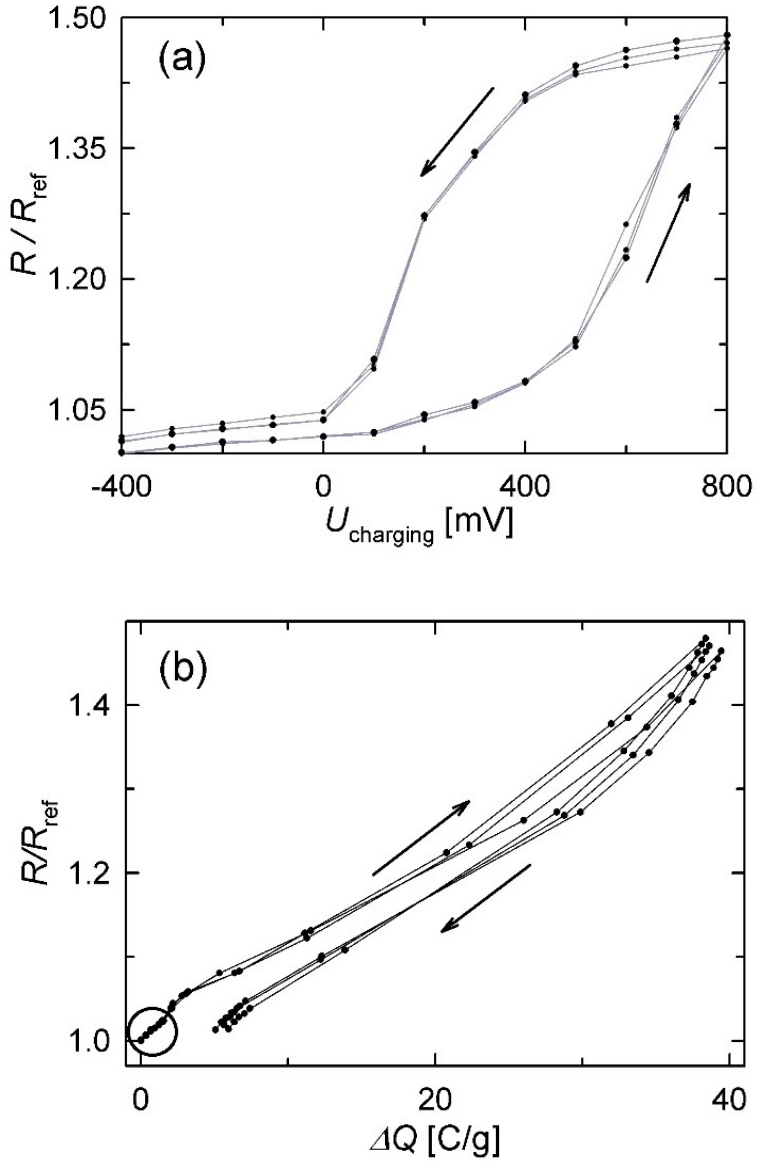

Figure 11.3.: Variation of resistance R of nanoporous Au (sample I) with (a) voltage $U_{charging}$ used for charging and with (b) corresponding imposed charge ΔQ during consecutive chrono-amperometric cycles between $U_{charging} = -400$ mV and $+800$ mV which includes the regime of chemical adsorption and desorption (cf. Fig. 11.2). The encircled range in part (b) represents the double layer regime. ΔQ is obtained by integration of the charging current; ΔQ and the reference value R_{ref} of the resistance refer to $U_{charging} = -400$ mV. The charge coefficient $(\Delta R/R)/\Delta\sigma$ given in Table 1 is obtained from the entire regime between -400 mV and $+800$ mV. $U_{charging}$ measured with respect to Ag/AgCl reference electrode [39, 40].

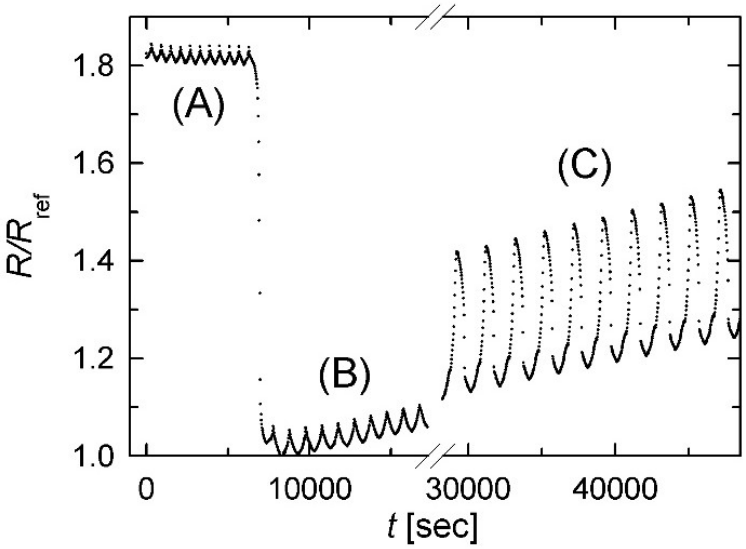

Figure 11.4.: Variation of resistance R of nanoporous Au (sample II) with time t upon reversible cycling between (A) $U_{charging}$ = +300 mV and +600 mV, (B) −400 mV and +100 mV, and (C) −400 mV and +600mV. The cycling regimes correspond to (A) the state with the initial as-prepared oxygen adsorbed layer and (B) the double layer or (C) chemical adsorption and desorption after irreversible removal of the initial adsorbed layer. The charge coefficients $(\Delta R/R)/\Delta\sigma$ of the three regimes are given in Table 1. R_{ref} denotes the minimum resistance in the double layer regime. $U_{charging}$ measured with respect to Ag/AgCl reference electrode [39, 40].

structure. This is the case because the ligament size of about 20 nm, i.e., the structural dimension of nanoporous Au is of similar size or even smaller than the mean free path of electrons. Indeed, the mean free path l of conduction electrons in crystalline Au at ambient temperature is in the range of 40 nm as derived from eq. (11.1) with the conductivity $\sigma = 4.55 \times 10^5$ $(\Omega\text{cm})^{-1}$, the charge carrier concentration $n = 5.9 \times 10^{28}$ m^{-3}, and the Fermi velocity $v_F = l/\tau = 1.39 \times 10^8$ cm/s of Au (data taken from [22]). The interpretation of the present results in terms of changes of the electron scattering probability at the crystal-electrolyte interfaces is in line with that given by Tucceri and Posadas [78] for the charge-depedence of the resistance of Ag films. According to these authors positive charging of the surface gives rise to localized scattering centres at the metal surface due to screening effects which leads to an increase of the resistance. This notion of charge-dependent interface scattering is also supported by recent *ab-initio* studies according to which an outward or inward relaxation of the top layer of the surface atoms of Au occurs in response to negative or positive charging the surface, respectively [79].

The theoretically predicted charge-induced relaxation of the surface [79], on the other hand, raises the question whether a variation of the thickness with charging associated with this relaxation may affect the resistance. In fact, merely because of a charge-induced thickness increase or decrease, the probability of charge scattering at the crystal-electrolyte interface is expected to decrease or increase, respectively. However, this effect should scale with the ratio of the charge-induced relaxation and the structure size. For a charged-induced relaxation well below 0.1 nm [79] and a structural size in the range of 20 nm this ratio is at least one order of magnitude smaller than the observed relative resistance variation and, therefore, cannot account for the observed resistance variation. This conclusion regarding the effect of relaxation is fully consistent with that of the pressure effect discussed in paragraph (ii).

The interpretation in terms of charge-dependent scattering at the crystal-electrolyte interfaces is further supported by comparing the present results with corresponding measurements on particle-assembled nanocrystalline metals and on thin films. The charge coefficient in the double layer regime of the nanoporous sample is up to more than 7× larger than that in cluster-assembled porous nanocrystalline Pt [11] (Table 1) . This shows that in particle-assembled nanocrystalline Pt the influence of charge-dependent scattering at electrolyte interface is reduced as compared to porous Au due to strong scattering at particle-particle grain boundary interfaces [11]. On the other hand, the charge coefficient

of np-Au is also up to 3× larger than that in Au film with a thickness of 7 nm (Table 1) [80] and even much larger than that in Ag films [78]. This indicates that the scattering at the electrolyte interface in the nanoporous sample is stronger than in thin films as expected because of the more complex ligament structure compared to a plane surface−electrolyte interface of a film. A more quantitative description of the electrical transport properties should take into account this complex morphology which for instance can be numerically simulated on the basis of finite element methods [81].

Finally, the resistance variation of nanoporous Au in the regime of specific adsorption will be discussed. Upon cycling in the voltage-range where specific adsorption or desorption of negative ions occurs, reversible resistance variations between up to 19% and 43% were found in the various nanoporous Au samples (see Figs. 11.3, 11.4 and Table 1). This resistance variation in the chemical regime of the nanoporous samples is of similar size (19%) or even higher (45%) than that observed by Ganon *et al.* [82] upon electrochemical adsorption and desorption of oxygen in Au films with thickness of 25 nm (Table 1). In the latter case, the resistance increase upon positive charging in the chemical regime is ascribed to the reversible processes of adsorption and chemisorption of oxygen species (OH^-, O^{2-}) with the formation of a Au-oxide layer [82]. An increase of the resistance of thin films is also observed for chemisorption of other negative ions [78].

The study of the chemical nature of the chemisorbed layer is beyond the scope of the present work. From the maximum transferred charge of 40 C/g in the chemical regime (Fig. 11.3b) a charge transfer of about two electrons per surface atom can roughly be estimated, assuming a mass-specific surface area of 10 m^2/g of np-Au [24], which corresponds to the formation of about one monolayer of chemisorbed species. Similar as discussed for the double layer regime (see paragraph i), the reduced number of charge carriers associated with one non-conducting chemisorbed monolayer in relation to the total number of charge carriers cannot account for the resistance variations in the range of $19 - 43\,\%$. This supports the notion developed earlier for thin films [78, 82] that the resistance in the chemical regime increases because the atoms of the chemisorbed layer act as scattering centres thus modifying the scattering rate $1/\tau$ [78, 82]. The present result that the charge coefficient $(\Delta R/R)/\Delta\sigma$ in this chemical regime is lower than in the double layer regime (Table 1) also qualitatively agrees with observations on thin films [78].

In conclusion, the present studies showed that the resistance of nanoporous Au can be reversibly tuned by means of charging the surfaces of the porous structure in an electrolyte.

	$(\frac{\Delta R}{R})_{max}$ [%]	$(\frac{\Delta R}{R})/\Delta Q$ [10^{-2} g/C] ([10^{-2} m^2/C])	charging regime	remarks
np-Au, I	0.04	2.2	double layer	Fig. 11.1
	0.43	0.9	specif. adsorpt.	Fig. 11.3
np-Au, II		1.4	(A) initial, with oxide	Fig. 11.4
		2.0	(B) double layer	Fig. 11.4
	0.19	0.6	(C) specif. adsorpt.	Fig. 11.4
np-Au [a]	0.06	3.3	double layer	
nc-Pt [b]	0.08	0.3	double layer	
Au, thin film (7 nm) [c]	0.016	0.7 (5.3)	double layer	
Au, thin film (25 nm) [d]	0.15	1.0 (2)	specif. adsorpt.	

[a] [12]
[b] [11]
[c] [80]
[d] [82]

Table 11.1.: Maximum relative variation $(\Delta R/R)_{max}$ and charge coefficient $(\Delta R/R)/\Delta\sigma$ of the relative resistance variation of nanoporous Au (np) with charging (sample I, II). ΔQ: charge density related to mass [C/g] or surface area [C/m^2] (quoted in brackets). The different charging regimes A, B, C of sample II are shown in Fig. 11.4. Literature values for np-Au, cluster-assembled porous nanocrystalline Pt (nc) and thin Au films are shown for comparison [40].

Reversible variations of the resistance of up to 43% occur due to the formation of a chemisorbed surface layer. Charge-induced modifications of the charge carrier scattering at the solid-electrolyte interface is identified as the dominant effect which causes the resistance variations. The relative resistance variation in nanoporous Au is found to be more pronounced in comparison to both porous cluster-assembled metals and thin films.

CHAPTER 12

Summary

The focus of the present work is on the synthesis, characterization and functionalization of nanoscaled metals and metaloxides. Functionalization is achieved by reversible charging of interfaces. The samples are synthesized in various ways: (i) chemical synthesis, (ii) nanocrystallite condensation under inertgas, and (iii) dealloying. Chemical synthesis by a polyol process enabled gaining FePt-nanoparticles with a crystallite size of 3.4 nm and a very narrow particle size distribution. By means of nanocrystallite condensation in inertgas highly pure nanocrystalline metal powders could be synthesized with a crystallite size of ca. 10 nm. Dealloying yielded a nanoporous foam received from an appropriate bimetallic master alloy where the less noble component was dissolved electrochemically.

Charging was performed in aqueous electrolytes, mainly 1-M KOH. With the help of charging a high surface density of charge carriers could be achieved. Along with the high surface-to-volume ratio of nanoscaled materials, the properties could be tuned reversibly by charging. Cyclovoltammetry was applied as pre-characterization method and by means of chronoamperometry the nanoscaled samples were charged. Nanocrystalline metal powder samples received from nanocrystallite condensation in inertgas (Co, Pd, FePd) were compacted and connected to a potentiostat directly while for metal oxides (maghemite, produced via microwave synthesis) Pt was added to create a chargeable percolating network.

The work aimed at the charge-induced tuning of magnetic moment and conductivity in nanoscaled metals and metal oxides. All magnetometry experiments were performed in a specially designed electrochemical cell which allowed in-situ measurements in SQUID

and simultaneous charging. The resistance measurements were performed in a 4-wire measurement setup where charging of the sample was also performed concurrently with an electrochemical cell built-up in a fume hood.

The nanocrystalline ferromagnetic materials as Co, FePt, and γ-Fe_2O_3 exhibit a decrease of m upon positive charging while an increase of m results from negative charging. For both Co and γ-Fe_2O_3/Pt-composites (1:3 weight-%) the reversible variation of m was assigned to electrochemically induced surface reactions. For Co the effect is small with 0.7 % at 50 Oe as charging is supposed to influence only the low magnetic Co-oxide shell.

In the case of γ-Fe_2O_3/Pt upon electrochemical cycling an Fe-oxide with low and high magnetization in anodic and cathodic direction is formed, respectively. This gives rise to a reversible variation of the magnetic moment up to 10.4 % at 50 kOe. In the pseudocapacitive regime $\Delta m/m_{ref}$ is significantly lower with 0.33 % at 50 Oe. Co and γ-Fe_2O_3/Pt exhibit the same charge coefficient β although the maximum relative variation of the magnetic moment $\Delta m/m_{ref}$ is 15× higher for γ-Fe_2O_3/Pt compared to Co.

FePd-alloys also exhibit a decrease of m upon positive charging and vice versa at fields above 2 kOe. However, for fields at 200 Oe and below the response upon charging is reversed so that positive charging increases the magnetic moment and negative charging decreases it. $\Delta m/m_{ref}$ is maximum at 20 Oe with 1.83 % for $Fe_{50}Pd_{50}$.

Although the relative variation for chemically synthesized FePt is with a maximum of 0.18 % significantly lower compared to other systems, the charge coefficient β exhibits with -9.12×10^{-3} g C^{-1} the highest observed value at 500 Oe. The large β might be assigned to the small crystallite size which is 3× smaller compared to particles from crystallite condensation in inertgas.

The present concept of tuning of magnetization may open up one promising niche path towards the current challenging effect of controlling magnetism by electric fields.

The resistance measurements on nanoporous Au yielded a reversible resistance variation up to 43 % upon electrochemical charging. Nanoporous Au exhibits a charging coefficient in the double layer regime which is 7× larger than that in porous nanocrystalline Pt. This shows that in particle-assembled nanocrystalline Pt the influence of charge-dependent scattering at the electrolyte interface is reduced as compared to nanoporous Au due to strong scattering at particle-particle grain boundary interfaces. The charging coefficient for the resistance is higher in the double layer and the pseudocapacitive

regime than in the regime of specific adsorption and desorption. This is in contrast to the charge-induced variation of the magnetic moment of nanocrystalline samples as the γ-Fe_2O_3/Pt-composite, where the pseudocapacitive regime exhibits a smaller charge-coefficient than in the adsorption/desorption regime. The strong variation of the resistance is attributed to variations of the scattering processes resulting from adsorbing and desorbing electrochemical species on the Au-surface. Comparing the relative variations of resistance and magnetic moment it can be concluded that R is more sensitive to charging than m, since electron-scattering selectively probes metal-electrolyte interfaces which are modified by charging. In contrast to that m represents a volume-averaged value where only the surface-shell part is sensitive to charging.

For future experiments the application of non-aqueous electrolytes and ionic liquids would be fruitful. This would allow operation under non-oxidizing conditions as well as the use of higher charging voltages. The experimental setup for in-situ SQUID-measurements would be significantly improved by introducing a quasi-reference electrode for SQUID-measurements. Chemically synthesized FePt with an improved removing of ligands appears highly attractive for further studies of charge-induced property tuning due to the extremely small crystallite size.

CHAPTER 13

Appendix

13.1. Nanocrystalline Co - supplementary data

This section amends the results presented in 5.2 with the results for 50 Oe, 500 Oe and 50 kOe in Fig. 13.1 - Fig. 13.6. In addition from the m-Q characteristics $\frac{d(m/m_{ref})}{dQ}$ is obtained.

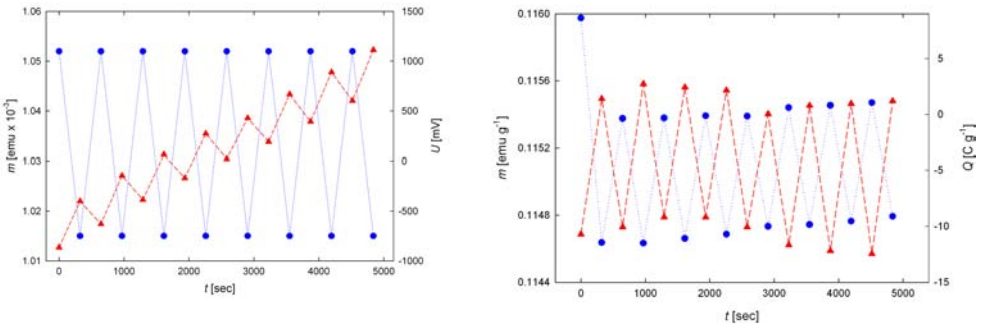

(a) time t vs magnetic moment m and applied charge Q

(b) time t vs magnetic moment m and applied charge Q

Figure 13.1.: Co measured at 50 Oe upon alternating adsorption/desorption

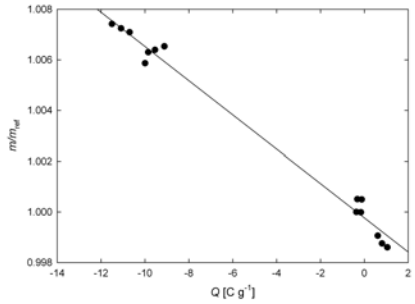

Figure 13.2.: Magnetic moment m of Co in dependence of Q with a linear regression fit for the calculation of $\frac{dm}{dQ}$ at 50 Oe

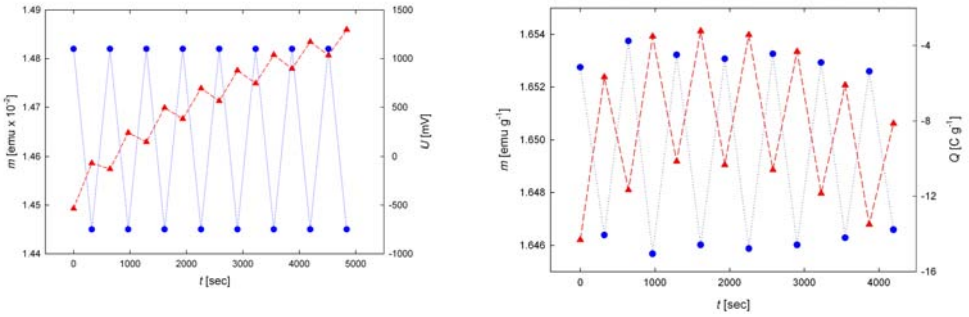

(a) time t vs magnetic moment m and applied charge Q

(b) time t vs magnetic moment m and applied charge Q

Figure 13.3.: Co measured at 500 Oe upon alternating adsorption/desorption

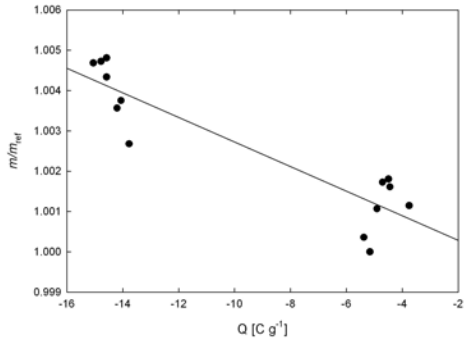

Figure 13.4.: Magnetic moment m of Co in dependence of Q with a linear regression fit for the calculation of $\frac{dm}{dQ}$ at 500 Oe

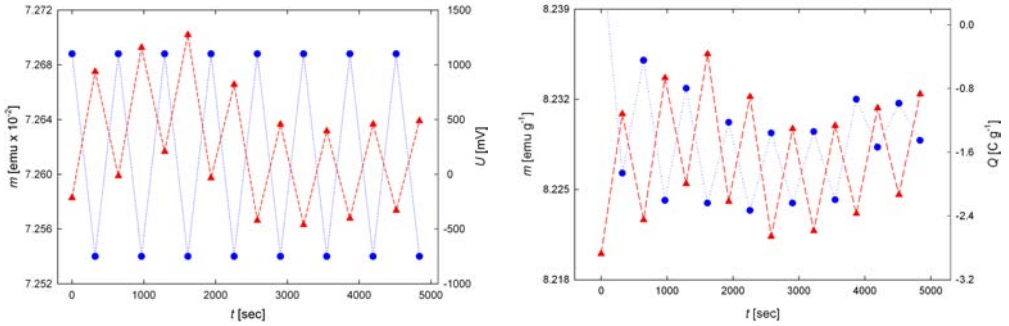

(a) time t vs magnetic moment m per mass and applied charge Q

(b) time t vs magnetic moment m per mass and applied charge Q

Figure 13.5.: Co measured at 50 kOe upon alternating adsorption/desorption

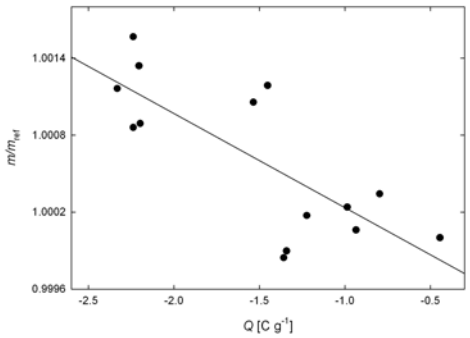

Figure 13.6.: Magnetic moment m of Co in dependence of Q with a linear regression fit for the calculation of $\frac{dm}{dQ}$ at 50 kOe

13.1.1. Influence of charging on coercitivity

In Fig. 13.7 the negative slope of the Co-hysteresis from Fig. 5.5(a) is shown. This is an evidence that indeed H_c is influenced by charging and not only a shift on the x-axis is given.

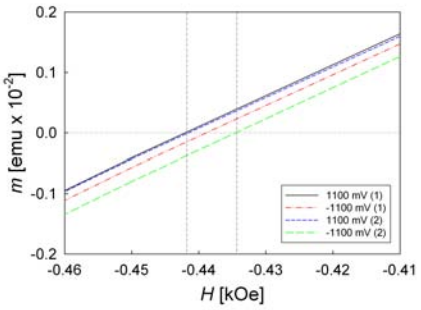

Figure 13.7.: Hysteresis loop of Co at four alternating charging states (negative flank)

13.2. Nanocrystalline Pd - supplementary data

Fig. 13.8 illustrates the U- and Q-dependence of nanocrystalline Pd at 2 kOe.

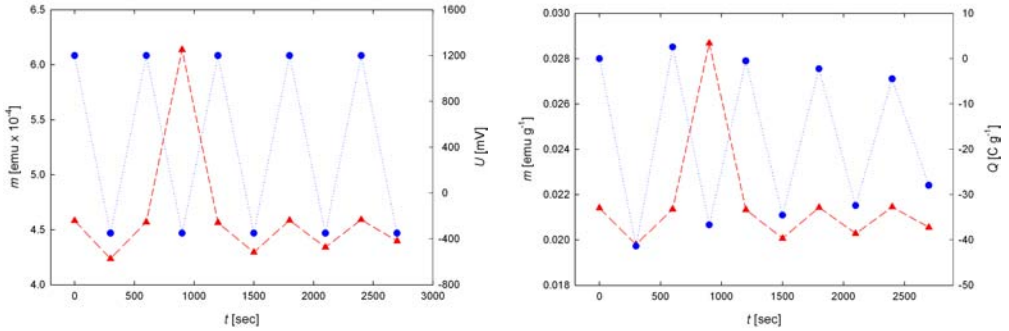

(a) time t vs magnetic moment m and applied charge Q for Pd

(b) time t vs magnetic moment m and applied charge Q for Pd

Figure 13.8.: Magnetic moment m of nanocrystalline Pd measured at 2 kOe upon consecutive adsorption-desorption cycling (a) charging voltage U, (b) imposed charge Q

13.3. Nanocrystalline FePd - supplementary data

13.3.1. $Fe_{20}Pd_{80}$

The supplemental material in this section completes the findings in section 7.2 for the magnetic fields of 20 kOe, 2 kOe and 20 Oe with the respective m-U and m-Q characteristics as well as the determination of $\frac{d(m/m_{ref})}{dQ}$ (Fig. 13.9 - Fig. 13.14).

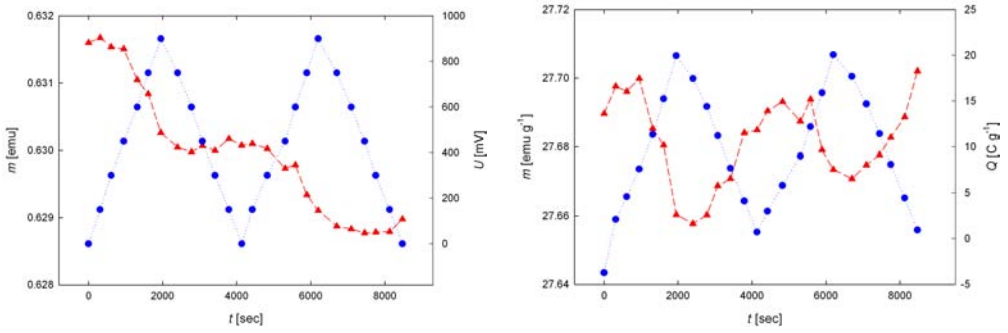

(a) time t vs. m and U (b) time t vs. m and Q

Figure 13.9.: Dependence of magnetic moment m of $Fe_{20}Pd_{80}$ on charging at 20 kOe

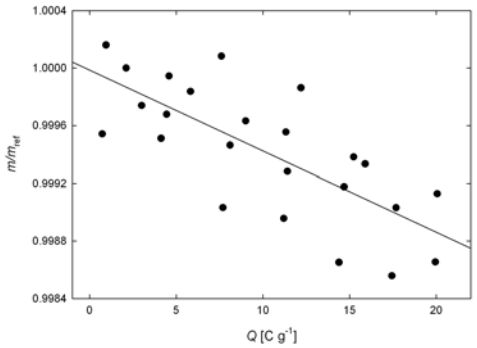

Figure 13.10.: Determination of $\frac{d(m/m_{ref})}{dQ}$ for $Fe_{20}Pd_{80}$ at 20 kOe

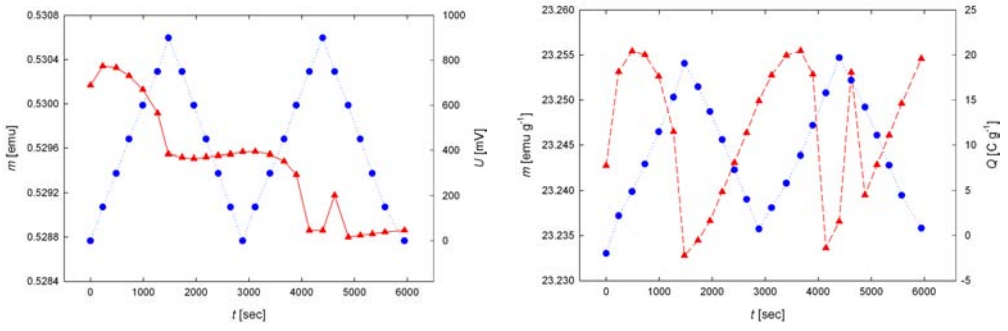

(a) time t vs. m and U (b) time t vs. m and Q

Figure 13.11.: Dependence of magnetic moment m of $Fe_{20}Pd_{80}$ on charging at 2 kOe

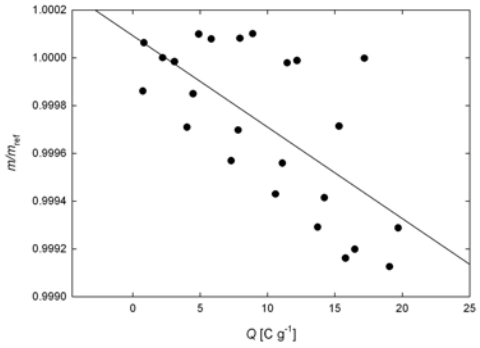

Figure 13.12.: Determination of $\frac{d(m/m_{ref})}{dQ}$ for $Fe_{20}Pd_{80}$ at 2 kOe

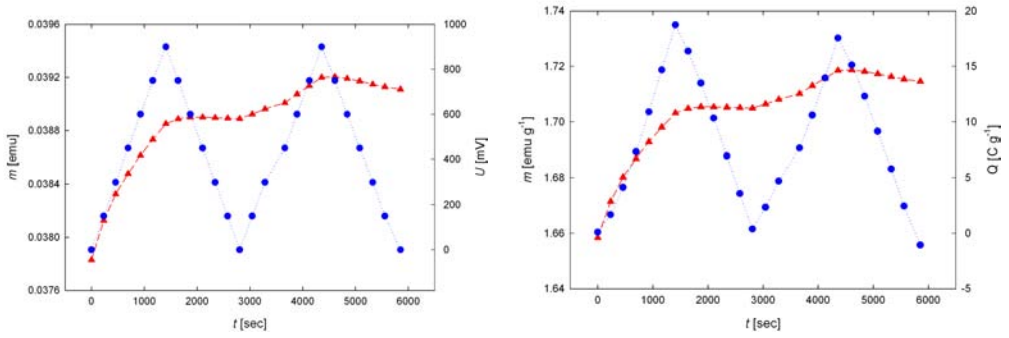

(a) time t vs. m and U

(b) time t vs. m and Q

Figure 13.13.: Dependence of magnetic moment m of $Fe_{20}Pd_{80}$ on charging at 20 Oe

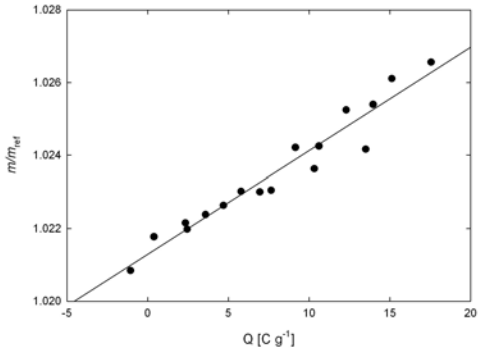

Figure 13.14.: Determination of $\frac{d(m/m_{ref})}{dQ}$ for $Fe_{20}Pd_{80}$ at 20 Oe

13.3.2. $Fe_{50}Pd_{50}$

13.3.2.1. Voltage regime for 2-electrode charging

Tab. 13.1 and 13.2 denote the 2-electrode charging voltage for in-situ charging in SQUID corresponding to the values in 3-electrode geometry

U_{WE-RE} **[mV]**	$U_{WE-CE_{end}}$ **[mV]**
0	230
+100	+614
+200	+832
+300	+1189
+400	(>)+1500

Table 13.1.: $Fe_{50}Pd_{50}$ CA precharacterization for in-situ charging in SQUID on 21.07.2009

U_{WE-RE} **[mV]**	$U_{WE-CE_{end}}$ **[mV]**
0	+290
+100	+200
+200	+1137
+300	+1460
+400	+1618
-600	-750

Table 13.2.: $Fe_{50}Pd_{50}$ CA precharacterization for in-situ charging in SQUID on 12.11.2009

13.3.2.2. In-situ charging in SQUID

Section 13.3.2.2 completes the measuring results in section 7.3 with the data for 20 Oe and 20 kOe. In Fig. 13.15 the dependence of the magnetic moment m on the charging voltage U/the charge Q is visualized for the 'virgin' measurement series.

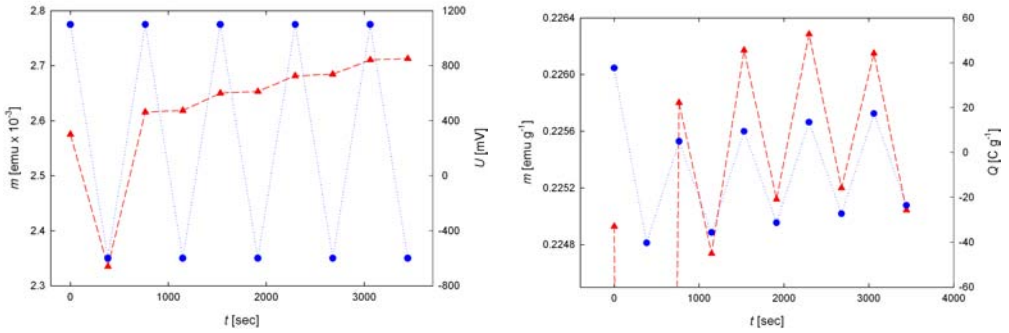

(a) t vs. m and vs. U (b) t vs. m and vs. Q

Figure 13.15.: Dependence of the magnetic moment m upon charging voltage U/charge Q at 20 Oe for $Fe_{50}Pd_{50}$

The extremely high value for the second m measuring point is an artifact and can be assigned to a bad regression fit during the SQUID measurements. Positive charging in the oxygen adsorption regime leads to an increase of the magnetic moment m while negative charging or rather electrochemically induced oxygen desorption causes a decrease of the magnetic moment m. The linear regression fit in Fig. 13.16 yields the charge coefficient $\frac{d(m/m_{ref})}{dQ} = 1.17{\times}10^{-4}$ g C^{-1} with a positive sign at 20 Oe.

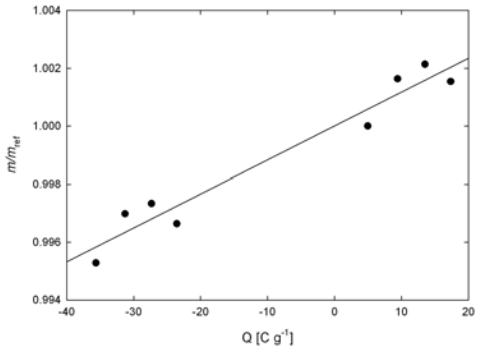

Figure 13.16.: Charge-dependence of the relative magnetic moment m/m_{ref} with the determination of the $\frac{d(m/m_{ref})}{dQ}$ by linear regression fit for $Fe_{50}Pd_{50}$ at 20 Oe. m_{ref} denotes the first measured m data point.

Applying a magnetic field $H_{appl} = 2$ kOe leads to a trend reversal which was already observed for $Fe_{20}Pd_{80}$. As a consequence in Fig. 13.17 positive charging leads to a decrease of m while negative charging yields an increase of m.

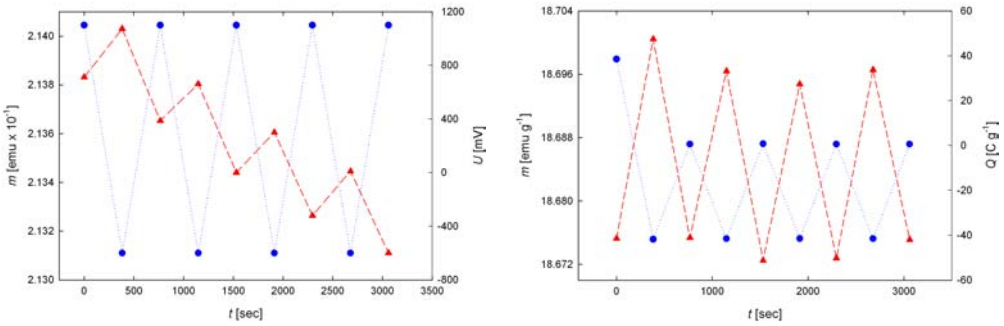

(a) t vs. m and vs. U (b) t vs. m and vs. Q

Figure 13.17.: Depedence of the magnetic moment m upon charging voltage U/charge Q at 2 kOe for $Fe_{50}Pd_{50}$

Linear regression in Fig. 13.18 yields the charge coefficient $\frac{d(m/m_{ref})}{dQ}$ with -2.7910^{-5} g C^{-1}.

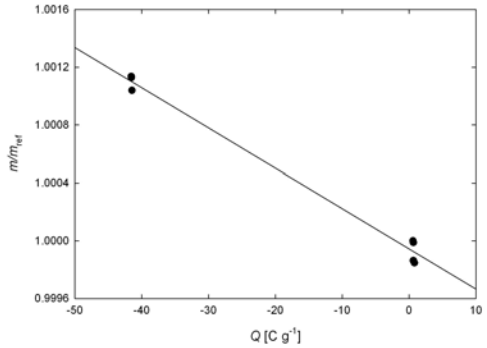

Figure 13.18.: Charge-dependence of the relative magnetic moment m/m_{ref} with the determination of the $\frac{d(m/m_{ref})}{dQ}$ by linear regression fit for $Fe_{50}Pd_{50}$ at 2 kOe. m_{ref} denotes the first measured m data point.

Fig. 13.19 - 13.22 show the U and Q characteristics for the measuring sequence denoted as 'highres'. Fig. 13.19 presents the results for 20 Oe with only one charging cycle but with $\Delta U = 300$ mV in anodic and cathodic direction, respectively. The 7^{th} measuring point can be explained by a bad regression fit by SQUID and must not be considered as an effect. The rest of the plot does not show a change aside from the slight increase at the beginning of the measurements. The only admissible interpretation is a slight 'kink' upon reversing the applied charging voltage in Fig. 13.19(a). This might be a bit more pronounced in Fig. 13.19(b) after the drift correction for m and Q but it must be emphasized here that

this argumentation does not have a very solid base.

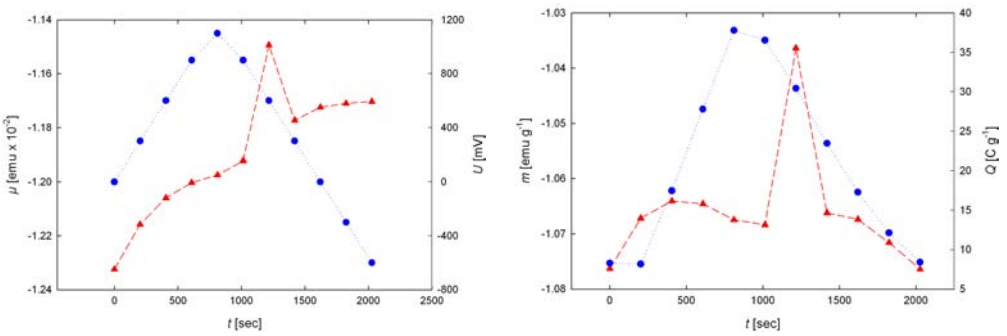

(a) t vs. m and vs. U (b) t vs. m and vs. Q

Figure 13.19.: Depedence of the magnetic moment m upon charging voltage U/charge Q at 20 Oe for $Fe_{50}Pd_{50}$- higher resolution

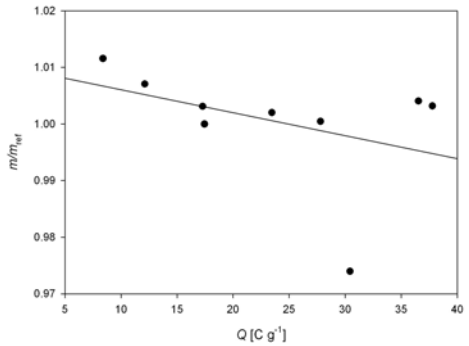

Figure 13.20.: Charge-dependence of the relative magnetic moment m/m_{ref} with the determination of the $\frac{d(m/m_{ref})}{dQ}$ by linear regression fit for $Fe_{50}Pd_{50}$ at 20 Oe - high resolution. m_{ref} denotes the first measured m data point.

Therefore a conclusive interpretation of Fig. 13.20 cannot be given. The slight downward trend of the linear regression fit seems not to be trustworthy in this context, as from earlier measurements on FePd-systems an increase of the slope is expected (→ see for example Fig. 13.15).

Adjusting the applied magnetic field H_{appl} to 2 kOe induces a sign change for the variation of m which means that from $H_{appl} = 2$ kOe upwards positive charging decreases m and vice versa.

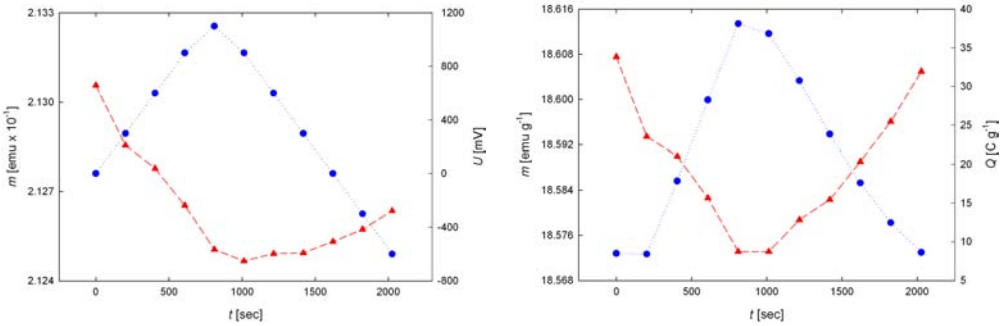

(a) t vs. m and vs. U (b) t vs. m and vs. Q

Figure 13.21.: Depedence of the magnetic moment m upon charging voltage U/charge Q at 2 kOe for $Fe_{50}Pd_{50}$- higher resolution

This goes along with a negative slope for the $\frac{d(m/m_{ref})}{dQ}$ derived from Fig. 13.22.

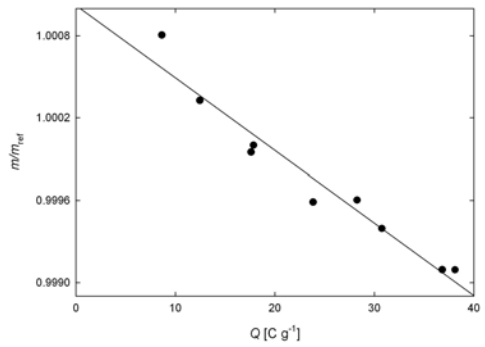

Figure 13.22.: Charge-dependence of the relative magnetic moment m/m_{ref} with the determination of the $\frac{d(m/m_{ref})}{dQ}$ by linear regression fit for $Fe_{50}Pd_{50}$ at 2 kOe - high resolution. m_{ref} denotes the first measured m data point.

13.4. Nanocrystalline FePt - supplementary data

In this section the synthesis route for $FePt_{ol}$ and additional measuring curves related to the in-situ charging experiments are presented.

13.4.1. Basic chemical synthesis route of FePt

The measurement setup requires a fume hood, as different chemicals have to be handled with care. At first all glass components are flushed with Argon, so that synthesis can be

performed under inertgas atmosphere. At the beginnnig of the synthesis the system remains open nevertheless. 197 mg/0.05 mmol Platinum acetylacetonate ($Pt(acac)_2$, Sigma Aldrich, 99.99% pure) and 390 mg/1.5 mmol 1,2-Hexadecanediol) (Sigma Aldrich, 98% pure), are mixed in a flask together with 20 ml of Dioctylether (Sigma Aldrich, ≥99% pure). This yields a cloudy yellow liquid which is frequently stirred under moderate heating via heating mantle. After reaching ≈ 110 °C , the liquid turns transparent which indicates that the components are diluted. Temperature measurements were taken between flask and heating mantle, as synthesis is done under sealed Argon atmosphere making it impossible to place the thermal element in the liquid. Careful Argon-flushing prevents the setup from water evaporation. At a temperature of 110 °C 0.13 ml/1 mmol $Fe(CO)_5$ (Acros, 99.5% pure) is injected into the solution along with 0.16 ml/0.5 mmol oleic acid (Sigma Aldrich, ≥99% pure) and 0.17 ml/0.5 mmol oleylamine (Fluka, ≥70% pure). As $Fe(CO)_5$ is stored in the refridgerator, it has to be warmed shortly before the start of the synthesis so that handling with an injection is possible. After injection the liquid turns cloudy again. The experimental setup is now completely sealed and set under a small Argon flow which is regulated via bubbler (≈1 bubble per second). The solution was now heated up under subsequent stirring up to ≈ 300 °C . Between 250°C and 300°C one can observe a colour change from cloudy yellow to black which is a good indicator for the reaction taking place in the flask

A water-supplied cooler enables reflux cooling of the solution so that evaporation through the bubbler is prevented. After having reached 300 °C (heating up phase lasts for ≈20 min) the solution is left for cooling down to room temperature. Upon reaching room temperature, the Argon sealing could be opened to the environment.

The synthesis step is finished at this point, only washing cycles for removing unsolved precipitation have to follow.

For triggering precipitation of the synthesized material 40 ml ethanol (technical quality, dewatered and purified) is filled into the flask with the synthesis product. This black product is then decanted into suitable tubes for centrifugation (Schott, Duran, 45ml, Gl 25, pointed base). It is recommendable not to decant the whole synthesis as centrifugation with a completely filled tube turns out to be difficult. As a counter balance is needed one has to fill a similar centrifugation tube with water of the same weight to start the centrifugation process (centrifuge: Hermle Z300). The precipitate is then centrifuged with 3000-4500 rpm for 5-15 min, depending on the filling level of the centrifugation

tube. Having finished centrifugation, the yellow-brown supernatant is discarded and the remaining black precipitate is dispersed in 20 ml n-hexane (technical quality, dewatered and purified). The excess liquid should be completely transparent to avoid loosing too many of the synthesized particles. 0.05 ml oleic acid and 0.05 ml oleylamine are added to the dispersion. A second washing cycle is performed then by triggering precipitation again with 20 ml ethanol and anew centrifugation. Again the precipitate is dispersed in 25 ml n-hexane and stored under Argon atmosphere. For the first production charges a rubber seal was in use to enable penetration by injection for removing the dispersion without breaking the Argon sealing. This is not in use any longer because n-hexane could penetrate through this rubber sealing. Therefore a normal screw cap is in use and after extraction of the dispersed ligand-coated FePt particles, the filling is flushed with Argon and sealed. The samples received from this synthesis shall be called 'FePt_oleic_stock' for the following discussions. All experiments base on the synthesis route from Sun et al. with the molar ratio of the precursors given above are supposed to yield a composition of 52 % Fe and 48 % Pt.

13.4.2. Ligand exchange

The removal of oleic acid and oleylamine from the FePt-surface can be done with defined washing cycles. In this work we pursue an aproach after the PhD-thesis of Oliver Muth [18]. Ligand exchange leads to a variation of the interparticle distance and possibly influences the magnetic properties. The first approach aimed at the replacement of oleic acid/oleylamine by octanoic acid (Fluka, puriss. p.a.) and octylamine (Fluka, puriss. p.a.) 3 ml of the stock solution are taken as basis for the ligand exchange. The stock solution is precipitated with 10 ml of ethanol and centrifuged. The resulting precipitate is then dispersed in 3 ml n-hexane which is mixed with 0.2 mol/l octanoic acid/octylamine while the ethanol/n-hexane excess is decanted. This dispersion is treated in an ultrasonic bath for 1 h. After this treatment the particles are precipitated again with 10 ml ethanol and dispersed in a solution of 3 ml n-hexane and octanoic acid (6×10^{-3} mol l^{-1}) as well as octylamine (6×10^{-3} mol l^{-1}). Repeating the procedure for 6 times yields a transition from $FePt_{ol}$ to $FePt_{oct}$ as can be seen above in the measurements.

In the same way as described before one can choose other ligands for the ligand exchange procedure. In our case $FePt_{hex}$ was chosen as further system. For the exchange procedure one can exactly follow the procedure described above, one only has to correct the amount

for hexanoic acid (Fluka, puriss. p.a.) and hexylamine (Fluka, puriss. p.a.). As it was easier to realize in the experiment the concentration of 6×10^{-3} mol l^{-1} hexanoic acid/hexylamine in n-hexane was achieved by diluting the solution with a concentration of 0.2 mol l^{-1}.

13.4.3. Ligand removal by utilisation of forming gas

For removing the ligands of $FePt_{ol}$ an additional approach is performed by applying forming gas. The aim is to remove the ligands upon thermal treatment. For that purpose 50 mg $FePt_{ol}$ was dropped on a Si-substrate and placed inside a vacuum oven with two valves attached to it. Considering a fraction of 0.18 mmol oleic acid compared to 53.5 mmol H_2 (12 l minican) it is clear that subsequent flushing provides sufficient hydrogen for reduction. One valve is connected to the vacuum pump then, the other valve is connected to a manometer and a minican filled with forming gas H_2 (Linde; 10% H_2). First the glass tube of the oven is evacuated, then the valve towards the pump is closed and the glass tube is flushed with forming gas. The glass tube is then heated up to 600 °C and frequently flushed with forming gas. After $\approx$ 1 h the glass tube is evacuated and cooled down to room temperature. After ventilation with air the forming gas treated sample is removed. The recovery here turns out to be difficutlt, as the $FePt_{ol}$ still sticks well to the substrate. Charging experiments led to the conclusion that ligand removal was not or only in small parts successful. Another problem to consider is that upon the thermal treatment a phase transition as well as a particle size enlargement are suspected to take place.

13.4.4. Charging of chemically synthesized FePt

Results at $H_{appl} = 50$ Oe are not presented as they could not be evaluated due to the extremely small variation of the magnetic moment $\Delta m = 5.22\times10^{-8}$ emu. Such a small variation does not allow any conclusions related to the influence of charging on the sample. At $H_{appl} = 500$ Oe an evaluation of the variation of the magnetic moment Δm becomes detectable. Additionally this variation is at the same order of magnitude as the possible influence of the Au-coil used for contacting the sample (see also discussion above). The fith data point is not given here as this large variation can only be reasonably explained by a faulty SQUID scan which occured during the automized sequence. In the diagrams shown over time in the following • in blue with dotted line denotes the charging voltage

U/the charge Q while ▲ in red with short dash denotes the magnetic moment m. The errorbars denote the possible influence of a Au-coil on the variation of m as discussed in 10.3.

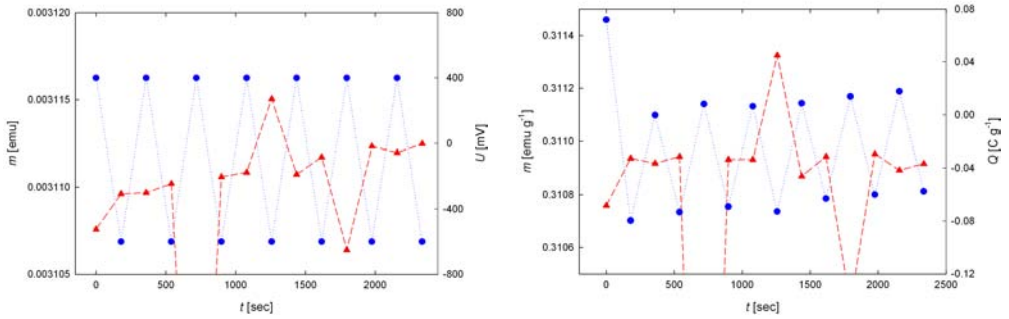

(a) t vs. m vs. U (b) t vs. m vs. Q

Figure 13.23.: Dependence of chemically synthesized FePt in dependence of charging at a magnetic field of 500 Oe

The determination of the $\frac{d(m/m_{ref})}{dQ}$ yields -9.12×10^{-3} g C^{-1} from Fig. 13.24. For both magnetic moment m and charge Q a linear correction of the superimposed drift is performed. The data points 1, 4 and 5 for m have been discarded.

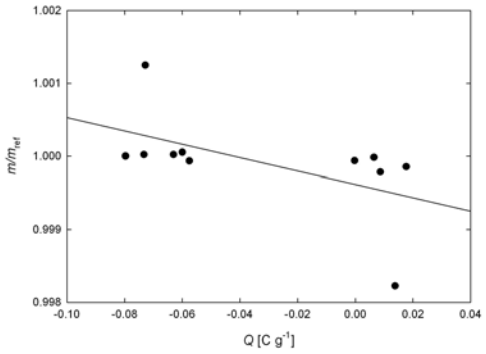

Figure 13.24.: $\frac{d(m/m_{ref})}{dQ}$ determination for chemically synthesized FePt at 500 Oe

For H_{appl} = 50 kOe an interpretation of the results in Fig. 13.25 becomes more difficult. The effect of charging on m is not so pronounced compared to 5 kOe. Nevertheless the data allow an interpretation in a way that positive charging also here leads to a decrease of m although a higher influence of noise has to be borne in mind here.

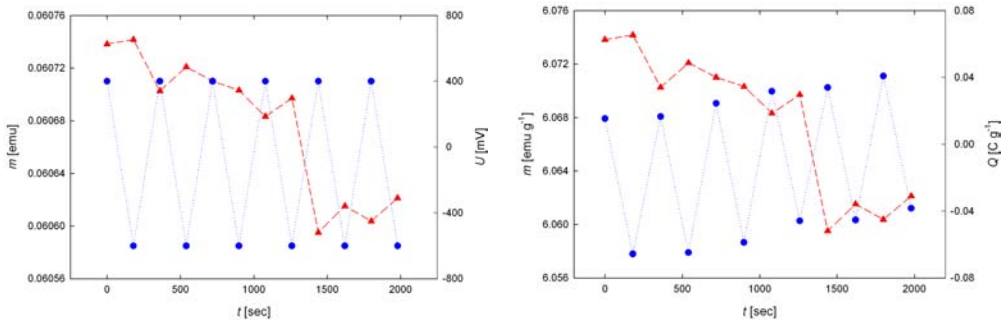

(a) t vs. m vs. U (b) t vs. m vs. Q

Figure 13.25.: Dependence of chemically synthesized FePt in dependence of charging at a magnetic field of 50 kOe

Linear regression is still possible for a determination of the $\frac{d(m/m_{ref})}{dQ}$ but the correlation coefficient r^2 is rather low with a value of 0.27 so that the absolute value of $\frac{dm}{dQ}$ = -4.73×10^{-3} g C^{-1} is questionable. Nonetheless for the $\frac{d(m/m_{ref})}{dQ}$ at 50 kOe a negative slope is given which is depicted in Fig. 13.26.

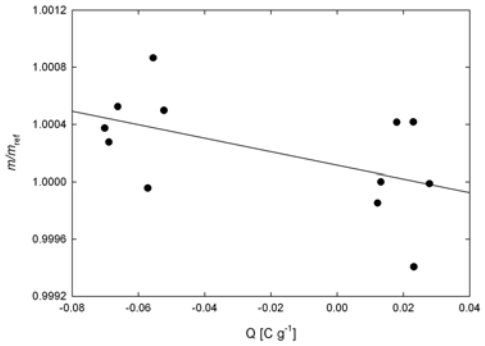

Figure 13.26.: $\frac{d(m/m_{ref})}{dQ}$ determination for chemically synthesized FePt at 50 kOe

13.5. Effect of charging current - supplementary data

For the determination of A it is a good ansatz for all samples to choose an ellipse with a = 1.5 mm and b = 0.25 mm as the pellets have a diameter of slightly less than 3 mm and a thickness of ≈0.5 mm. This yields with $A = ab\pi$ for the Au-coil A = 1×10^{-6} m^2. n is estimated with 10; for a stable rather non-brittle pellet the number of windings is less. $I_{leak,max}$ is the leakage current taken from the evaluation of the chronoamperometry

curves. It is important to mention that this magnetic moment is field-independent; that means that with increasing magnetic field the relative influence on the variation of m originating from the Au-coil becomes smaller and smaller. The more leakage current a sample exhibits the more the influence by the coil on the magnetic moment variation has to be considered. The possible influence of the calculation from Eq. 10.1 is maximized by choosing $n = 10$ and the maximum determined leakage current as $I_{leak,max}$ for every single measurement sequence, respectively.

Acknowledgements

Good scientific work can never be done alone - this doctoral thesis is no exception. There are many people I have to give thanks:

Univ.-Prof. Dr. Roland Würschum, TU Graz for the support and the supervision of my work as well as the fruitful discussions

Univ.-Prof. Dr. Heinz Krenn, KFU Graz for providing the possibility for doing SQUID magnetometry as well as the fruitful discussions in the field of magnetometry

Univ.-Prof. Dr. Hans-Eckhardt Schaefer for kindly acting as external reviewer

Ao. Univ.-Prof. Dr. Stephan Landgraf, TU Graz for the support in the fields of chemical synthesis and electrochemistry

DI Stefan Topolovec, TU Graz for the fruitful collaboration and the 'tuning' of maghemite as well as the valuable discussions and the help with latex-writing

DI Patrick Wahl, formerly TU Graz for the valuable data on nanoporous Au, the fruitful discussions and the extremely useful Matlab-program for chronoamperometry

DI Maximilian Besenhard, formerly TU Graz for the fruitful discussions in the field of electrochemistry

Dr. Kashif Nadeem, KFU Graz for the help with SQUID-magnetometry and the fruitful discussions

Hilde Freißmuth, TU Graz for the valuable help concerning the synthesis of FePt

DI Peter Parz, TU Graz for the collaboration and the fruitful discussions concerning electrochemistry and materials science

Dr. Dorothée Vinga Szabó, Karlsruhe Institute of Technology for the support with

maghemite and TEM-pictures

Dr. Hai-Jun Jin and Univ.-Prof. Dr. Jörg Weißmüller, formerly Karlsruhe for the support with AgAu- and PtCu-masteralloys as well as nanoporous Au and fruitful discussions

Dr. Karin Wewerka and Dr. Ilse Letofsky-Papst, TU Graz for the nice FePt-TEM pictures

The whole staff of the Institute of Materials Physics, TU Graz for the support in the last years

My Parents, Ewald and Brigitte Traußnig: Thanks a lot for the support over all the years during my studies and for teaching me so many important thinks beside physics

Financial support by the Austrian Science Fund (FWF) (project S10405-N16) and by NAWI Graz (Graz Advanced School of Science) is appreciated

Bibliography

[1] Krenn, H. and Granitzer, P. *Physik in unserer Zeit* **33**, 218 (2002).

[2] Weissmüller, J., Viswanath, R. N., Kramer, D., Zimmer, P., Würschum, R., and Gleiter, H. *Science* **300**, 312 (2003).

[3] Eerenstein, W., Mathur, N. D., and Scott, J. F. *Nature* **442**, 759 (2006).

[4] Ziese, M. and Thornton, M. J. *Spin electronics*. Springer, Heidelberg, (2001).

[5] Chu, Y., Martin, L. W., Holcomb, M. B., Gajek, M., Han, S., He, Q., Balke, N., Yang, C., Lee, D., Hu, W., Zhan, Q., Yang, P., Fraile-Rodriguez, A., Scholl, A., Wang, S. X., and Ramesh, R. *Nature Materials* **7**, 478 (2008).

[6] Kleemann, W. *Physics* **2**, 105 (2009).

[7] Mikami, R., Taguchi, M., Yamada, K., Suzuki, K., Sato, O., and Einaga, Y. *Angewandte Chemie International Edition* **43**, 6135 (2004).

[8] Sun, S., Murray, C. B., Weller, D., Folks, L., and Moser, A. *Science* **287**, 1989 (2000).

[9] Sun, S. *Advanced Materials* **18**, 393 (2006).

[10] Gleiter, H., Weissmüller, J., Wollersheim, O., and Würschum, R. *Acta Materialia* **49**, 737 (2001).

[11] Sagmeister, M., Brossmann, U., Landgraf, S., and Würschum, R. *Physical Review Letters* **96**, 156601 (2006).

[12] Mishra, A. K., Bansal, C., and Hahn, H. *Journal of Applied Physics* **103**, 094308 (2008).

[13] Drings, H., Viswanath, R. N., Kramer, D., Lemier, C., Weissmüller, J., and Würschum, R. *Applied Physics Letters* **88**, 253103 (2006).

[14] Ghosh, S., Lemier, C., and Weissmuller, J. *IEEE Transactions on Magnetics* **42**, 3617 (2006).

[15] Schaefer, H. *Nanoscience*. Springer, Berlin/Heidelberg, (2010).

[16] Hahn, H. *Nanostructured Materials* **9**, 3 (1997).

[17] Acet, M., Mayer, C., Muth, O., Terheiden, A., and Dyker, G. *Journal of Crystal Growth* **285**, 365 (2005).

[18] Muth, O. *Nukleophile aromatische Substitution zur Synthese mehrzähniger Komplexliganden und Herstellung geordneter bimetallischer Nanopartikel*. Dissertation - Universität Duisburg-Essen, (2005).

[19] Vollath, D., Szabó, D. V., Taylor, R. D., and Willis, J. O. *Journal of Materials Research* **12**, 2175 (1997).

[20] Szabó, D. V. and Vollath, D. *Advanced Materials* **11**, 1313 (1999).

[21] Demtröder, W. *Experimentalphysik 2: Elektrizität und Optik*. Springer, Berlin/Heidelberg, (2008).

[22] Kittel, C. *Introduction to Solid State Physics*. Wiley, München, (1995).

[23] Viswanath, R. N., Kramer, D., and Weissmüller, J. *Electrochimica Acta* **53**, 2757 (2008).

[24] Jin, H. J., Parida, S., Kramer, D., and Weissmüller, J. *Surface Science* **602**, 3588 (2008).

[25] Erlebacher, J., Aziz, M. J., Karma, A., Dimitrov, N., and Sieradzki, K. *Nature* **410**, 450 (2001).

[26] Ding, Y., Kim, Y. J., and Erlebacher, J. *Advanced Materials* **16**, 1897 (2004).

[27] Gottstein, G. *Physikalische Grundlagen der Materialkunde*. Springer, Berlin, (2001).

[28] Petegem, S. V., Brandstetter, S., Maass, R., Hodge, A. M., El-Dasher, B. S., Biener, J., Schmitt, B., Borca, C., and Swygenhoven, H. V. *Nano Letters* **9**, 1158 (2009).

[29] Getzlaff, M. *Fundamentals of Magnetism*. Springer, Berlin/Heidelberg, (2008).

[30] Stöhr, J. and Siegmann, H. C. *Magnetism: From Fundamentals to Nanoscale Dynamics*. Springer, Heidelberg, (2006).

[31] Schwertmann, U. and Cornell, R. M. *Iron oxides in the laboratory: preparation and characterization.* Wiley-VCH, Weinheim, (2000).

[32] Topolovec, S. *Magnetische Eigenschaften nanokristalliner Metalloxide unter elektrochemischer Beladung.* Masterarbeit - TU Graz, (2010).

[33] Valenzuela, R. *Magnetic ceramics.* Cambridge University Press, Cambridge, (1994).

[34] Okrusch, M. and Matthes, S. *Mineralogie: Eine Einführung in die spezielle Mineralogie, Petrologie und Lagerstättenkunde.* Springer, Würzburg, (2010).

[35] Hamann, C. H. and Vielstich, W. *Elektrochemie.* Wiley-VCH, Weinheim, (1998).

[36] Schmickler, W. *Grundlagen der Elektrochemie.* Springer Science & Business, Braunschweig/Wiesbaden, (1996).

[37] Milazzo, G. and Defay, R. *Elektrochemie: Grundlagen und Anwendungen.* Birkhäuser, Basel, (1980).

[38] *SQUID MPMS-XL-7 - manual.* Quantum Design.

[39] Wahl, P. *Durchstimmbarer elektrischer Widerstand von nanoporösem Gold.* Masterarbeit - TU Graz, (2010).

[40] Wahl, P., Traußnig, T., Landgraf, S., Jin, H. J., Weissmüller, J., and Würschum, R. *Journal of Applied Physics* **108**, 073706 (2010).

[41] Ismail, K. M. and Badawy, W. A. *Journal of Applied Electrochemistry* **30**, 1303 (2000).

[42] Novoselsky, I. M. and Menglisheva, N. R. *Electrochimica Acta* **29**, 21 (1984).

[43] Lyons, M. E. and Brandon, M. P. *International Journal of Electrochemical Science* **3**, 1425 (2008).

[44] Richardson, J. T. and Vernon, L. W. *The Journal of Physical Chemistry* **62**, 1153 (1958).

[45] Lyons, M. E. and Brandon, M. P. *International Journal of the Electrochemical Science* **3**, 1425 (2008).

[46] Grigoriev, I. S., Meilikhov, E. Z., and Radzig, A. A. *Handbook of Physical Quantities.* CRC-Press, USA, (1997).

[47] Lotgering, F. *Philips Res. Rept.* **11**, 337 (1956).

[48] Salvarezza, R. C., Montemayor, M. C., Fatas, E., and Arvia, A. J. *Journal of Electroanalytical Chemistry* **313**, 291 (1991).

[49] Hulliger, F. *Journal of Physics and Chemistry of Solids* **26**, 639 (1965).

[50] Breiter, M. W. *Journal of Electroanalytical Chemistry* **81**, 275 (1977).

[51] Ghosh, S. *Charge Induced Tunable Magnetic Properties in Transition Metal Alloys.* Dissertation - Universität des Saarlandes, Schriftenreihe FZK, (2008).

[52] Lemier, C., Ghosh, S., Viswanath, R. N., Fei, G. T., and Weissmüller, J. *MRS Symp. Proceedings* , R2.6.1 (2005).

[53] Bozorth, R. M. *Ferromagnetism.* van Nostrand, USA, (1961).

[54] Traußnig, T., Topolovec, S., Nadeem, K., Szabó, D. V., Krenn, H., and Würschum, R. *Physica Status Solidi - Rapid Research Letters* **5**, 150 (2011).

[55] Fiorani, D., Testa, A. M., Lucari, F., D'Orazio, F., and Romero, H. *Physica B: Condensed Matter* **320**, 122 (2002).

[56] Batlle, X. and Labarta, A. *Journal of Physics D: Applied Physics* **35**, R15 (2002).

[57] Coey, J. M. D. *Physical Review Letters* **27**, 1140 (1971).

[58] Vollath, D. *Nanomaterials: an introduction to synthesis, properties and application.* Wiley-VCH, Germany, (2008).

[59] Nadeem, K., Krenn, H., Traussnig, T., Würschum, R., Szabó, D., and Letofsky-Papst, I. *Journal of Magnetism and Magnetic Materials - accepted* .

[60] Jacintho, G. V., Corio, P., and Rubim, J. C. *Journal of Electroanalytical Chemistry* **603**, 27 (2007).

[61] Posey-Dowty, J. *Icarus* **66**, 105 (1986).

[62] Zavaliche, F., Zhao, T., Zheng, H., Straub, F., Cruz, M. P., Yang, P. L., Hao, D., and Ramesh, R. *Nano Letters* **7**, 1586 (2007).

[63] Borisov, P., Hochstrat, A., Chen, X., Kleemann, W., and Binek, C. *Physical Review Letters* **94**, 117203 (2005).

[64] Duan, C., Jaswal, S. S., and Tsymbal, E. Y. *Physical Review Letters* **97**, 047201 (2006).

[65] Zavaliche, F., Zheng, H., Mohaddes-Ardabili, L., Yang, S. Y., Zhan, Q., Shafer, P., Reilly, E., Chopdekar, R., Jia, Y., Wright, P., Schlom, D. G., Suzuki, Y., and Ramesh, R. *Nano Letters* **5**, 1793 (2005).

[66] Rao, C. N. R., Thomas, P. J., and Kulkarni, G. U. *Nanocrystals: synthesis, properties and applications.* Springer, Berlin/Heidelberg, (2007).

[67] Park, J., Joo, J., Kwon, S. G., Jang, Y., and Hyeon, T. *Angewandte Chemie International Edition* **46**, 4630 (2007).

[68] Sun, S., Fullerton, E. E., Weller, D., and Murray, C. B. *IEEE Transactions on magnetics* **37**, 1239 (2001).

[69] Spieß, L. and Teichert, G. *Moderne Röntgenbeugung.* Vieweg & Teubner, Wiesbaden, (2005).

[70] Granqvist, C. G. *Journal of Applied Physics* **47**, 2200 (1976).

[71] Duan, C. G., Velev, J. P., Sabirianov, R. F., Zhu, Z., Chu, J., Jaswal, S. S., and Tsymbal, E. Y. *Physical Review Letters* **101**, 137201 (2008).

[72] Zhang, H., Richter, M., Koepernik, K., Opahle, I., Tasnádi, F., and Eschrig, H. *New Journal of Physics* **11**, 043007 (2009).

[73] Jette, B. and MacVicar, M. *Magnetics, IEEE Transactions on* **27**, 3025 (1991).

[74] Juzeliũnas, E. *Journal of Solid State Electrochemistry* **11**, 791 (2006).

[75] Ziman, J. M. *Principles of the theory of solids.* Cambridge University Press, Cambridge, (1979).

[76] Bass, J., Dugdale, J., Foiles, C., and Myers, A. *Numerical Data and Functional Relationships in Science and Technology, Landolt-Börnstein, News Group III, Vol. 15B.* Springer, Germany, (1985).

[77] Jin, H., Wang, X., Parida, S., Wang, K., Seo, M., and Weissmüller, J. *Nano Letters* **10**, 187 (2010).

[78] Tucceri, R. and Posadas, D. *Journal of Electroanalytical Chemistry* **283**, 159 (1990).

[79] Umeno, Y., Elsässer, C., Meyer, B., Gumbsch, P., and Weissmüller, J. *EPL (Europhysics Letters)* **84**, 13002 (2008).

[80] Dasgupta, S., Kruk, R., Ebke, D., Hütten, A., Bansal, C., and Hahn, H. *Journal of Applied Physics* **104**, 103707 (2008).

[81] Eilks, C. and Elliott, C. *Journal of Computational Physics* **227**, 9727 (2008).

[82] Ganon, J., Vanhuong, C., and Clavilier, J. *Surface Science* **79**, 245 (1979).

Deutsche Fassung:
Beschluss der Curricula-Kommission für Bachelor-, Master- und Diplomstudien vom 10.11.2008
Genehmigung des Senates am 1.12.2008

EIDESSTATTLICHE ERKLÄRUNG

Ich erkläre an Eides statt, dass ich die vorliegende Arbeit selbstständig verfasst, andere als die angegebenen Quellen/Hilfsmittel nicht benutzt, und die den benutzten Quellen wörtlich und inhaltlich entnommene Stellen als solche kenntlich gemacht habe.

Graz, am ……. ……..
(Unterschrift)

Englische Fassung:

STATUTORY DECLARATION

I declare that I have authored this thesis independently, that I have not used other than the declared sources / resources, and that I have explicitly marked all material which has been quoted either literally or by content from the used sources.

……. ……..
date (signature)